436

A STUDY OF THE REACTION $\pi^- p \rightarrow K^0 \Lambda$ AT 5 GeV/c USING A POLARIZED PROTON TARGET

Stephen Lindsay Lloyd

A thesis presented for the Degree of Doctor of Philosophy in the University of London

Imperial College
LONDON S.W.7

April 1978

ABSTRACT

The analysis of a high statistics study of the reaction $\pi^- p \rightarrow K^o \Lambda$ at 5 GeV/c using a polarized target is described. Data were taken in the range $0.0 < -t < 2.0$ $(GeV/c)^2$. The charged decay products from the K^o's were observed in optical spark chambers inside a large magnet viewed by television cameras.

The experimental asymmetry in the K^o production observed with target polarized up and down together with a measurement of the ratio of bound to unbound protons in the target material was used to calculate the polarization parameter P_o. The polarization was compared to the predictions of various phenomenological models.

Preface

The experiment described in this thesis was performed by a collaboration of physicists from CERN, ETH (Zurich), Imperial College, Southampton and Helsinki. The experiment started taking data in October 1974 and finished in December 1975. The author became a research student at Imperial College in October 1974 and worked with this group at CERN from April 1975, returning to Britain in January 1976 to analyse the data.

The author was not involved at all with the planning or setting up of the experiment but was involved with most of the data taking and all the analysis to date.

Chapters 1 and 2 of this thesis contain an introduction to the physics behind the experiment and a description of the apparatus involved. The author's contribution to the experiment starts with the data reduction described in Chapter 3 which was performed in conjunction with M.C.S. Williams. Chapters 4 to 6 present the analysis of the data and Chapter 7 deals with the design of a π^o detector carried out during autumn 1975. They are the author's own work.

CONTENTS

	Page
Abstract	1
Preface	2
List of Figures	5
List of Tables	7
Chapter 1 Introduction and Theoretical Background	
1.1 Introduction	9
1.2 Formalism	10
1.3 Hypercharge Exchange Reactions	16
1.4 Polarized Target Experiments	19
Chapter 2 The Experimental Setup and Data Taking	
2.1 Introduction	29
2.2 Apparatus	29
2.3 Data Taking	34
2.4 Trigger Conditions	35
Chapter 3 Data Reduction	
3.1 Introduction	44
3.2 ROMEO	44
3.3 Timing Considerations	47
3.4 Enrichment	52
3.5 Recognition of Lambdas	55
Chapter 4 Analysis	
4.1 Introduction	68
4.2 Kinematic Fitting	68
4.3 Contamination	73
4.4 Experimental Precision	76
4.5 Event Losses	80

Chapter 5 Experimental Results

5.1 Introduction 91

5.2 The Experimental Asymmetry 91

5.3 The Effective Target Polarization 99

5.4 Results 107

Chapter 6 Theoretical Discussion

6.1 Introduction 133

6.2 Comparison of the Data with Various Models 134

6.3 Predictions for A and R Parameters 143

6.4 Conclusions 145

Chapter 7 Test of a π^0 Detector

7.1 Introduction 152

7.2 The π^0 Detector 152

7.3 The Test Run 156

7.4 Conclusion 157

Appendix 1 Density Matrix Formalism 165

Appendix 2 Parity Violating Baryon Decays 167

Appendix 3 The Error in the Asymmetry 169

Acknowledgements 171

References 172

List of Figures

		Page
Figure 1.1	Mandelstam Variables	25
1.2	Duality Diagrams	25
1.3	Coordinate System	26
1.4	Hypercharge Exchange Data	27
1.5	Regge Trajectories	28
Figure 2.1	Schematic Layout of Beam Line	40
2.2	Schematic Diagram of Side View of CERN-ETH Magnet	41
2.3	Cross-section of Target and Veto Counters	42
2.4	Online Display of $K^{o}\Lambda$ Candidate	43
Figure 3.1	Structure of ROMEO Program	63
3.2	The Effects of the E Counter Cut	64
3.3	Logic Diagram for Enrichment Runs	65
3.4	K^{o} Mass Distribution	66
3.5	Lambda Mass Distribution	66
3.6	Missing Mass Squared to K^{o}	67
3.7	Missing Mass Squared to $K^{o}K^{o}$	67
Figure 4.1	Beam Parameters	83
4.2	$P(\chi^2)$ Distribution for Decay	84
4.3	$P(\chi^2)$ Distribution for Interaction	84
4.4	$P(\chi^2)$ for Double K^{o} Events	85
4.5	Stretch Functions	86
4.6	Centre of Mass Decay Angle for $-t > 0.5$ $(GeV/c)^2$	87
4.7	Centre of Mass Decay Angle for All t	87
4.8	Distribution of K^{o} Decay Point	88

	4.9	Distribution of Interaction Point	89
	4.10	(Missing Mass)^2 to K^o for Different Track Lengths	90
Figure	5.1	$P_o \lvert\tilde{P}_T\rvert$ as a Function of cos ϕ	121
	5.2	$P_o \lvert\tilde{P}_T\rvert$ as a Function of Decay Angle	122
	5.3	'Parity Violating' Asymmetry	123
	5.4	Sample Event Rates	124
	5.5	Values of R2	125
	5.6	Polarization as a Function of Missing Mass Squared	126
	5.7	Consistency Checks on R1	127
	5.8	The Structure of F_c	128
	5.9	The Acceptance of the Apparatus	129
	5.10	The Polarization Parameter	130
	5.11	Polarization for All t	131
	5.12	The Differential Cross-section	132
Figure	6.1	Predictions for the Polarization from Simple Regge Models	147
	6.2	Regge Cut Trajectories	147
	6.3	Regge-Pomeron Cuts	148
	6.4	Comparison of the Polarization with the Predictions of Various Models	149
	6.5	Helicity Amplitudes from the Model of Navelet and Stevens	150
	6.6	Predictions for A and R Parameters	151
Figure	7.1	Cross-section of π^o Detector	159
	7.2	Schematic View of Part of π^o Detector	160
	7.3	Sample Shower Distribution	161
	7.4	π^o Mass Distribution	162
	7.5	Energy Resolution	163
	7.6	Online Display of Shower Candidates	164

List of Tables

		Page
Table 1.1	t channel Exchanges for Charge and Hypercharge Exchange Reactions	24
Table 2.1	Data Taking Cycles	38
2.2	Target Details	39
2.3	Number of Triggers Recorded	39
Table 3.1	The Effects of the Beam Window	59
3.2	The Effects of the Chamber Cuts	59
3.3	The Effects of the Pulse Height Cuts	60
3.4	Timing in ROMEO	60
3.5	Breakdown of a Single Run by Event Types	61
3.6	Contents of Output Tape for A Single Run	61
3.7	Results of Eye Scan of $K^{o}\Lambda$ Candidates	62
3.8	Reasons for Failure of Visible $K^{o}\Lambda$ Events	62
Table 4.1	Beam Parameters	81
4.2	Momentum Precision for 114cm Tracks	81
4.3	t Precision	82
4.4	Event Losses During Data Reduction	82
Table 5.1	$P_o\lvert\tilde{P}_T\rvert$ for all Quadrants Assuming Uniform Acceptance	111
5.2	Acceptance Functions (A1/A2).2/π	111
5.3	Values of $P_o\lvert\tilde{P}_T\rvert$	112
5.4	$P_o\lvert\tilde{P}_T\rvert$ as a Function of Missing Mass Squared	113
5.5	Event Rates off Different Targets	114
5.6	Values of F_c, R1 and R	115
5.7	Values of R1 for Different $P(\chi^2)$ Interaction Cuts	116

5.8 Values of R as a Function of Missing Mass Squared 117

5.9 Values of the Polarization Parameter P_o 118

5.10 Corrections to the Differential Cross-section 119

5.11 Values of the Differential Cross-section 120

Table 7.1 Values of χ^2 as a Function of Gamma Energies 158

CHAPTER 1

Introduction and Theoretical Background

1.1 Introduction

A wealth of data on strong interactions has been accumulated since the discovery in 1947 of the pi-meson, the quantum of the strong nuclear force, postulated by Yukawa in 1935. There is however still no global theory which can account quantitatively for all this data.

Many of the so-called 'fundamental' particles can be classified by various symmetry schemes such as SU_3 and Regge recurrences. SU_3 relates particles by their charge, strangeness etc. while the classification of Regge recurrences relates particles with the same internal quantum numbers but different spins and masses. The Regge representation enables one to make predictions as to the behaviour of the scattering amplitudes in high energy collisions. Hence there is a complementarity between the static properties of particles and their scattering properties.

Two body elastic and inelastic reactions can be explained by various models such as Regge Poles, Absorption and Geometrical models. These models provide predictions for as yet unmeasured quantities in a wide variety of reactions. By doing experiments to measure these quantities one is able to test the various models and hence modify or

reject them in order to fit the data.

In the experiment described in this thesis, it was proposed to measure directly the scattering amplitudes in $\pi^- p \rightarrow K^o \Lambda$. By doing this one would then be able to distinguish the best model for this reaction. At the time of writing only the polarization parameter has been measured and by using the differential cross-section one can only determine the scattering amplitudes if one has some theoretical input. However this can suggest which models are obviously wrong and which are worth developing further.

In this chapter, two body scattering in terms of helicity amplitudes is discussed. The general scattering properties of hypercharge exchange reactions are presented and it is shown how one can measure helicity amplitudes in a polarized target experiment.

1.2 Formalism

1.2.1 Helicity Amplitudes

In a relativistic formalism, two body elastic and inelastic reactions are most easily parameterized in terms of helicity amplitudes, where helicity is the component of the particle's spin along its direction of motion. For a spinless meson scattering off a spin $\frac{1}{2}$ baryon ($0^- \frac{1}{2}^+ \rightarrow 0^- \frac{1}{2}^+$) there are four such amplitudes F_{++}, F_{+-}, F_{-+} and F_{--} where

+ and - refer to the helicity ($\pm\frac{1}{2}$) of the spin $\frac{1}{2}$ baryon, before and after the interaction.

Parity conservation demands that $F_{++}=F_{--}$ and $F_{+-}=F_{-+}$ so we are left with two amplitudes F_{++} and F_{+-} denoting helicity non flip and flip in the outgoing baryon. In general the F amplitudes are complex numbers, so that the interaction is parameterized in terms of four real numbers. Hence three independent variables need to be measured in order to determine the interaction up to an overall phase. The differential cross-section is defined by

$$\frac{d\sigma}{dt} = |F_{++}|^2 + |F_{+-}|^2$$

1.2.2 Mandelstam Variables and Crossing

In a reaction $1 + 2 \rightarrow 3 + 4$ as shown in fig. 1.1, let P_i and M_i be the four momentum and mass of the i^{th} particle. The reaction can be described in terms of three Mandelstam variables, s, t and u defined by

$$s = (P_1 + P_2)^2 = (P_3 + P_4)^2$$
$$t = (P_1 - P_3)^2 = (P_2 - P_4)^2$$
$$u = (P_1 - P_4)^2 = (P_2 - P_3)^2$$

with $s + t + u = \sum M_i^2$

Transforming particle to antiparticle is equivalent to reversing the sign of the four momentum as shown in fig. 1.1. By crossing symmetry all three channels $1 + 2 \rightarrow 3 + 4$, $1 + \bar{3} \rightarrow \bar{2} + 4$ and $1 + \bar{4} \rightarrow \bar{2} + 3$ can be described by the same

amplitude A(s,t,u). A(s,t,u) can be analytically continued from one kinematic region to another and hence physical behaviour in one channel can influence behaviour in another.

1.2.3 Regge Poles and Trajectories

Most of the differential cross-sections for $0^-\frac{1}{2}^+ \rightarrow 0^-\frac{1}{2}^+$ reactions have a sharp peak in the forward direction. This suggests that the scattering is peripheral and takes place through the exchange of a boson. Models based on the exchange of a meson with spin J are unable to account for the energy and angular dependences observed for reactions with $J \gg 1$.

If however the exchanged object is allowed to have angular momentum which is a function of the invariant 4 momentum transfer t, the energy dependence of the cross-section is a power law consistent with experiment. This is known as the Regge Pole model. Thus a good starting point for any theory of high energy scattering is a peripheral model based on Regge Pole exchange.

In order to conserve quantum numbers at the two vertices, charge exchange reactions proceed via the exchange of the (vector) and A_2(tensor) trajectories, whereas hypercharge exchange reactions proceed via the exchange of K^*(vector) and K^{**}(tensor) trajectories. The trajectory is the straight line that relates the mass squared and the spins of the particles. The various

exchanges are shown in Table 1.1 for some charge and hypercharge exchange reactions. Duality diagrams showing two of the reactions in terms of their quark contents are shown in fig. 1.2.

The line reversed hypercharge exchange reactions $\pi N \rightarrow KY$ and $\bar{K}N \rightarrow \pi Y$, where N is a nucleon and Y a hyperon (i.e. Λ or sigma), are particularly important in the study of Regge Poles and the corrections to the models. One of the reasons is that in the Λ- /sigma production reactions, the weak decay of the hyperon acts as a polarization analyser and so a complete set of observables can be obtained using a polarized target without having to do a double scatter to determine the recoil polarization.

1.2.4 Density Matrix Formalism

Hypercharge exchange reactions are best described within the framework of the density matrix formalism which is described in Appendix 1.

If we start with an initial density matrix

$$\rho^i = \tfrac{1}{2}(1 + \underline{P}^i \cdot \underline{\sigma})$$

where $\underline{P}^i$ is the polarization of the initial state baryon and $\underline{\sigma}$ are the Pauli matrices, then the final state density matrix ρf is given by $\rho f = M \rho^i M^+$ where M is some matrix. It can be shown (Ref. 1) that M must be of the form $M = F_{++} - iF_{+-}\, \hat{\underline{n}} \cdot \underline{\sigma}$ where $\hat{\underline{n}}$ is the normal to the scattering plane.

If $F_{++} = f$ and $F_{+-} = h$ then f can be expressed as;

$$\rho f = \tfrac{1}{2}(f - ih\hat{\underline{n}}.\underline{\sigma})(1 + \underline{P}^i.\underline{\sigma})(f^* + ih^*\hat{n}.\underline{\sigma})$$

which reduces to

$$\rho f = \tfrac{1}{2}\left[|f|^2 + |h|^2 + 2\mathrm{Im}f^*h\hat{\underline{n}}.\underline{\sigma} + 2\mathrm{Im}f^*h(\underline{P}^i.\hat{\underline{n}}) - 2\mathrm{Re}f^*h(\underline{P}^i_\wedge\hat{\underline{n}}).\underline{\sigma} + (|f|^2 + |h|^2)(\underline{P}^i.\hat{\underline{n}})(\hat{\underline{n}}.\underline{\sigma}) + (|f|^2 - |h|^2)(\hat{\underline{n}}_\wedge(\underline{P}^i_\wedge\hat{\underline{n}})).\underline{\sigma}\right]$$

If we define the Wolfenstein parameters (Ref. 2) P_o, A and R by;

$$P_o = \frac{2\mathrm{Im}f^*h}{|f|^2+|h|^2} \qquad A = \frac{-2\mathrm{Re}f^*h}{|f|^2+|h|^2} \qquad R = \frac{|f|^2-|h|^2}{|f|^2+|h|^2}$$

then $$\rho f = \frac{(|f|^2+|h|^2)}{2}\left\{1 + P_o\underline{P}^i\hat{\underline{n}} + \left[P_o\hat{\underline{n}} + (\underline{P}^i.\hat{\underline{n}}).\hat{\underline{n}} + A(\underline{P}^i_\wedge\hat{\underline{n}}) + R\hat{\underline{n}}\,(\underline{P}^i_\wedge\hat{\underline{n}})\right].\underline{\sigma}\right\}$$

If $|f|^2 + |h|^2 = \left(\frac{d\sigma}{d\Omega}\right)_o$ then

$$\rho f = \left(\frac{d\sigma}{d\Omega}\right)_o \frac{(1 + P_o\underline{P}^i.\hat{\underline{n}})}{2}\left(1 + \frac{1}{1+P_o\underline{P}^i.\hat{\underline{n}}}\left[P_o\hat{\underline{n}} + (\underline{P}^i.\hat{\underline{n}}).\hat{\underline{n}} + A(\underline{P}^i_\wedge\hat{\underline{n}}) + R\hat{\underline{n}}_\wedge(\underline{P}^i_\wedge\hat{\underline{n}})\right].\underline{\sigma}\right)$$

Comparing this with

$$\rho f = \tfrac{1}{2}\left(\frac{d\sigma}{d\Omega}\right)(1 + \underline{P}^f.\underline{\sigma}) \text{ we have}$$

$$\left(\frac{d\sigma}{d\Omega}\right) = \left(\frac{d\sigma}{d\Omega}\right)_o (1 + P_o\underline{P}^f.\hat{\underline{n}}) \qquad - \qquad (1.1)$$

where the final state baryon polarization is given by

$$\underline{P}^f = \frac{1}{1+P_o\underline{P}^i.\hat{\underline{n}}}\left\{P_o\hat{\underline{n}} + (\underline{P}^i.\hat{\underline{n}})\hat{\underline{n}} + A(\underline{P}^i_\wedge\hat{\underline{n}}) + R\hat{n}_\wedge(\underline{P}^i_\wedge\hat{n})\right\}$$

1.2.5 Angular Distributions

In Appendix 2 the decay distribution for a parity violating weak decay is derived.

$$\left(\frac{d\sigma}{d\Omega}\right)_{decay} = \left(\frac{d\sigma}{d\Omega}\right)' \quad (1 + \alpha \underline{P}^f . \hat{\underline{k}})$$

Using the coordinate system shown in fig. 1.3, we have that

$$\underline{P}^f . \hat{\underline{k}} = \frac{1}{1+P_o P_T \cos\phi} \left\{ P_o \sin\theta \sin\psi + P_T \cos\phi \sin\theta \sin\psi \right.$$
$$\left. + A P_T \sin\phi \cos\theta + R P_T \sin\phi \sin\theta \cos\psi \right\}$$

where P_T is the target baryon spin.

Hence the angular distribution for a reaction $0^- \tfrac{1}{2}^+ \rightarrow 0^- \tfrac{1}{2}^+$ where the recoil baryon decays weakly, can be expressed as

$$W(\cos\theta,\psi,\phi) \sim \left(\frac{d\sigma}{d\Omega}\right)_{prod} \cdot \left(\frac{d\sigma}{d\Omega}\right)_{decay}$$
$$\sim (1 + \alpha \hat{\underline{P}} . \hat{\underline{k}})(1 + P_o P_T \cos\phi)$$
$$\sim 1 + \alpha P_o \sin\theta \sin\psi + P_T \left\{ P_o \cos\phi + \alpha (\cos\phi \sin\theta \sin\psi \right.$$
$$\left. + A \sin\phi \cos\theta + R \sin\phi \sin\theta \cos\psi) \right\} \qquad - (1.2)$$

Thus for the reaction $\pi^- p \rightarrow K^o \Lambda$, by measuring the decay distribution for $\Lambda \rightarrow \pi^- p$, the parameters P_o, A and R can be extracted. Since $P_o^2 + A^2 + R^2 = 1$, one needs an additional measurement, that of $d\sigma/dt$ to enable the helicity flip and non flip amplitudes to be determined up to an overall sign.

1.3 Hypercharge Exchange Reactions

We have seen that by using a polarized target and by measuring the decay parameters of the recoil hyperon we can determine the amplitudes for $\pi^- p \rightarrow K^o \Lambda$ for example. However several hypercharge exchange reactions share the same exchange trajectories and there are several features common to all these reactions. Any model which explains the structure of the amplitudes in one reaction must also be able to describe or predict structure in other reactions.

Some of the main features of hypercharge exchange reactions are listed below. The differential cross-sections and polarizations for some of the reactions are shown in fig. 1.4 taken from Ref. 3.

1.3.1 Shrinkage

If the differential cross-section is parameterized as $\frac{d\sigma}{dt} \sim e^{-bt}$ and b increases with centre of mass energy $\sqrt{s}$, then this is known as shrinkage.

For $-t \gtrsim 0.02$ all hypercharge exchange reactions exhibit shrinkage consistent with exchange degenerate K^* - K^{**} pole behaviour except for $\bar{K}N \rightarrow \pi\Sigma$ which has a flatter effective trajectory α_{eff} where;

$$\ln \frac{d\sigma}{dt} = \text{const} + \left[2\alpha_{eff}(t) - 2\right] \ln s$$

For small $|t|$ the Σ reactions have trajectories noticeably higher than those for the Λ reactions. The

exchange degenerate K^{*} - K^{**} trajectory $\alpha = 0.35 + 0.82t$ is shown in fig. 1.5 along with the ρ - A_2 trajectory.

1.3.2 Crossing

The cross-sections for the line reversed pair of reactions $\pi N \rightarrow KY$ and $\bar{K}N \rightarrow \pi Y$ should be equal asymptotically i.e. at high $\sqrt{s}$, these reactions having different s-channels but the same t-channel. In the 4-8 GeV/c region the cross-sections for $\bar{K}N \rightarrow \pi Y$ are larger by up to a factor of two which in general decreases as the forward direction is reached. This effect is most pronounced in the Λ reactions. At around 4 GeV/c for example $d\sigma/dt(K^{-}p \rightarrow \pi^{0}\Lambda)/d\sigma/dt(\pi^{-}p \rightarrow K^{0}\Lambda) \sim 1.5$ and $d\sigma/dt(K^{-}p \rightarrow \pi^{-}\Sigma^{+})/d\sigma/dt(\pi^{+}p \rightarrow K^{+}\Sigma^{+}) \sim 1.3$ at $t = -0.5(GeV/c)^{2}$.

1.3.3 SU(3) Properties

The polarizations in $\pi p \rightarrow K\Lambda$ and $\pi p \rightarrow K\Sigma$ have similar structures but opposite signs as have the reactions $\bar{K}p \rightarrow \pi\Lambda$ and $\bar{K}p \rightarrow \pi\Sigma$. One explanation is that the K^{*} exchange amplitudes in the Λ and Σ reactions are related by SU(3) octet symmetry.

If we define an amplitude A_8 proportional to the well measured $NN\pi$ coupling and α proportional to the reasonably well measured $\Sigma\Sigma\pi$ coupling and related to the ratio between the antisymmetric (F) and symmetric (D) amplitudes we can express

$$A_8 = \frac{\sqrt{15}}{10} D + \frac{\sqrt{3}}{6} F \qquad \alpha = \frac{\sqrt{3}}{6} \frac{F}{A_8}$$

α is the same for vector and tensor exchanges but different for helicity flip and non flip (denoted by - and + subscripts).

SU(3) Isoscalar factors (Ref. 4) give for $N \rightarrow 8 \otimes 8$:

$$N \rightarrow \Sigma K \sim \frac{-3\sqrt{5}}{10} D + \tfrac{1}{2}F = \sqrt{3}(2\alpha - 1)\, A_8$$

$$N \rightarrow \Lambda K \sim \frac{-\sqrt{5}}{10} D - \tfrac{1}{2}F = -\frac{(2\alpha + 1)}{\sqrt{3}}\, A_8$$

Thus the ratio of the couplings

$$\frac{g_{NK\Sigma}}{g_{NK\Lambda}} = -\frac{3(2\alpha - 1)}{(2\alpha + 1)}$$

or in the specific case of the Σ^0

$$\frac{g_{pK^+\Sigma^0}}{g_{pK^+\Lambda}} = \frac{\sqrt{3}(2\alpha - 1)}{(2\alpha + 1)}$$

Hence: $$\frac{d\sigma/dt\ (\pi^- p \rightarrow K^0\Sigma^0)}{d\sigma/dt\ (\pi^- p \rightarrow K^0\Lambda)} = 3\left(\frac{2\alpha - 1}{2\alpha + 1}\right)^2$$

since $$P_0 \frac{d\sigma}{dt} = 2\mathrm{Im}F_{++}F_{+-} = 2|F_{++}|\,|F_{+-}|\sin\phi_{+-}$$

and assuming the same phase ϕ_{+-} for Σ and Λ reactions we have

$$P_0 \frac{d\sigma}{dt}(\pi^- p \rightarrow K^0\Lambda) \sim 2\sin\phi_{+-} A_8^{+} A_8^{-} \left(\frac{2\alpha_+ + 1}{\sqrt{3}}\right)\left(\frac{2\alpha_- + 1}{\sqrt{3}}\right)$$

$$P_0 \frac{d\sigma}{dt}(\pi^- p \rightarrow K^0\Sigma^0) \sim \frac{2\sin\phi_{+-}}{3} A_8^{+} A_8^{-} \sqrt{3}(2\alpha_+ - 1)\sqrt{3}(2\alpha_- + 1)$$

$$\frac{P_0 \frac{d\sigma}{dt}(\pi^- p \rightarrow K^0\Lambda)}{P_0 \frac{d\sigma}{dt}(\pi^- p \rightarrow K^0\Sigma^0)} = \frac{1}{3}\,\frac{(2\alpha_+ + 1)(2\alpha_- + 1)}{(2\alpha_+ - 1)(2\alpha_- - 1)}$$

Thus although each reaction is interesting on its own, more information can be gained if reactions are compared

with others which are related to them via SU(3) symmetry relations.

1.4 Polarized Target Experiments

We wish to measure the P_o, A and R parameters in the reaction $\pi^- p \rightarrow K^o \Lambda$ in order to measure the helicity amplitudes and hence test the predictions of various phenomenological models.

We can see from equation 1.2 that maximum information on the parameters A and R is obtained when $\sin\phi = \pm 1$, i.e. when the lambda is produced parallel or antiparallel to the target spin direction. One therefore needs an experimental setup which allows the decays of these lambdas to be analysed.

1.4.1 Polarized Targets

An alcohol polarized target needs a high magnetic field (>2T) to produce high polarization. This would normally require pole pieces, separated by a gap of about 10cm., above and below the target. Hence the lambdas produced parallel or antiparallel to the target polarization, containing maximum A and R information would be lost into the pole pieces.

One solution is to have a conventional alcohol target polarized along the beam direction. This however makes it difficult to mount detectors close to the target to analyse the lambda decay.

Our solution was to use a 'frozen spin' target, made of 1,2-propanediol ($C_3H_8O_2$). The target is first polarized in a uniform 2.5T magnetic field produced by pole pieces mounted vertically outside the main magnetic field. It is then frozen by cooling to $< 0.05^{\circ}K$ and moved into a holding field of 1T. sufficient to keep it polarized for several hours.

1.4.2 Detectors

To enable the decay products of the produced lambdas to be analysed, a large magnet spectrometer was used. This consisted of a magnet filled with optical spark chambers viewed by television cameras. The magnetic field, as well as allowing the spark chamber tracks to be momentum analysed, acted as the holding field for the polarized target.

In order to study the reaction $\bar{\pi} p \rightarrow K^{\circ}\Lambda$ it is necessary to avoid as much as possible triggering on other reactions, to reduce analysis and apparatus dead time. Since we required a neutral final state, the target was surrounded by veto counters, containing heavy metal gamma converters, which vetoed events containing final state charged particles or gammas.

We also required the decay of at least one of the neutral final state particles inside the spark chamber fiducial volume. This was achieved by having a 'picket fence' of scintillation counters downstream of the last spark chamber module.

Even with these trigger conditions one did not trigger exclusively on $\pi^- p \rightarrow K^o \Lambda$ events. The background from other reactions is discussed in the next section.

1.4.3 Background Reactions

The main background reactions for this experiment were as follows

(1) $\pi^- p \rightarrow K^o \Lambda$ produced on unpolarized bound protons

(2) $\pi^- p \rightarrow K^o \Sigma^o$, $\Sigma^o \rightarrow \gamma \Lambda$ and the γ is undetected

(3) $\pi^- p \rightarrow \Lambda K^o$ (backward peak)

(4) $\pi^- p \rightarrow K^o Y^{o*}$, $Y^{o*} \rightarrow \bar{K}^o n$

(5) $\pi^- p \rightarrow K^o \bar{K}^o n$

(6) Events containing charged tracks or gammas which have escaped detection in the veto counters.

The effects of (1) are discussed in 1.4.5 and (2) is discussed in Chapter 5. Reactions (3), (4) and (5) are easily identified in the reconstruction and kinematic fitting and can be analysed separately. Background from (6) can also be identified and rejected.

1.4.4 Beam Energy

At beam energies of < 3 GeV, scattering amplitudes are best described in terms of s-channel resonance production, whereas at higher energies t-channel exchanges provide the better framework for describing the amplitudes.

We are interested in the structure of these t-channel exchange amplitudes and at low energy these could be complicated by resonance production in the s-channel, hence to overcome these problems it was decided to perform the experiment at 5 GeV . At this energy there is other selected data available for comparison including a good measurement of $d\sigma/dt$ in our channel.

1.4.5 Measurement of Polarization using a Frozen Spin Target

In Chapter 5, the polarization parameter P_o in $\pi^- p \rightarrow K^o \Lambda$ is measured using information from the forward K^o only. Since only the free protons of hydrogen in the propanediol target are polarized, one needs to separate events off these polarized protons from background events off protons bound inside carbon or oxygen nuclei. If one uses the lambda information in addition to the K^o information one can separate kinematically since the bound protons will have fermi momentum which will cause a momentum imbalance at the interaction vertex. If only the K^o information is used one cannot do this unless one's experimental precision is extremely good.

In polarization measurements of this kind the effects of the background can be separately determined (Ref. 5).

From equation 1.1 it follows that the polarization P_o at fixed momentum transfer t can be expressed as

$$P_o = \frac{1}{P_T \cos\phi} \frac{n_+ - n_-}{n_+ + n_-}$$

where $P_T \overset{\cos\phi}{\wedge}$ is the product $|\underline{P}^i.\hat{\underline{n}}|$ and $n_\pm$ are the counting rates of events on positively (up) or negatively (down) polarized protons.

With a polarized frozen spin target we have $N_\pm = n_\pm + m_\pm$ where $N_\pm$ are the total rates and $m_\pm$ is the background rate which is independent of the target polarization i.e. $m_+ = m_-$

$$\therefore P_o = \frac{1}{P_T \cos\phi} \frac{N_+ - N_-}{N_+ + N_-} \cdot \frac{N_+ + N_-}{n_+ + n_-}$$

where $\frac{N_+ + N_-}{n_+ + n_-} = R$ is the ratio of events on all protons to events on free protons, thus

$$P_o = \frac{R}{P_T \cos\phi} \frac{N_+ - N_-}{N_+ + N_-}$$

Hence one does not need to know for each event whether or not it was produced off a bound or unbound proton. The ratio R does not depend on target polarization and can be measured with unpolarized targets.

Table 1.1

t channel exchanges for charge and hypercharge reactions

Reaction	t channel exchange
$\pi^- p \to \pi^o n$	ρ
$\pi^- p \to \eta^o n$	A_2
$K^- p \to \bar{K}^o n$	ρ, A_2
$K_L^o p \to K_S^o p$	ρ, ω
$\pi^+ p \to K^+ \Sigma^+$	K^*, K^{**}
$\pi^- p \to K^o \Sigma^o$	K^*, K^{**}
$K^- p \to \pi^- \Sigma^+$	K^*, K^{**}
$\pi^- p \to K^o \Lambda$	K^*, K^{**}
$K^- p \to \pi^o \Lambda$	K^*, K^{**}

Figure 1.1

Mandelstam Variables

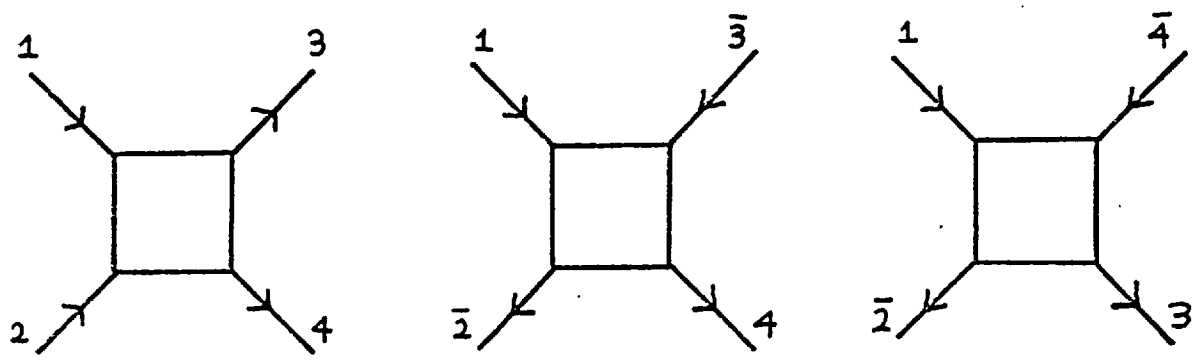


Figure 1.2

Duality Diagrams

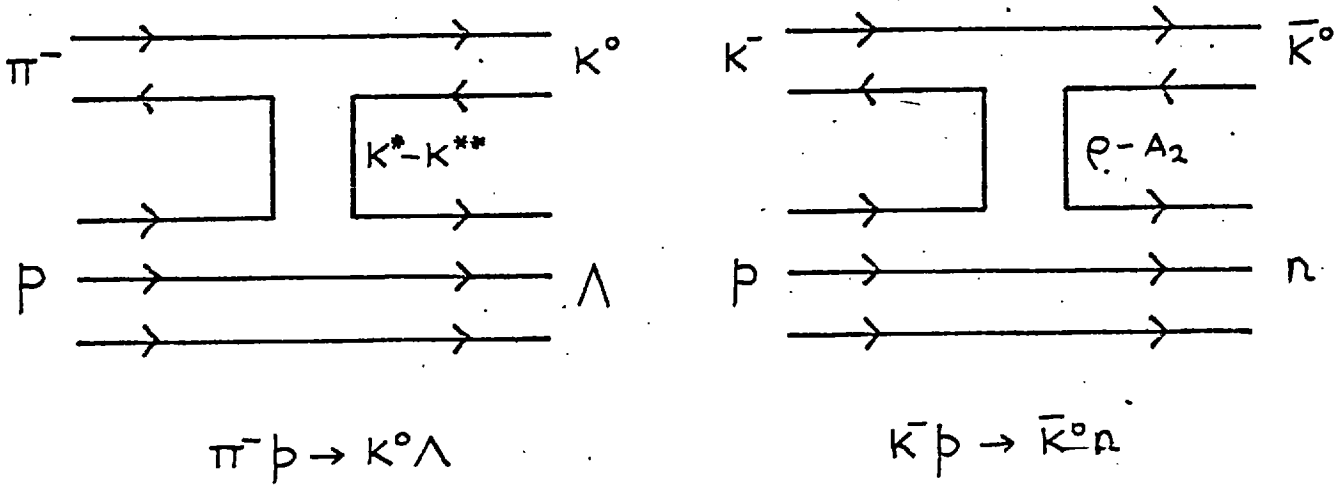


Figure 1.3

Coordinate System

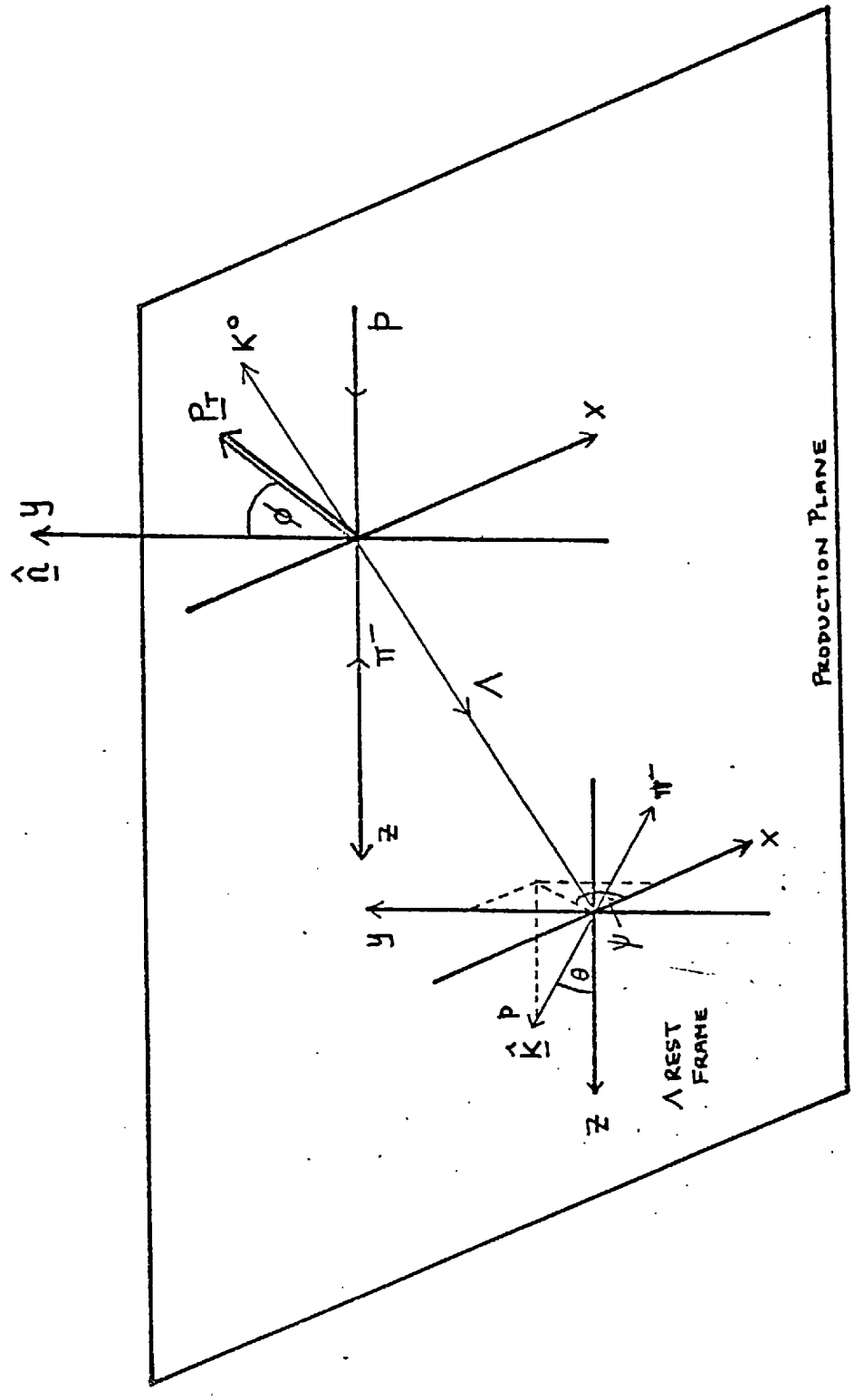
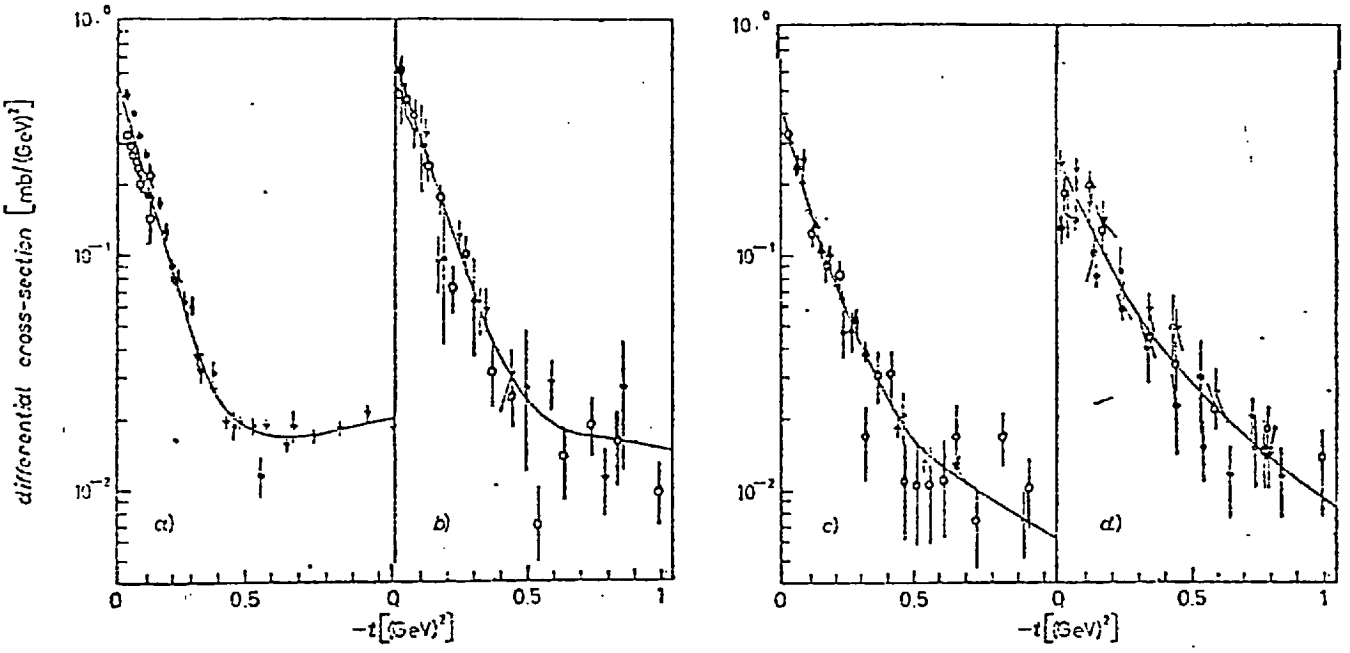
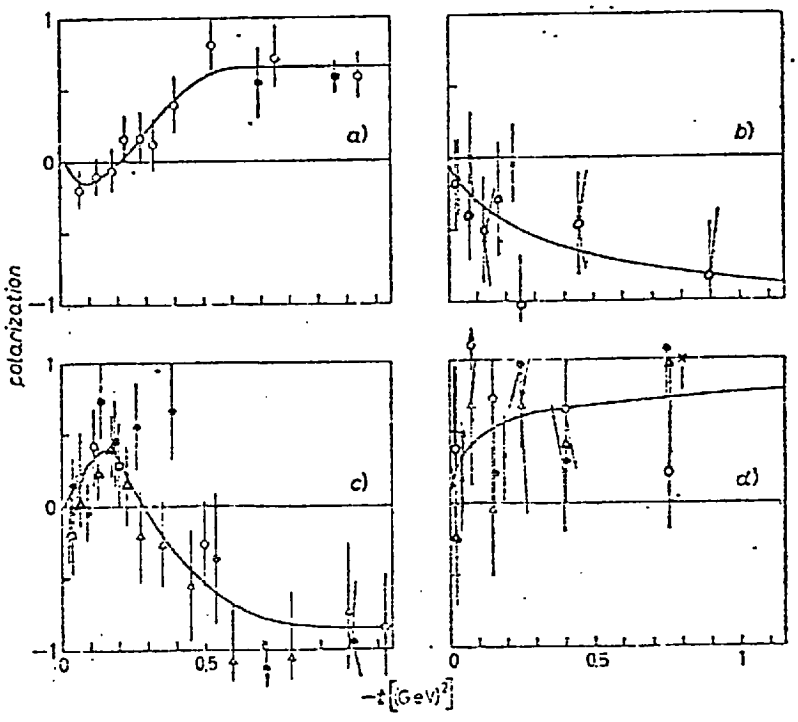


Figure 1.4

Hypercharge Exchange Data



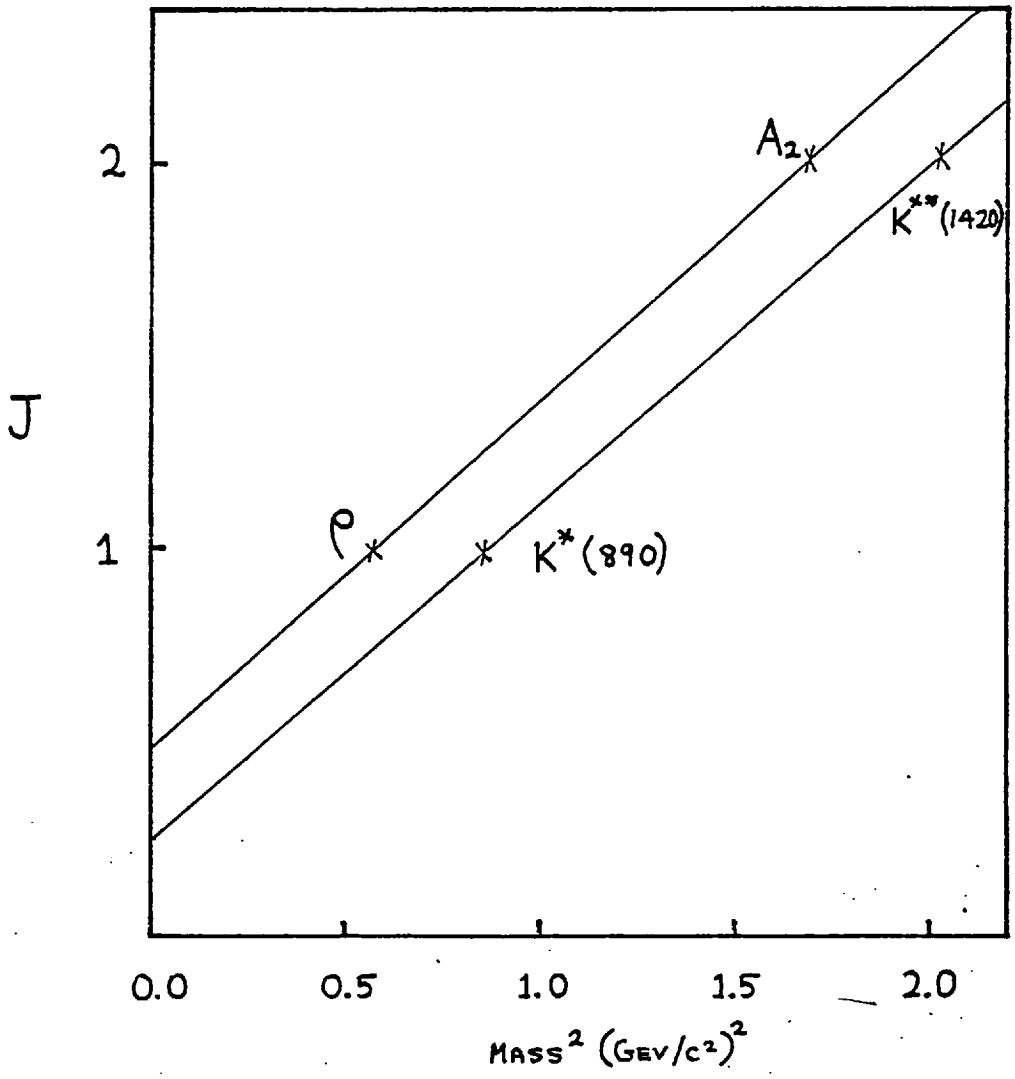
Hypercharge-exchange cross-section data in the region of 4 GeV/c, together with interpolating curves: *a)* $\pi^+p \to K^+\Sigma^+$: ▾ 4 GeV/c, ▾ 4 GeV/c; $\pi^-p \to K^0\Sigma^0$: • 4 GeV/c. *b)* $K^-p \to \pi^-\Sigma^+$: ○ 3.95 GeV/c, ▪ 4.07 GeV/c, ▾ 4.25 GeV/c. *c)* $\pi^-p \to K^0\Lambda$: ○ 3.9 GeV/c, ▫ 4 GeV/c, ▲ 4 GeV/c. *d)* $K^-p \to \pi^0\Lambda$: ▪ 3.9 GeV/c, ○ 3.95 GeV/c, ▾ 4.25 GeV/c; ½ $(K^-n \to \pi^-\Lambda)$: • 3.9 GeV/c.



Hypercharge-exchange polarization data in the region of 4 GeV/c, together with interpolating curves: *a)* $\pi^+p \to K^+\Sigma^+$: ○ 4 GeV/c, ▫ 4 GeV/c. *b)* $K^-p \to \pi^-\Sigma^+$: ○ 3.95 GeV/c, × 4.25 GeV/c. *c)* $\pi^-p \to K^0\Lambda$: ○ 3.95 GeV/c, • 4.5 GeV/c, ▲ 5 GeV/c. *d)* $K^-p \to \pi^0\Lambda$: ○ 3.95 GeV/c, × 4.25 GeV/c, ▲ 4.25 GeV/c; $K^-n \to \pi^-\Lambda$: • 3.9 GeV/c.

Figure 1.5

Regge Trajectories



CHAPTER 2

The Experimental Setup and Data Taking

2.1 Introduction

A 5 GeV/c negative pion beam was incident on a frozen spin polarized target. A neutral final state was demanded and the momenta of the decay products from this neutral final state were measured in the CERN-ETH magnet filled with optical spark chambers viewed by Plumbicon TV cameras.

2.2 Apparatus

2.2.1 The Beam

The beam line was designed to produce 5.10^5 negative pions per P.S. burst with momenta of 5 GeV/c. An upstream momentum slit ensured an accuracy of $\sim$ 1%. The beam line consisted of bending magnets, quadrupoles, a Čerenkov counter, beam defining scintillation counters, multiwire proportional chambers (MWPC's) and surface barrier diode counters, as shown in fig. 2.1.

The trajectory of the incoming beam particle was measured by three groups of MWPC's. MWPC1 and 2 were at each end of the Čerenkov counter C1 and consisted of 4 planes with 2mm. wire spacing. With the x direction along the beam line, the wires were aligned along the z, y, z=y

and z=-y directions. MWPC3 was mounted just upstream of the cryostat entrance window. It consisted of 4 planes with 1mm. wire spacing also with the wires aligned along the z, y, z=y, and z=-y directions.

An incoming beam particle was defined as S1.S2.S3.S4. S5.S6.$\bar{A}$1.C1, where S1 to S3 and S6 were scintillation counters, S4 and S5 were surface barrier diode counters inside the target cryostat. A1 was a large scintillation counter with a hole in it which was put into anticoincidence to veto beam halo. C1 was the Čerenkov counter filled with ethylene at 1 Kg/cm^2 to reject K^- and antiprotons in the beam. The discriminator of S2 was set to 50ns, the resolving time of the MWPC's, but was clipped to 5ns for beam coincidences to ensure that no other particle passed through S2, 50ns before the particle giving the trigger.

2.2.2 The Target

The polarized target was of the 'Frozen Spin' type and was constructed and operated by the CERN-Helsinki frozen spin target group (Ref. 6). The target was made of 1,2-Propanediol and was 150mm. long. Before April 1975 it had a diameter of 17mm. which was reduced to 16mm. after this date.

The target was first polarized in a 2.5 Tesla magnetic field produced by pole pieces mounted alongside the beam entrance. Polarization was achieved by irradiating the target with microwaves. Once the required degree of

polarization was achieved, the target was cooled to $< 50mK^{o}$ and moved into the main volume of the spectrometer magnet where the polarization was 'held' by the 1 Tesla magnetic field. The target was polarized in the $\pm z$ direction where z is vertically upwards and x is down the beam line.

The average polarization achieved was 85% with a loss rate of 1-5% per day. The polarization reversal time was 1-2 hours and the target had solid angle access of $4\pi \times 0.94$. The target was repolarized to the opposite parity, i.e. from spin up to spin down or vice versa, every 24 hours to avoid any systematic errors between +ve and -ve polarization data, for example running for a week on positive polarization and then finding that the number of $K^{o}\Lambda$ events was very low could bias the results.

2.2.3 The Spectrometer Magnet

The CERN-ETH magnet (Ref. 7) has a magnetic field of 1T over a volume of 200 x 90 x 80 $cm.^{3}$. There is a hole in the upper pole piece over which the camera hut was mounted. The magnet was open at both ends to allow the polarized target and the spark chambers to be readily accessed. A side view of the magnet is shown in fig. 2.2.

2.2.4 Veto Counters

In order to enhance the signal in the final state $K^{o}\Lambda$ it was necessary to veto events with charged tracks or π^{o}'s coming from the primary vertex and also events with $\Sigma^{o} \rightarrow \gamma\Lambda$.

Surrounding the target was a veto counter consisting of two cylindrical scintillation counters R1 and R2 each 5mm. thick. These were separated by 6mm. of tantalum which is approximately 1 radiation length. This acted as a gamma converter, the electrons being detected in R2. The average gamma conversion efficiency was $\sim$ 70%.

Obviously events where the lambda decayed before reaching the R counters would be vetoed, but since these lambdas would be slow in the laboratory frame, the loss is greatest at low $|t|$.

The downstream end of the target was covered by 3 'F' veto counters each 5mm. of scintillator with 5mm. tungsten between each pair. The F counters vetoed forward π^o's and charged tracks. The veto counter arrangement is shown in fig. 2.3.

2.2.5 'E' Counters

To ensure that we had a charged decay of one of the neutral particles, a hit was demanded in one or more of 8 downstream 'E' counters. These counters were in the form of a hodoscope at the downstream end of the spark chambers and were each 11.5cm. wide and 82cm. high.

2.2.6 The Spark Chambers

Nine modules of optical spark chambers were used in this experiment. The 3 downstream modules had 12 8mm. gaps

with 1.2mm. dead space between gaps. The 6 upstream modules each consisted of 14 1cm. gaps with no dead space. The most upstream 3 modules had a hole down the centre in which the polarized target and the veto counters were inserted (see fig. 2.2).

The chambers had an active area of 60 x 67 cm^2 each and were pulsed with 11Kv with a 450v/cm. D.C. clearing field.

2.2.7 The Camera System

The chambers were viewed by 7 plumbicon television cameras (Ref. 8). 6 of these were mounted above the chambers forming a stereo pair of 3 chambers each. The seventh camera was mounted downstream alongside the chambers and viewed, via a large mirror, modules 3, 4, 5 and 6. This camera was to improve the z accuracy of sparks located near the target where most lambda decays were expected, and hopefully to improve lambda finding.

2.2.8 Data Acquisition System

Two Hewlett Packard 2100-32K word computers from NP computer division at CERN were used during data taking. One of the computers read in the data from the CAMAC system in the form of scalar data, MWPC data and camera data. The data was stored in core and then written to tape. Sample data was sent to the second computer which performed checks on counter and chamber efficiencies etc., printed trigger rates and gave a visual display of selected events. An

example of such a display of a $K^{o}\Lambda$ candidate is shown in fig. 2.4.

2.2.9 Timing

The dead time of the data taking system, i.e. the time for the cameras to 'read' the data and for the computer to read out the buffers, was 22ms.

The 450 volts/cm. clearing field gave a spark chamber memory time of 600ns. There was a 400ns delay between the passage of the particle and the firing of the spark chambers.

2.3 Data Taking

Data were taken during 5 PS cycles of approximately 3 weeks each. These are summarized in Table 2.1. Cycle 4 was interrupted for about a month by a fire at the PS.

Each data taking run (given a separate number) comprised a separate file on output tape. A run normally consisted of a full data tape equivalent to about 1 hours data taking or 11,000 triggers, but could be shorter if for some reason data taking was stopped. Thus a tape could contain several runs.

The raw data tapes were transfered to the Rutherford Laboratory and compressed 3 into 1 onto 6250 b.p.i. tapes for analysis.

2.3.1 Targets

As well as taking data on the propanediol target, data were taken on Carbon, Hydrogen and 'Empty' targets. These data are discussed in Chapter 5.

The details of these targets and number of triggers recorded on each are shown in Tables 2.2 and 2.3. FEP (Fluorinated ethylene polypropane) refers to the bag in which the propanediol beads were contained. The propanediol polarized target was hydrogen free.

The later part of the 5^{th} cycle was used to test a π^o detector which is discussed in Chapter 7.

2.4 Trigger Conditions

2.4.1 Normal Triggers

The initial trigger conditions during the 1st. cycle were;

$$\prod_{i=1}^{6} S_i \cdot \bar{A}_1 \cdot C_1 \cdot \sum_{j=1}^{2} \bar{R}_j \cdot \sum_{k=1}^{3} \bar{F}_k \cdot \sum_{l=1}^{8} E_l$$

During the other cycles $\bar{A}_1$ was removed from the trigger to improve the trigger rate and C1 was not included in the trigger but was flagged. This enabled events with incident K^- or antiprotons to be recorded alongside π^- events. The amount of $K^-/\bar{p}$ in the beam was 3%.

2.4.2 Relaxed Trigger

From the 2nd cycle onwards, R2 was also removed from the trigger and flagged. This meant that events with a final state Σ^{o} could be taken in parallel with the final state Λ events.

2.4.3 Beam Trigger

From run 1209 onwards a beam trigger was introduced whereby every 100 events an event was recorded which only had one beam track on it. This was to enable the beam parameters to be monitored during analysis. Beam tracks are discussed in Chapter 4.

The trigger for beam tracks was;

$$\prod_{i=1}^{6} S_i \cdot \sum_{j=1}^{8} E_j$$

In addition to beam tracks being recorded every 100 events, two complete tapes of beam track events were recorded at different times during data taking.

2.4.4 Fiducial Events

At the start of every run and between PS bursts, fiducial events were recorded. These consisted of illuminated slits arranged in specific patterns between the spark chamber modules.

Because the number of slits on a bar was greater than the number of digitizings allowed per camera line, the bars were illuminated half at a time, one half being called a left fiducial event and the other a right fiducial event. Between PS bursts a left/right pair was recorded with the order alternating to produce the sequence:- (LR)(RL)(LR) etc., in order to cut down systematics. 20 such pairs of events were recorded at the beginning of each data taking run.

2.4.5 Slit Box and Slewing

Whilst the target was being repolarized, events were recorded, consisting of flash tubes illuminating wires stretched above the prisms covered with 'scotch-lite'. The intensity of the tube was varied so that the variation in apparent position of a spark with pulse height (slewing) could be investigated.

We also digitized a box with slits illuminated by fluorescent tubes inside it which could be inserted inside the magnet in place of the spark chambers. The slit box was normally used after each cycle for calibration purposes, evaluation of distortions etc.

2.4.6 Trigger Rates

The trigger rate for most of the experiment was ~ 50 triggers per 10^6 incoming pions which gave ~ 10 events per burst on average. Trigger rates are discussed in more detail in Chapter 4.

Table 2.1

Data Taking Cycles

Cycle	Started	Ended	Runs	Targets	Comments
1	31 Oct 74	21 Nov 74	500-879	Propanediol, Empty	Normal trigger
2	7 Apr 75	3 May 75	1015-1444	Propanediol, Carbon	$\bar{A}1$ out, $\check{C}$ and R2 flagged
3	6 Jun 75	25 Jun 75	1445-1821	Propanediol, Carbon	"
4 (a)	28 Aug 75	29 Aug 75	2015-2049	Propanediol	"
(b)	26 Sep 75	16 Oct 75	2070-2575	Propanediol	"
5	6 Dec 75	18 Dec 75	3001-3131	Hydrogen, π^0 test	"

Table 2.2

Target Details

Material	Mass	Mass FEP	Length	Diameter
Propanediol (Cycle 1)	21.5g	4.99g	147mm	17mm
Propanediol (Cycles 2-4)	21.56g	4.99g	147mm	16mm
Carbon (Cycle 2)	18.31g	4.99g	5x10mm	15mm
Carbon (Cycle 3)	17.63g	5.28g	5x10mm	15mm
Hydrogen	-	-	150mm	-

Table 2.3

Number of triggers recorded

Target	Number of data tapes	Number of triggers
Empty	9	100,000
Unpolarized	5	60,000
Polarized +ve	502	5,500,000
Polarized -ve	492	5,400,000
Carbon	77	850,000
Hydrogen	58	650,000

Figure 2.1

Schematic Layout of Beam Line

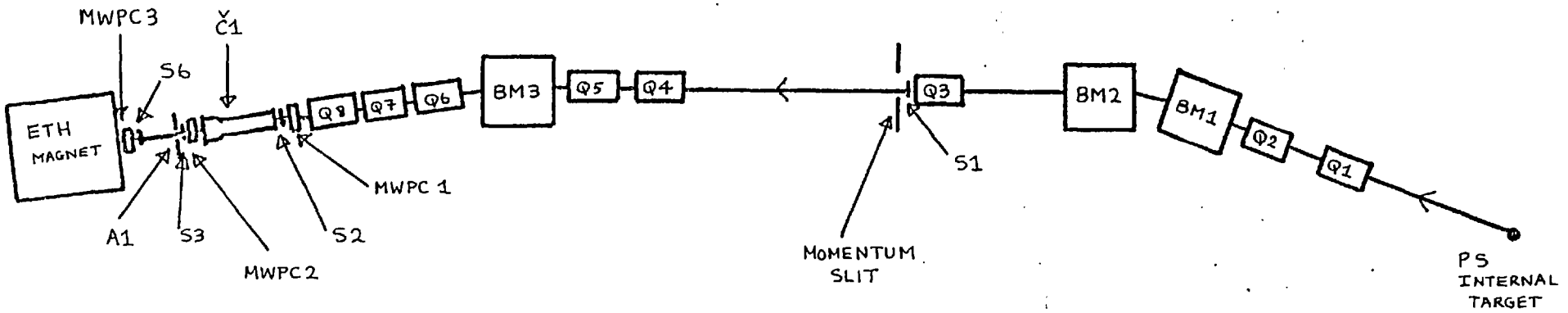


Figure 2.2

Schematic Diagram of Side View of
CERN - ETH Magnet

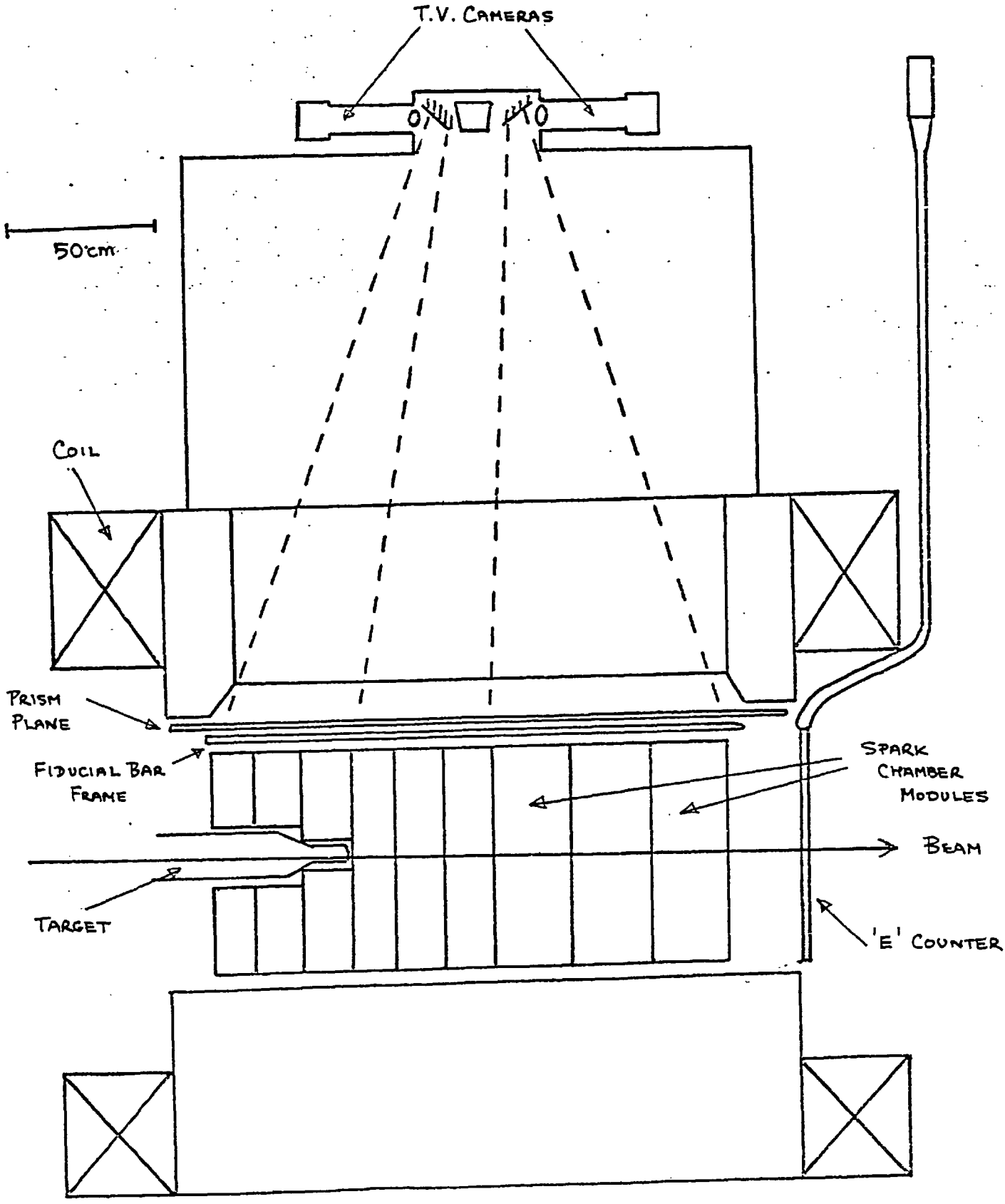


Figure 2.3

Cross-section of Target and Veto Counters

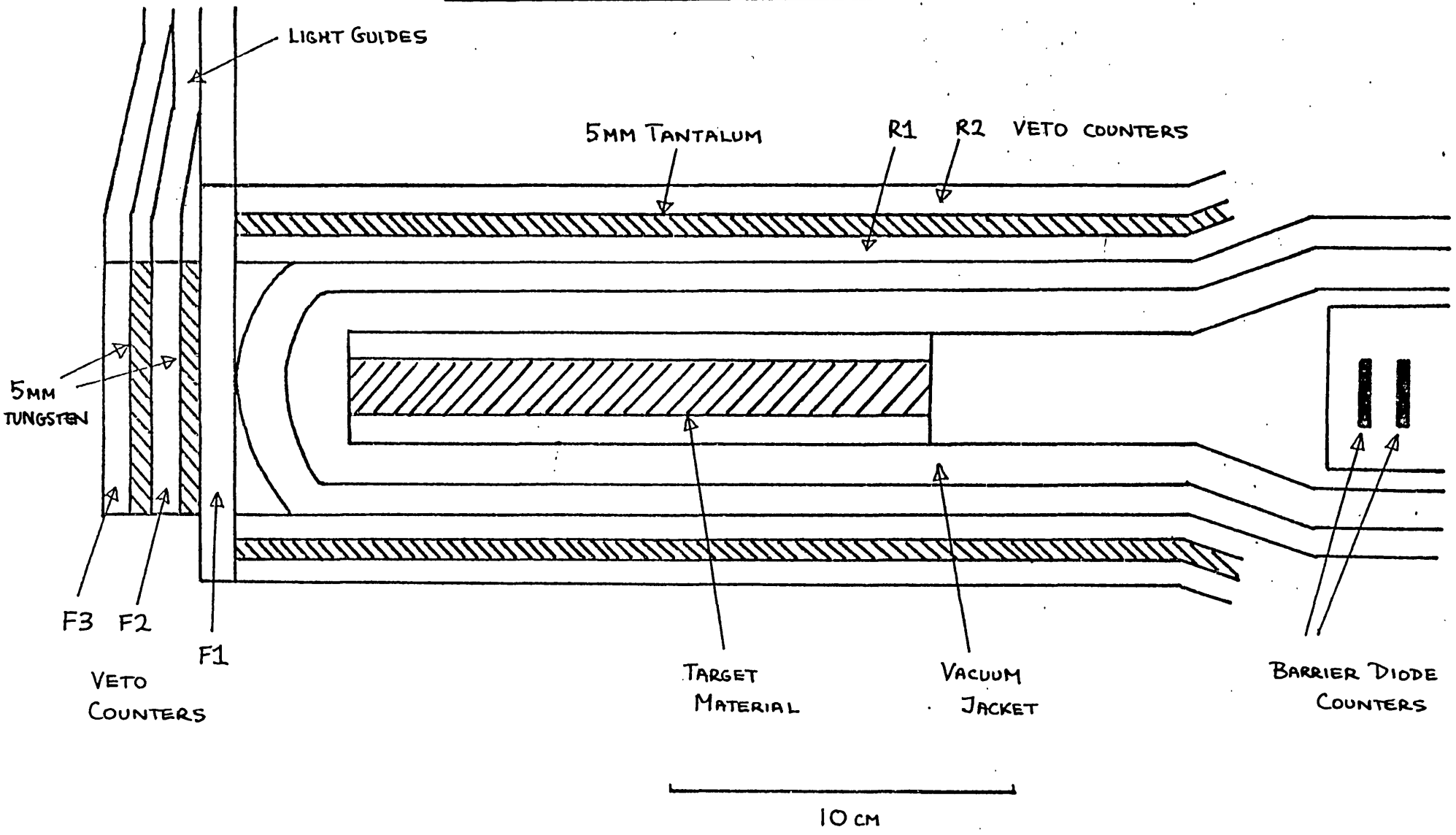
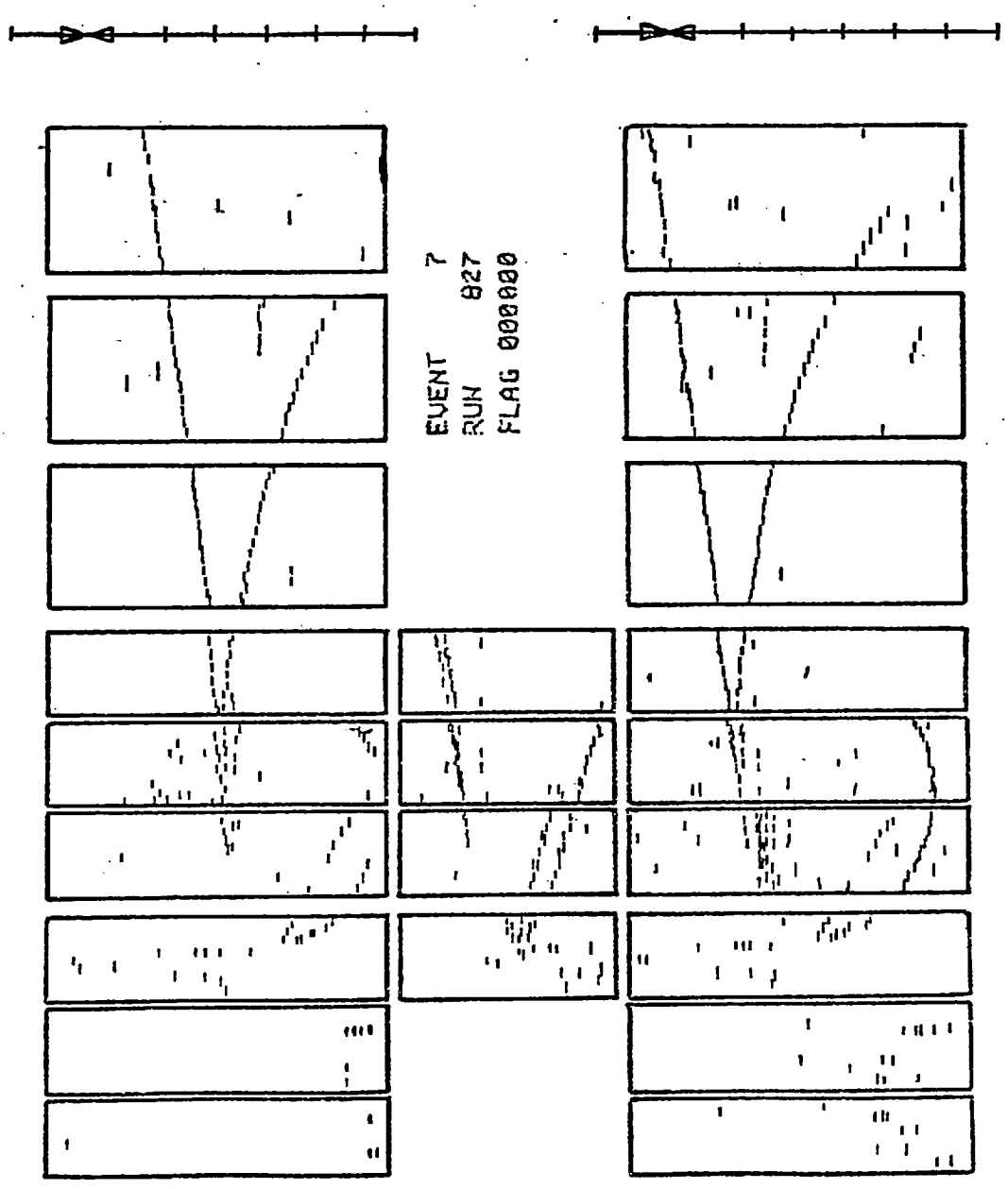


Figure 2.4

Online Display of $K^{o}\Lambda$ Candidate



CHAPTER 3

Data Reduction

3.1 Introduction

Due to the very large amount of data, $\sim 10^7$ triggers occupying 400 6250 b.p.i. magnetic tapes, and the difficulty of recognising slow recoil lambdas which decay near the target and at large angles to the beam direction, it was decided to enrich the data.

In principle this enrichment consisted of doing a relatively quick and simple analysis of all the data to pick out potential $\pi^- p \rightarrow K^o \Lambda$ candidates which would be more fully analysed later using a more sophisticated program.

In this chapter, the analysis program ROMEO is briefly described together with the details of the data enrichment.

3.2 ROMEO

ROMEO (Ref. 9) is a program written at CERN for recognition and geometrical reconstruction of spark chamber events taken by the OMEGA magnetic spectrometer system. Since our experimental system was very similar to that of OMEGA we were able to use their program extensively modified to suit the geometry of our experiment.

The program consists of several modules corresponding to different phases of the analysis. A schematic diagram of the program structure is shown in fig. 3.1. During debugging the various modules were overlayed to save space but in the final version only GEOMETRY was overlayed. The different modules are described below. All constants for the program are preset in Blockdata in the ROOT module which also deals with input and output, event selection and overall control of the program.

3.2.1 The Initialization Module

The initialization module is called once at the start of the program and reads in control cards which can be used to change the standard values of certain constants. It allows the user to control event selection and the amount of output one gets each event. Some secondary constants are calculated in the units required by the program.

3.2.2 The Fiducial Mark Module

The fiducial mark module is called at the beginning of every run on tape and computes the transformation coefficients which convert the raw plumbicon digitizings into the system of coordinates used in ROMEO. If the required number of fiducial events are not found at the start of the first run then the program skips to the start of the next run and so on until they are found. Once the coefficients have been calculated the tape is rewound to the first run again.

For the purposes of the enrichment the coefficients were found to be sufficiently stable throughout a run to make it unnecessary to update the coefficients from the fiducial events between bursts.

3.2.3 The Pattern Recognition Module

The pattern recognition module sorts out tracks from the raw digitizings for each event and sends the ordered coordinates to the geometry module.

The spark chamber system is scanned gap by gap from the downstream end. Once a digitizing is found, a temporary track bank is set up. An area within certain tolerances is then searched in the next gaps and if digitizings are found in at least 2 of the next 4 gaps the track bank is made permanent; otherwise it is abandoned. Further digitizings are added as each gap is scanned. The bank is closed if no digitizing is found for 14 gaps.

To overcome the necessity to correct for the staggering of sparks in the crossed electric and magnetic fields, tracks are only followed in odd numbered gaps. Digitizings in even numbered gaps are later complemented to the tracks.

Finally tracks in different views are matched together to find which are the projections of a track in space. As long as there is at least one track of each sign found in

at least two views, the information is passed to Geometry - otherwise the event is abandoned.

3.2.4 The Geometry Module

The geometry module takes the tracks in the different views and reconstructs the track in space. The track parameters - momentum, dip and azimuthal angles - are calculated. Pairs of positive and negative tracks with a common $\overset{h}{\underset{\Lambda}{c}}$ord that points towards the target are traced back through the magnetic field and a vertex fit is attempted (Refs. 10 and 11). If a vertex is successfully fitted, a one constraint kinematic fit is attempted in order to decide whether or not the event is a likely $\pi^- p \rightarrow K^o \Lambda$ candidate. This kinematic fit is described in Chapter 4.

3.2.5 The Close Module

The close module writes a short summary after each file has been processed as an aid to bookkeeping as well as resetting some constants ready for the next run to be processed.

3.3 Timing Considerations

After it had been modified to suit our setup, ROMEO took ~ 200ms to process an event on the IBM 360/195 at the Rutherford Laboratory. This would have required in the region of 700 hours of CPU time to process all of the data which would have made progress impossibly slow. A

reasonable amount of time was thus spent in trying to reduce the time per event without reducing our final data sample too much. The various methods tried are described below.

3.3.1 Beam Window

About 20% of events have a stray beam track associated with the event which is no use in the analysis but wastes the computer's time being parameterized. The idea of a beam window, or road as it sometimes called, is that the average position of the beam in each gap is determined and any sparks occuring within a certain distance of that position are eliminated before pattern recognition.

The positions of sparks in a gap for a given view is given by a digitizing which corresponds to the distance of the spark from the edge of the chamber. One digitizing is equivalent to about 0.1mm. The first 100 events per run were analysed and the digitizings for each gap histogrammed. The bin with the most digitizings was taken as the central position of the beam in that gap, assuming that it agreed with a rough estimate made from an eye scan of events. This eliminates false values caused by breakdown in the chambers or dead spots on the camera for example. The beam window for that gap is defined as this value $\pm$ 50 digits - corresponding to a 1cm. road through the chambers. Once this had been done, the tape was rewound and normal analysis proceeded.

By looking at pictures of events with and without the beam window it appeared that beam tracks were removed quite well. However we can see from Table 3.1 that although the number of beam tracks was reduced from 19% to 4% with the time per event falling from 263ms to 237ms, the number of K^o's found fell from 29% to 26% leaving the time per K^o unchanged.

The beam window was operational from gap 43 onwards, gap 43 being the first after the target. Gap 3 was the most upstream, 124 the most downstream.

In order to regain some of the lost K^o's the window was not started till gap 85 with the hope that beam tracks would still be eliminated but K^o's would not. What actually happened was that some beam tracks were eliminated but others were left as short tracks between gaps 43 and 85 which no longer qualified as 'beam tracks' but were considered for V^o candidates which did not reduce the time/K^o.

Beam tracks are defined in Geometry as tracks which satisfy <u>all</u> the criteria

$$1/P = -0.2 \pm 0.015 \ (GeV/c)^{-1}$$

$$DIP = 0.0 \pm 10.0 \ mrad$$

$$AZI = 10.0 \pm 10.0 \ mrad$$

Once a track has been designated as a beam track it is not considered for the formation of vertices.

3.3.2 Chamber Cut

For the enrichment of the data we were looking for fast forward K^{o}'s and it was thought that time could be saved without significant loss of events by ignoring all gaps upstream of gap 43 i.e. upstream of the target exit. The information contained in the side view was not used for this analysis.

From Table 3.2 it can be seen that the best combination is no beam window with the upstream gaps ignored, resulting in a reduction of time but no loss of potential $K^{o}\Lambda$ events. A beam window was therefore not used.

3.3.3 Pulse Height Cut

Each digitizing as well as giving the postion in a gap of each spark also contains coded information on its pulse height. Sparks caused by ionization left by old tracks not associated with the trigger should be less bright and hence have lower pulse heights than tracks associated with the trigger. By setting a pulse height threshold it should therefore be possible to eliminate background and cut down analysis time.

From Table 3.3 it can be seen that raising the pulse height threshold does reduce the time but also decreases the number of potential $K^{o}\Lambda$ events more rapidly. Setting a threshold of 1 could show some improvement but it was

felt that it was better not to delete any sparks on the basis of pulse height.

3.3.4 E Counter Test

Since tracks associated with the trigger hitting a downstream E counter should give a count in that counter it was hoped that one could distinguish between tracks from the event and 'old' tracks by extrapolation of the track to the E counter and seeing whether or not the relevant counter fired.

For tracks that were reconstructed to form vertices, 76% were correlated with a hit in the appropriate E counter. Tracks that could not be formed into vertices were only correlated 43% of the time.

Three categories of track were defined

(a) Tracks which should have fired an E counter but didn't.
(b) Tracks which would have missed the E counters.
(c) Tracks correlated with a hit in the appropriate E counter.

The K^o effective mass distributions were examined for the case where both tracks of the V^o came from categories (b) or (c). This removed 25% of the K^o peak and 31% of the background.

The cut was then tightened so that one track had to be from category (c) and the other from (b) or (c). This removed 18% of the K^o peak and 69% of the background as

shown in fig. 3.2. The saving of time by geometry only having to consider these categories was only 3.7% and was not considered worth losing 18% of the data for.

A breakdown of the timing for various parts of the program is shown in Table 3.4. The time per event was eventually reduced to about 180ms by removing some redundancy in ROMEO and making some routines more efficient.

3.4 Enrichment

A diagram of the logic for the enrichment is shown in fig. 3.3. The analysis was done without slewing corrections and without the information from the side view. The pattern recognition part of ROMEO was set up so as to look only for fast forward tracks from forward K^o decay and not to attempt to analyse the recoil lambdas.

For every input file, corresponding to a data taking run, an output file was written. The contents of the records on the output file depended on what type of event was input to ROMEO. The different types of event are listed below. Each event consisted of a scaler record containing the electronic counter data, a MWPC record and a camera data record.

3.4.1 Fiducial Events

All the fiducial events at the beginning of each run were copied directly onto the output tape. Pairs of

fiducial events were also copied every 19 bursts, hence preserving the LRL... pattern and providing the option of updating the transformation coefficients during the run if required in the final version of ROMEO.

3.4.2 Beam Events

All beam trigger events were copied directly to the output tape so that the parameters of the beam can be monitored during future analysis.

3.4.3 K^- or Antiproton Triggers

When the Čerenkov was not included in the trigger but merely flagged, about 10% of the data consisted of a K^- or $\bar{p}$ beam particle. The $K^-/\bar{p}$ contamination in the beam was $\sim$ 3% but the trigger cross-section into neutral final states is higher for K^- or $\bar{p}$ interactions leading to a 10% trigger rate.

If in the analysis of these events, K^o's or lambdas were found then the event was copied onto tape but without the camera data i.e. only the scaler, MWPC and the geometry output banks from ROMEO were written on the tape. The majority of these events will probably be $K^-p \rightarrow K^on$ and no extra information could be gained from a reanalysis since the neutron will escape detection in our chambers. The amount of $\bar{p}p \rightarrow \Lambda\bar{\Lambda}$ is small.

3.4.4 Sigma Events

Whilst R2 was only flagged and not included in the trigger, the final state $K^{o}\Sigma^{o}$ was taken in parallel with $K^{o}\Lambda$, the gamma from $\Sigma^{o} \rightarrow \gamma\Lambda$ being responsible for the R2 hit. At the moment no attempt is being made to analyse this channel, so events having R2 hits were skipped.

3.4.5 Normal Triggers

Events with no R2 flag and no $\bar{\bar{C}}1$ flag were passed through the pattern recognition and geometry stages of ROMEO and dealt with in 3 ways.

(a) Events with no K^{o} or Λ found were skipped.

(b) Events with 1 K^{o} or 1 Λ identified by the kinematic fit were subjected to a cut on their missing mass squared to see whether they were possible $K^{o}\Lambda$ or ΛK^{o} events.

The cuts were :-

$$0.4 < MMK^{o\,2} < 1.9 \ (GeV/c^{2})^{2} \quad \text{or}$$
$$-0.5 < MM\Lambda^{2} < 1.0 \ (GeV/c^{2})^{2}$$

The unfitted K^{o} and Λ effective masses are shown in figs. 3.4 and 3.5 and the missing mass squared to the fitted K^{o} together with the cuts are shown in fig. 3.6. If an event satisfied these criteria it was copied completely to output tape with scalers, MWPC, camera and Geometry data and is known as a 'full' event. Events not satisfying the criteria were output with scalers, MWPC and Geometry data only and are known as 'half' events.

(c) Events with more than one K^{o} or Λ or one of each were output as full events.

3.4.6 Summary

The statistics of a typical run equivalent to about 1 hours data taking were as follows :-

12,269 triggers
6,403 (52%) had R2 flagged and were skipped

Of the remaining 5855, 1477 failed,
1428 in pattern recognition
44 with incorrect raw data
and 5 in geometry.

Failures in pattern recognition are usually due to there not being one track of each sign recognised. Incorrect raw data is usually attributed to some error in decoding the data from the cameras or a tape error. Failures in geometry sometimes occur when pattern recognition finds more tracks than geometry can handle.

The content of the remaining 4389 events is shown in Table 3.5. What was written on the output tape is shown in Table 3.6.

3.5 Recognition of Lambdas

In order to measure P_o, A and R it is necessary to measure both the forward K^o and the recoil lambda. The enriched data tapes contain events with a measured K^o with the missing mass in the lambda region. The second stage of the data reduction involves the reanalysis of these events to measure the recoil lambdas. This reanalysis has not yet been completed due to the difficulty of finding the recoil lambdas as explained below.

3.5.1 Improvements to ROMEO

(a) Tolerances

The tolerances controlling the track finding obviously needed to be relaxed since the program was set up to find fast forward tracks whereas the tracks from lambdas tend to be slow and wide angles.

Since the angles of the tracks tend to increase as one gets nearer the target region, the tolerances were adjusted accordingly so that downstream the tolerances were still fairly tight whereas close to the target region they were much more relaxed. Although this allows larger angle tracks to be found, it increases the amount of ambiguity if several tracks are close together.

(b) Side View

The data from the side view was incorporated and although track recognition seems to work fairly well, the problem of matching the tracks found in views 1 and 2 to those in view 3 (the side view) has still not been solved satisfactorily.

(c) Upstream Gaps

Data from all the gaps including those gaps upstream of the target are used. Lambdas where one of the tracks goes backwards are dealt with correctly, and the sign of the track is correctly computed, but the program gets confused if a track turns back on itself and is often treated as more than one track.

(d) Short Tracks

Some of the tracks from the lambda decay are extremely short, consisting of less than 6 sparks in one view. Most of these tracks are not found by ROMEO because of the need to find sparks in odd parity gaps and then complement them. Most of these tracks are present in module 3 and some other method of identifying them is needed.

3.5.2 Scanning

In order to see how well the program was doing and what type of events were giving problems, several events were drawn out as pictures and scanned by eye.

The results of scanning 96 $K^{o}\Lambda$ candidates (as defined by missing mass) are shown in Table 3.7. In addition the $K^{o}K^{o}$ events yield 2 $K^{o}\Lambda$ events found (both K^{o} and Λ identified), 2 probable $K^{o}\Lambda$ events and 12 possible $K^{o}\Lambda$ events. This is probably the source of the first peak in fig. 3.7, the missing mass squared to $K^{o}K^{o}$, the lambda being misidentified so that the missing mass squared is shifted from zero.

One can calculate how many lambdas one expects to see in the chambers from the branching ratios

$$\Lambda \rightarrow n\pi^{o} \quad (35.8\%)$$

$$\text{and } \Lambda \rightarrow p\pi^{-} \quad (64.2\%)$$

Using the acceptance calculated in Chapter 5 of 25.6% for neutral and 10.8% for charged decay, one expects 55 neutral and 41 charged lambda decays.

In the original proposal (Ref. 12) we define a measureability criterion for lambdas of 8 sparks in one track and 20 in the other. 60% of lambdas were expected to meet this requirement. Putting in this requirement one therefore expects

55 K^o events with no lambda seen
25 K^o events with a measureable lambda
16 K^o events with an unmeasureable lambda

From Table 3.7 one can see that the numbers of events with no lambda seen are in reasonable agreement, but that the number of measureable lambdas is lower than expected. This means that to reach the total numbers of events for the full analysis (60,000 events off free protons) quoted in the proposal, we need to rescue a large number of 'lambda possible' category assuming we can recognise all the events with a lambda seen. The reason for failure of 5 events where the lambda should have been picked up are shown in Table 3.8.

3.5.3 Conclusions

A lot of work is required on program developement to enable us to recognise lambdas in confused events and where the tracks have few sparks before a full P_o, A and R analysis can be done.

Table 3.1

The effects of the beam window

	No window	Window gap 43	Window gap 85
V^o's	52.5%	48.8%	55.2%
K^o's	29.2%	26.0%	24.8%
Λ's	4.6%	4.4%	6.0%
Tracks	201%	168%	192%
Beam Tracks	18.9%	3.6%	7.6%
Patrec time	167ms	139ms	159ms
Geom time	66ms	60ms	68ms
Time/event	263ms	237ms	267ms
Time/K^o	0.90s	0.91s	1.07s

Table 3.2

The effects of the chamber cuts

	No window	No window + 43 clear gaps	Window gap 43 + 43 clear gaps
V^o's	52.5%	54.7%	50.2%
K^o's	29.2%	30.8%	27.6%
Λ's	4.6%	4.8%	4.6%
$K^o\Lambda$'s	7.8%	7.9%	6.3%
Tracks	201%	195%	161%
Beam Tracks	18.9%	19.6%	7.1%
Patrec time	167ms	148ms	120ms
Geom time	66ms	62ms	54ms
Time/event	263ms	241ms	202ms
Time/$K^o\Lambda$	3.37s	3.03s	3.18s

Table 3.3

The effects of the pulse height cuts

	Pulse Height Threshold			
	0	1	2	3
Patrec	158ms	154ms	151ms	143ms
Geom	67ms	66ms	69ms	60ms
Time/event	242ms	238ms	237ms	221ms
V^o's	55%	54%	48%	36%
K^o's	30%	30%	26%	20%
$K^o\Lambda$'s	9%	9%	7%	6%
Time/$K^o\Lambda$	2.7s	2.6s	3.3s	3.7s

Table 3.4

Timing in ROMEO

Initialization	0.23s	0.09%
Read Fid. record	7ms/call	1.75%
Read non Spark record	3ms/call	4.20%
Read Spark record	3ms/call	1.39%
Pattern Recognition	143ms/call	69.09%
Geometry	49ms/call	22.82%
Fiducial Module	0.32s	0.12%
Other time	1.12s	0.43%
Output of Events	0.30s	0.12%
Time per event	207ms	

Table 3.5

Breakdown of a single run by event types

V^0s	4166	71% (of non R2 triggers)
K^0s	1855	32% "
$K^0\Lambda$s	801	14% "
ΛK^0s	80	1% "
Λs	291	5% "
K^0K^0s	210	4% "

Table 3.6

Content of output tape for a single run

138 Fiducial Events
985 'Full' Events
1502 'Half' Events
122 Beam Events
214 $K^-/\bar{p}$ Events

Table 3.7

Results of eye scan of $K^0\Lambda$ candidates

Number of Events	Type	Number Expected
49	no Λ visible	55
6	Λ found	25
6	Λ there but not found	
5	Λ there but <8 sparks	16
19	Λ possibly there (≥ 1 track)	
4	Λ found but doubtful if real	
3	Λ found but event confused	
4	probably KK event	

Table 3.8

Reasons for failure of visible $K^0\Lambda$ events

Number of Events	Reason
1	1st 4 sparks in odd parity gaps
1	sign wrong for one track
1	1 track treated as 2
1	1 track turns through 360° - treated as 3 tracks
1	track appears to kink in 1 view
1	very narrow opening angle

Figure 3.1

Structure of the ROMEO Program

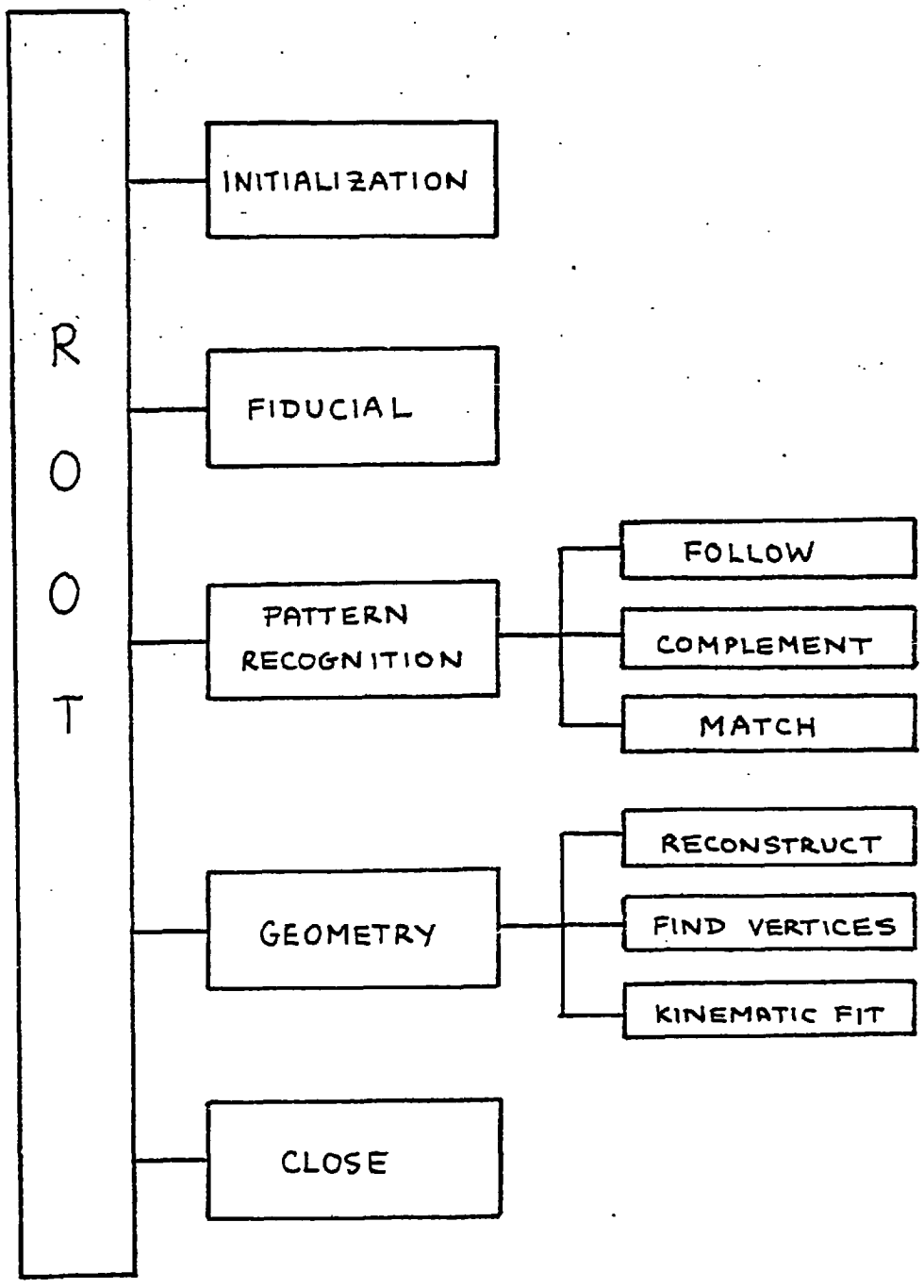


Figure 3.2

The Effects of the E Counter Cut

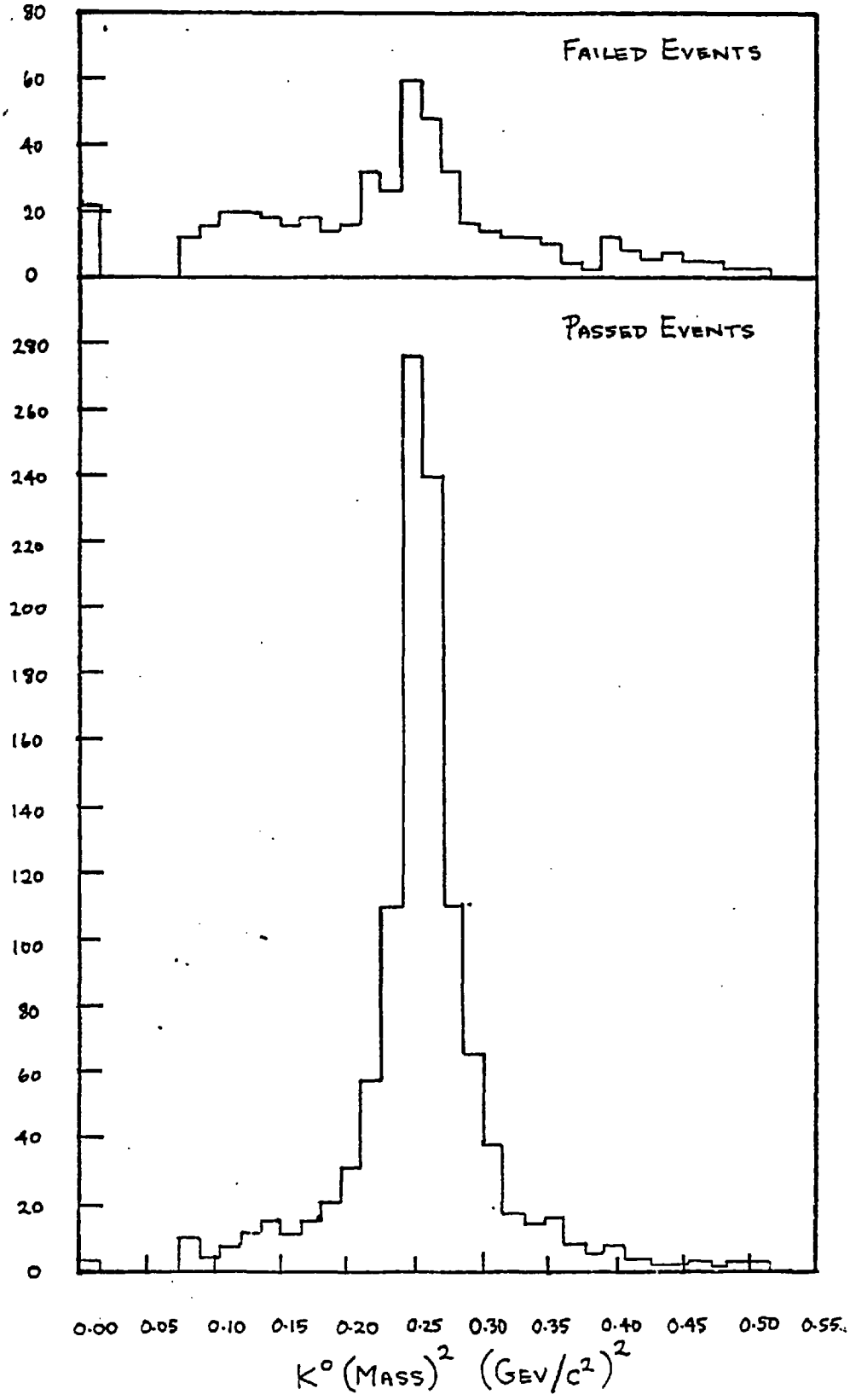


Figure 3.3

Logic Digram for Enrichment Runs

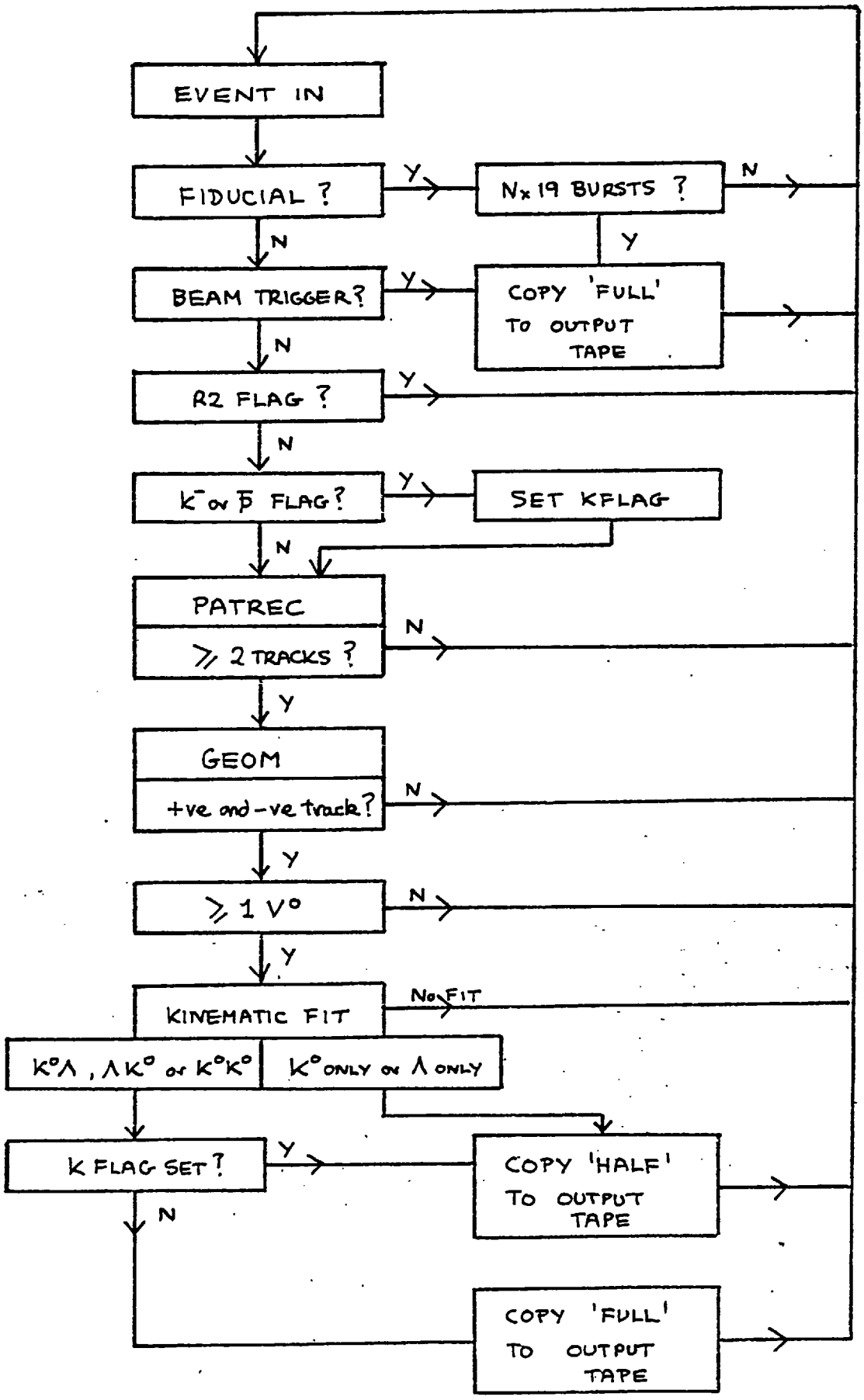


Figure 3.4

K^0 Mass Distribution

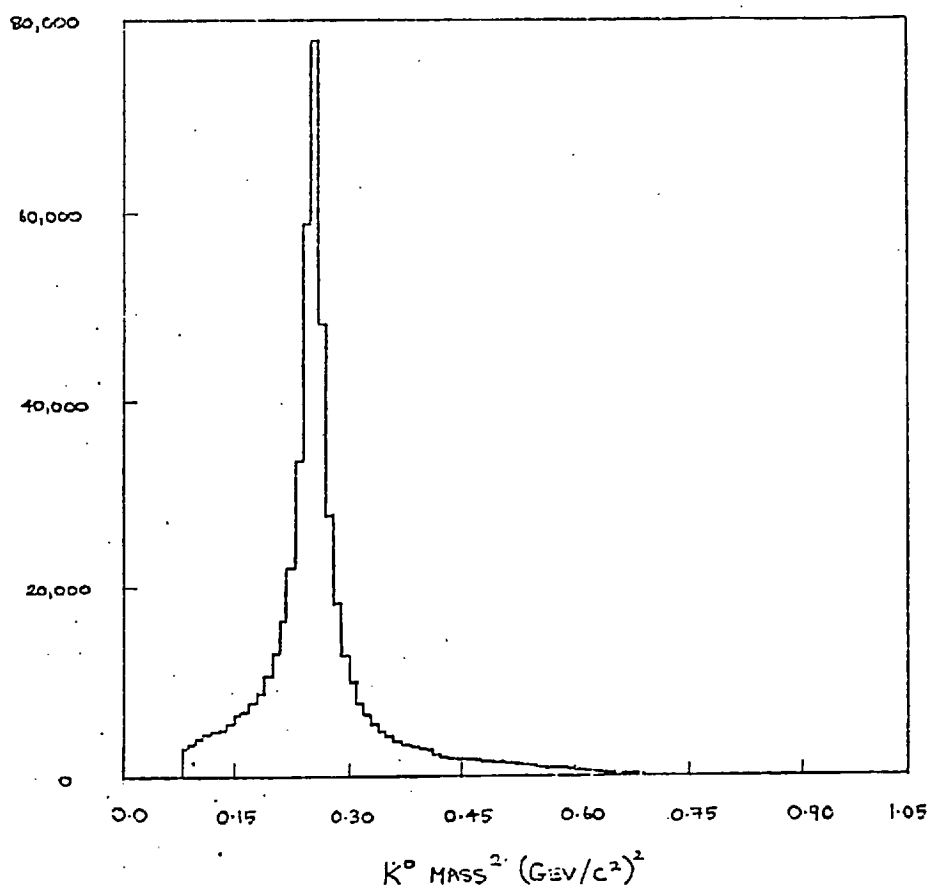


Figure 3.5

Lambda Mass Distribution

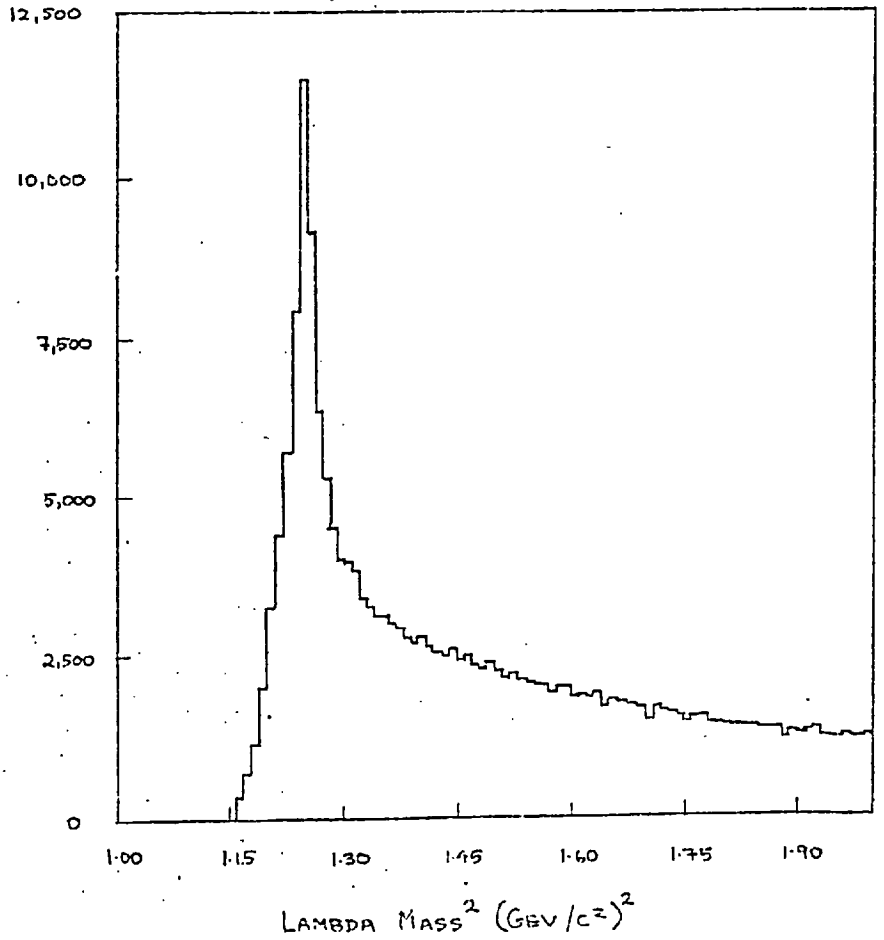


Figure 3.6

Missing Mass Squared to K^0

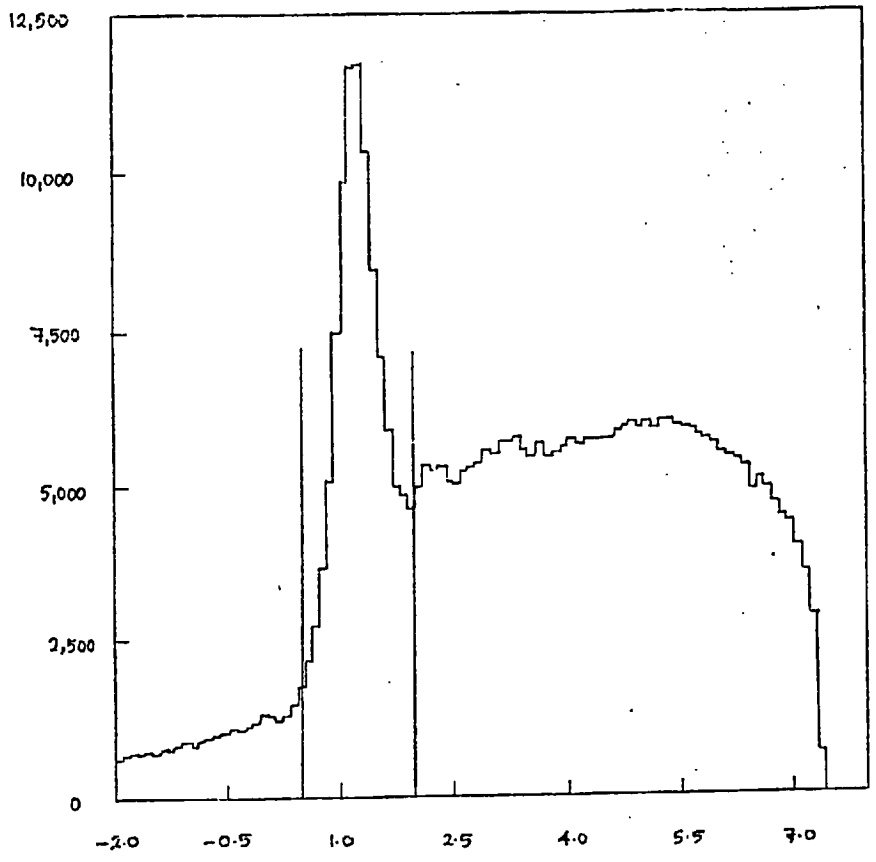
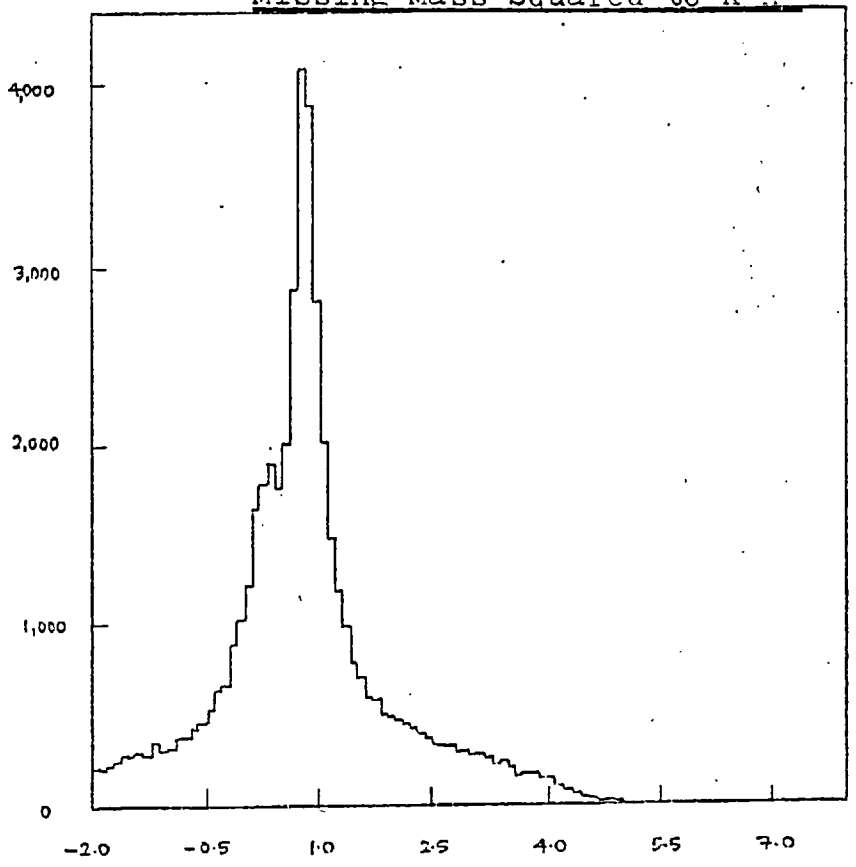


Figure 3.7

Missing Mass Squared to K^0K^0



CHAPTER 4

Analysis

4.1 Introduction

Because of the difficulty of recognising the recoil lambdas, as outlined in Chapter 3, it was decided to make a high statistics measurement of the polarization parameter P_o using the forward K^o data only, before attempting the full P_o, A and R analysis. This measurement is described in the remaining chapters.

4.2 Kinematic Fitting

The geometry output data on the enriched tapes contains information on the momenta and decay positions of the forward particles but does not identify the particles uniquely. Thus it was necessary to perform a kinematic fit to identify the event with possible decay and production hypotheses.

4.2.1 Beam Tracks

In order to fit the event to an interaction hypothesis it is necessary to know the parameters of the incoming beam particle. These parameters were obtained by analysing the events taken with the beam track trigger. ROMEO can

be easily modified to analyse these events by no longer requiring that pattern recognition finds more than one track. The distribution of measured momentum for the beam is shown in fig. 4.1 for one of these beam trigger runs. Because tracks are only visible downstream of the target the tracks were extrapolated upstream to get the azimuthal angle at the centre of the target.

The parameters of the beam are shown in Table 4.1. They are in good agreement with those expected from the beam optics. It was not necessary for this analysis to use the MWPC's to obtain the trajectory of every beam track individually.

There is another source of beam tracks. These are background beam tracks as discussed in 3.3.1. From fig. 4.1 and Table 4.1 one can see that the distributions of beam parameters are much broader than for triggered beam tracks. This is because they are mostly 'old' tracks and hence the ionization has drifted away from its original position before the chambers are pulsed, thus increasing the measurement errors.

4.2.2 The Fitting Program

A one constraint fit was performed at both the decay and interaction vertices separately. For each hypothesis a quantity χ^2 was defined by

$$\chi^2 = \sum_{i=1}^{n} \sum_{j=1}^{n} (q_i^{meas} - q_i^{fitted}) G_{ij} (q_j^{meas} - q_j^{fitted})$$

where $q_i = 1/p, \lambda, \phi$, the inverse momentum, dip and azimuthal angles for each track. $1/p$, λ and ϕ are chosen because their errors are approximately normally distributed. G_{ij} is the inverse of the external error matrix.

If $\bar{p}_1$, $\bar{p}_2$, m_1 and m_2 are the momenta and masses of the measured particles and m_o is the mass of the missing neutral particle then χ^2 was minimized subject to the constraint equation

$$f = \sqrt{\bar{p}_1^{\,2} + m_1^{\,2}} + \sqrt{\bar{p}_2^{\,2} + m_2^{\,2}} - \sqrt{(\bar{p}_1 + \bar{p}_2)^2 + m_o^{\,2}} = 0$$

The fit was deemed to have converged if the residual f after the n^{th} iteration was less than 0.1 MeV. The fit was abandoned if after any iteration χ^2 exceeded 100.

For each hypothesis a χ^2 probability $P(\chi^2)$ was calculated. On the basis of the $P(\chi^2)$ distribution a statistical choice between hypotheses could be made.

4.2.3 The Decay Vertex Fit

At the decay vertex the following hypotheses were tested

(1) $K^o s \rightarrow \pi^+ \pi^-$

(2) $\Lambda \rightarrow p \pi^-$

(3) $\bar{\Lambda} \rightarrow \bar{p} \pi^+$

(4) $\gamma \rightarrow e^+ e^-$

If s is the sagitta, L the length and ρ the projected radius of a track in cm. we can write (Ref. 11)

$$s \simeq \frac{(L\cos\lambda)^2}{8\rho}$$

For a 1T. field we have that $p=0.003\rho$ where p is in GeV/c. If we assume that the error in s is the spatial resolution σ_y we can write

$$\Delta(1/p) = \frac{8.\sigma_y}{0.003(L\cos\lambda)^2}$$

Assuming maximal correlation between the errors on 1/p and ϕ we can write

$$\Delta\phi = \frac{L\cos\lambda}{2}\,\Delta(1/\rho) = \frac{4.\sigma_y}{L\cos\lambda}$$

Similarly for the dip angle we can write

$$\Delta\lambda = \frac{4.\sigma_z}{L\cos\lambda}$$

These values of $\Delta(1/p)$, $\Delta\lambda$ and $\Delta\phi$ were fed into the error matrix. The values of σ_y and σ_z were then varied until the $P(\chi^2)$ distribution was flat as shown in fig. 4.2. The final values were: $\sigma_y = 0.5$mm.

$\sigma_z = 2$mm.

The value of σ_y is compatible with the value obtained from the residuals on the tracks. A cut on the distribution at low $P(\chi^2)$ eliminates those events which are not genuine K^0 decay without biasing the data.

4.2.4 The Interaction Fit

Events which satisfied the decay hypothesis $K^0s \rightarrow \pi^+\pi^-$ were subjected to a fit to $\pi^-p \rightarrow K^0\Lambda$ using the values of

the beam calculated in 4.2.1. The values and errors on the K^o were passed from the decay fit. The $P(\chi^2)$ distribution is shown in fig. 4.3.

Some events contained 2 K^o's. In these cases the K^o giving the highest $P(\chi^2)$ for the production fit was accepted. Distributions of $P(\chi^2)$ for the 'good' and 'bad' K^o are shown in fig. 4.4. It can be seen that the distribution for the 'good' K^o is the same as for single K^o events whereas the distributions for the 'bad' K^o is heavily peaked towards low $P(\chi^2)$.

4.2.5 Stretch Functions

The stretch (or pull) of a quantity q ($=1/p, \lambda, \phi$) to be fitted can be defined as

$$S_q = \frac{q(\text{unfitted}) - q(\text{fitted})}{\sqrt{\Delta q(\text{unfitted}))^2 - (\Delta q(\text{fitted}))^2}}$$

The distributions of these stretches are shown in fig. 4.5 and are expected to be gaussian with zero mean and unit standard deviation. All the stretches are consistent with this, which gives us confidence that the errors have been correctly estimated and that the values of the beam parameters are correct.

4.2.6 Cuts on the Data

In order to distinguish genuine $\pi^- p \rightarrow K^o \Lambda$ events from background, cuts were made on the data, requiring that

the $P(\chi^2)$ for both fits be $\geqslant 3\%$.

The effects of the cuts in reducing contamination from lambdas is discussed in the next section.

4.3 Contamination

One of the main sources of contamination comes from the reaction $\pi^- p \rightarrow \Lambda K^o$ (backward peak) where the lambda goes forward and is fitted as a K^o. Background from $\pi^- p \rightarrow K^o \Sigma^o$ is discussed in Chapter 5.

4.3.1 Decay Distributions

The lambda contamination can be estimated by looking at the distribution of $\cos\theta^*$ where θ^* is the angle between the direction of the positive decay product and the V^o direction in the centre of mass of the V^o.

If q is the momentum of the positive decay product in the V^o centre of mass and $q_\perp$ is its component perpendicular to the V^o direction then

$$\cos\theta^* = \left(1 - \left(\frac{q_\perp}{q}\right)^2\right)^{\frac{1}{2}}$$

For K^os $|q_K|^2 = 0.043\ (GeV/c)^2$ and for lambdas $|q_\Lambda|^2 = 0.01\ (GeV/c)^2$. If a genuine lambda fakes a K^o decay then $q_\perp \leq q_\Lambda$, but we fit the event as a K^o so that $q = q_K$.

Hence $$\cos\theta^* \geqslant \left(1 - \left(\frac{q_\Lambda}{q_K}\right)^2\right)^{\frac{1}{2}}$$

i.e. $$\cos\theta^* \geqslant 0.876$$

Thus lambda contamination will cause an enhancement in $\cos\theta^*$ above this value. We can see from fig. 4.6 that the amount of lambda contamination is quite large before the $P(\chi^2)$ cuts are applied. After the cuts have been applied however the amount of contamination is very small.

We can also see that the amount of antilambda contamination is negligible. This is not surprising since the threshold for $\bar{p}p \rightarrow \bar{\Lambda}$+anything is at 4.87 GeV/c. Thus the chances of producing a fast forward $\bar{\Lambda}$ are very small.

Since asymmetric K^{o}'s are as likely to fake lambdas as antilambdas and we know we have almost no antilambdas, one can estimate the amount of genuine lambda contamination from the ratio

$$\frac{\text{number of } \Lambda \text{ fits - number of } \bar{\Lambda} \text{ fits}}{\text{total number of events}}$$

After the $P(\chi^2)$ cuts have been applied this gives a value of 0.006 which is acceptably small.

4.3.2 Asymmetry in the Decay Distributions

The distributions shown in fig. 4.6 are for $|t| > 0.15$ $(\text{GeV/c})^2$. The distributions for all $|t|$ are shown in

fig. 4.7. It can be seen that there is an asymmetry in the distribution which peaks towards -ve $\cos\theta^*$ and is entirely due to events at $|t| \lesssim 0.15$ $(GeV/c)^2$. Possible causes of this asymmetry have been extensively investigated.

It is not clear whether this is really an enhancement at -ve $\cos\theta^*$ or a depletion at +ve $\cos\theta^*$. A depletion could be caused by some anomaly in the detection efficiency for fast forward K^os. In this case this asymmetry does not bias the polarization measurement, but merely cuts down the statistics, the effect being the same for spin up and spin down.

An enhancement could be caused by some non K^o background. If so these would be events with a fast negative track and a slow positive. The obvious source of fast negative tracks are beam tracks. Plots of momentum before the kinematic fits failed to show any enhancement around 5 GeV/c.

Slow positive particles could come from nuclear break up in the propanediol target or from interactions in the F counters. Since the effect is present both in Carbon and Hydrogen data, the former is excluded. Cuts on the x value of the decay position should show if the effect originates in the F counter region but nothing is observed.

The effect is still present if measured values are used instead of fitted ones to calculate $\cos\theta^*$. Hence the

kinematic fit is not causing this effect. Cuts on track length or residuals also fail to show any differences.

It was noted that the effect was more prominent in the early data and had gone away completely towards the end of the experiment and is hence probably caused by some initial misalignment somewhere in the apparatus which was later corrected.

If the asymmetry is due to non K^o events then one would expect these to be uniformly distributed in general and hence one would expect to see a changing lambda polarization with $\cos\theta^*$. This is investigated in Chapter 5 and no effect is seen. Hence we conclude that although the origin of this decay asymmetry is as yet not fully understood, it does not bias the polarization measurement in any way.

4.4 Experimental Precision

The precision of momentum and spatial measurements and their dependence on track lengths and clearing fields have been investigated by M.C.S. Williams (Ref. 8). Only points arising from this analysis are discussed here.

4.4.1 Spatial Precision

The spatial precision σ_y and σ_z can be expressed in terms of three quantities, σ_F the R.M.S. spark fluctuation,

σ_M the R.M.S. measurement error in each view and a stereo constant λ related to the stereo angle between the two views, in this case $=4.7$. Hence

$$\sigma_z = (\sigma_F^2 + 2\lambda^2\sigma_M^2)^{\frac{1}{2}}$$

$$\text{and } \sigma_y = (\sigma_F^2 + \tfrac{1}{2}\sigma_M^2)^{\frac{1}{2}}$$

Putting in our values of σ_y=0.5mm. and σ_z=2mm. we can solve to get

$$\sigma_M = 0.29\text{mm.}$$

$$\text{and } \sigma_F = 0.46\text{mm.}$$

M.C.S. Williams gets values of σ_M=0.13 and σ_F=0.35 but these were obtained from triggered beam tracks which are at well defined small angles and only involve one track in general. Hence one expects a better precision from triggered beam tracks.

A previous experiment using a similar setup (Ref. 10) but measurement by H.P.D. obtained σ_M=0.11mm. and σ_F=0.34mm. M.C.S. Williams finds that spatial precision falls linearly with increasing clearing field so that since we used a clearing field of 450v/cm. whereas previously only 125v/cm. had been used, the values of σ_M and σ_F are within expectations.

4.4.2 Accuracy in Determining the Decay Point

The distribution of the x value of the decay point is shown in fig. 4.8. The cutoff, corresponding to the downstream edge of the F counters, can be used to

calculate the error in the x position of the decay vertex position (Ref. 10)

$$\sigma(\text{x decay}) \simeq \tfrac{1}{2}\left[\text{x decay(max height)} - \text{x decay}(\tfrac{1}{2}\text{ max height})\right]$$

which gives a value of $\sim$ 1cm. for σ(x decay)

4.4.3 Accuracy in Determining the Interaction Point

Since no MWPC data was used and hence no accurate beam trajectory for each event, only an approximate value of the interaction point can be calculated. This is achieved by extrapolating the trajectory of the K^o back to the (x,y) plane at y=0. The distribution of x position is shown in fig. 4.9.

The distribution can be expressed as

$$N(x_{int}) = N_o \int_o^b e^{-\frac{(b-a)}{L_o}} \; e^{-\frac{(a-x)^2}{2\sigma^2}} \, da \; \frac{1}{\sigma\sqrt{2\pi}}$$

where b is the length of the target, σ is the measurement precision and L_o is the decay length of 4.8 GeV/c K^os (in this case 25.8cm.).

The first term arises from the cutoff due to the F counters, whilst the second is due to the measurement errors.

$N(x_{int})$ for σ=7cm. is shown in fig. 4.9. This is slightly worse than previous experiments where MWPC data has been used.

4.4.4 Momentum Precision

The momentum precision for this experiment calculated by M.C.S. Williams is shown in Table 4.2 for tracks which traverse the whole of the spectrometer from the downstream edge of the target i.e. $\sim$ 114cm.

4.4.5 Missing Mass Precision

The missing mass precision depends critically on the track lengths of the K^o decay products. The missing mass squared to the K^o is shown in fig. 4.10 for 2 different track length cuts. Only events with 1 K^o are included to remove some of the background from $K^o_s K^o_s n$. The $\Lambda(1520)$ is clearly visible.

Also plotted is the distribution obtained from a previous experiment by this group (Ref. 13) using the same apparatus but measurement by H.P.D. The precision is comparable for track lengths $\geqslant$ 110cm.

It can be seen that there is a slight asymmetry in the lambda peak for our distributions. Some of this asymmetry can be explained by fermi momentum in the target (Ref. 10). However the asymmetry is also present in data taken on the Hydrogen target. The origin of this asymmetry is discussed in Chapter 5.

4.4.6 t Precision

Let p_1, E_1, m_1 and p_3, E_3, m_3 be the momenta, energies and masses of the incident π^- and outgoing K^os. Let θ be the scattering angle. Then:

$$t = m_1^2 + m_3^2 - 2E_1E_3 + 2p_1p_3\cos\theta$$

Thus
$$\Delta t^2 = \left(\frac{2E_3p_1}{E_1} - 2p_3\cos\theta^2\right)^2\Delta p_1^2$$
$$+\left(\frac{2E_1p_3}{E_3} - 2p_1\cos\theta^2\right)^2\Delta p_3^2$$
$$+ (2p_3p_1\sin\theta)^2\Delta\theta^2$$

We find that $\Delta\theta$ is $\sim$ 0.005rad independent of t and with Δp_1=0.05 GeV/c from the momentum slit and Δp_3=0.12 GeV/c from the error on the fitted K^o we get the values of Δt listed in Table 4.3.

4.5 Event Losses

The losses and numbers of events at each stage of the data reduction and analysis are shown in Table 4.4. For the measurement of the polarization we are left with $\sim$ 435,000 events on polarized propanediol, approximately equally divided between spin up and spin down.

Table 4.1

Beam parameters

	Triggered	Background
$1/p$ (GeV/c)$^{-1}$	0.202 ± 0.001	0.200 ± 0.007
λ(rad)	-0.005 ± 0.008	-0.008 ± 0.011
ϕ(rad)	0.011 ± 0.008	0.012 ± 0.011

Table 4.2

Momentum precision for 114cm tracks

Momentum (GeV/c)	$\Delta p/p$
0.5	0.011
1.0	0.012
2.0	0.016
3.0	0.017
4.0	0.020
5.0	0.024

Table 4.3

t precision

$-t$ (GeV/c)^2	Δt
0.05	0.01
0.1	0.015
0.2	0.02
0.4	0.03
0.6	0.04
0.8	0.04
1.0	0.05
1.4	0.06
2.0	0.08

Table 4.4

Event losses during data reduction

Stage	% loss	Events remaining
Raw data		4,025,000
Initialization	0.2%	4,017,000
Pattern recognition	15%	3,414,000
Geometry	79%	717,000
Kinematics	18%	588,000
P(χ^2) cuts	26%	435,000

Figure 4.1

Beam Parameters

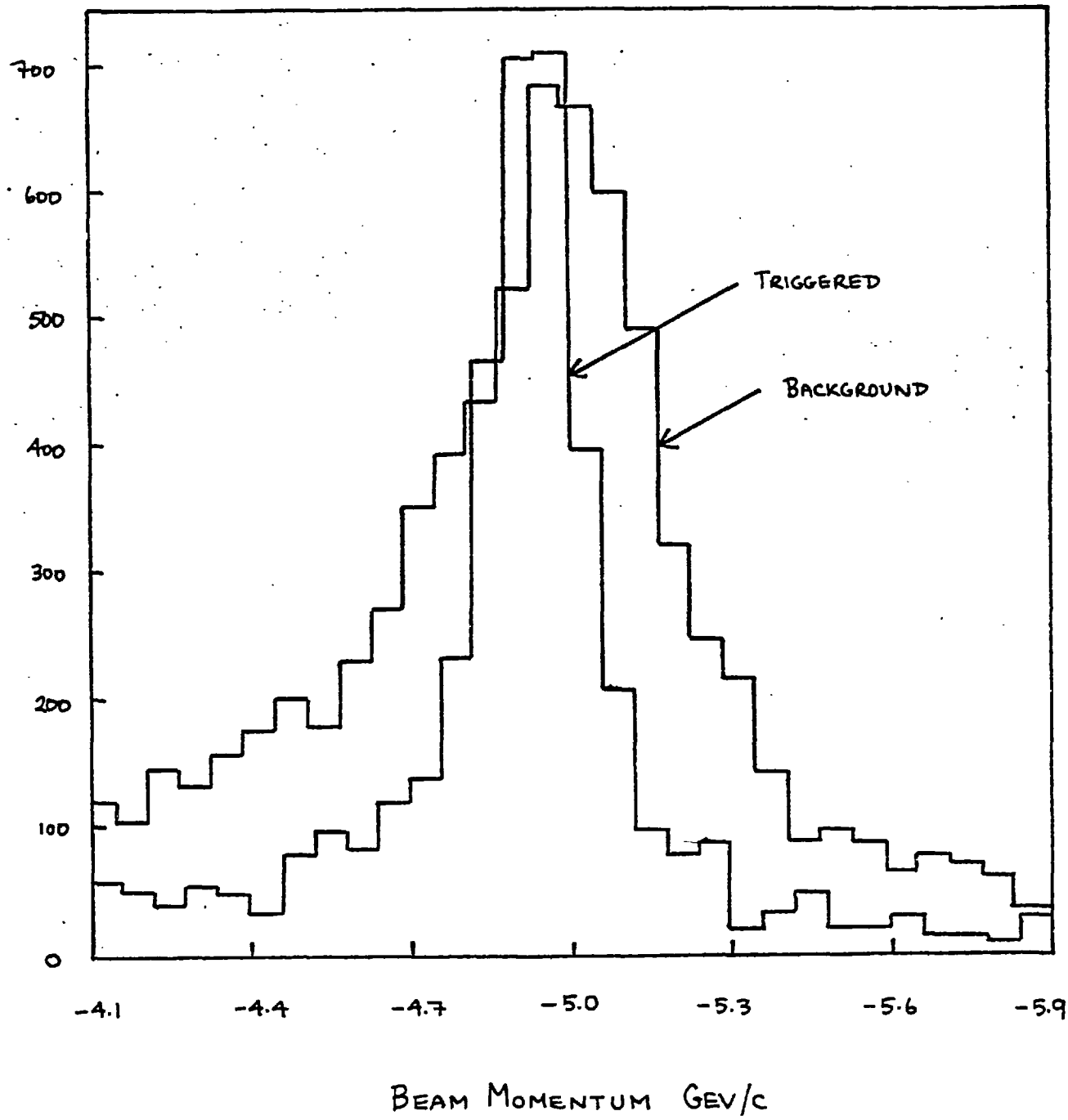


Figure 4.2

$P(\chi^2)$ Distribution for Decay

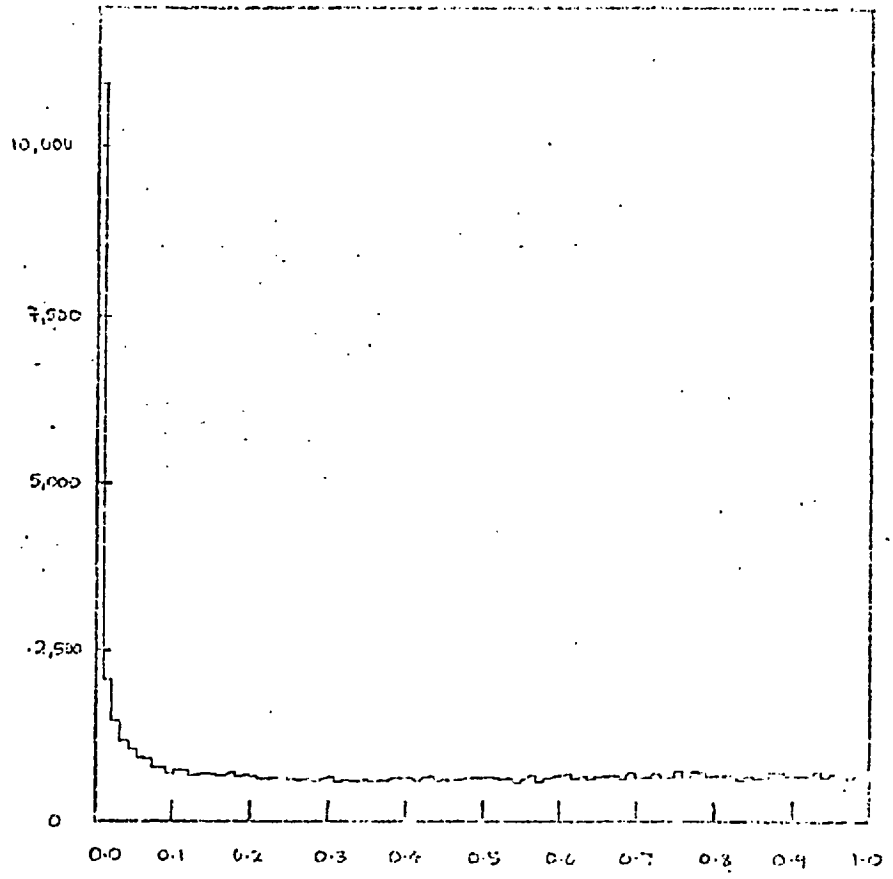


Figure 4.3

$P(\chi^2)$ Distribution for Interaction

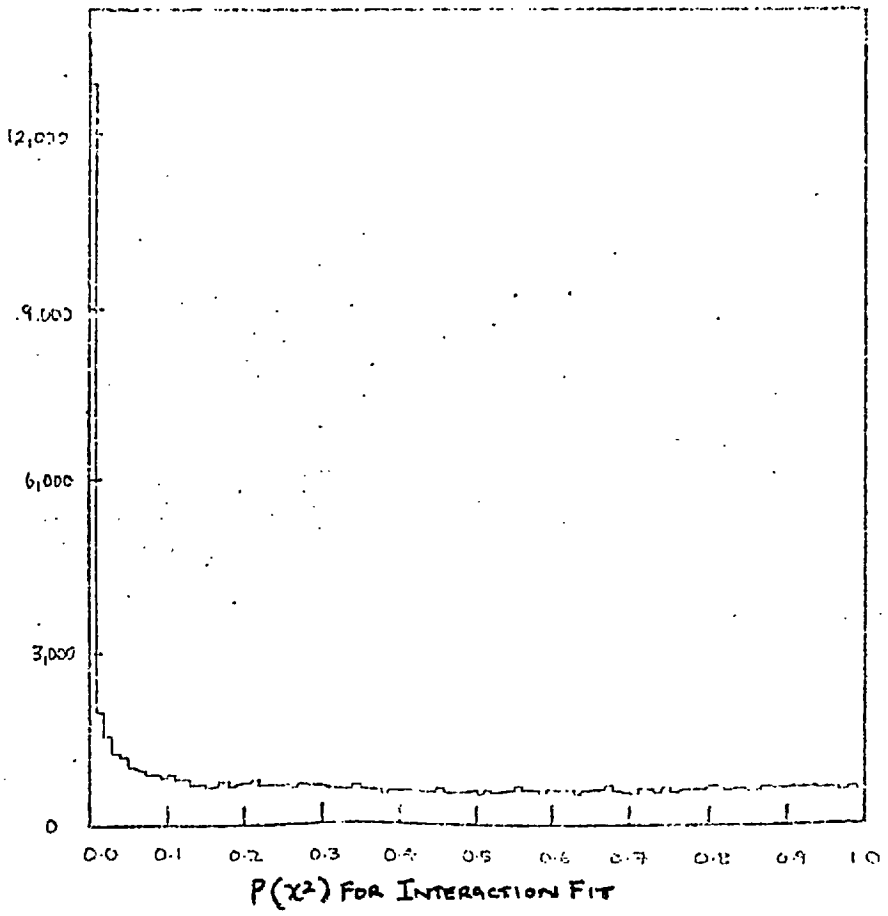


Figure 4.4

$P(\chi^2)$ For Double K^0 Events

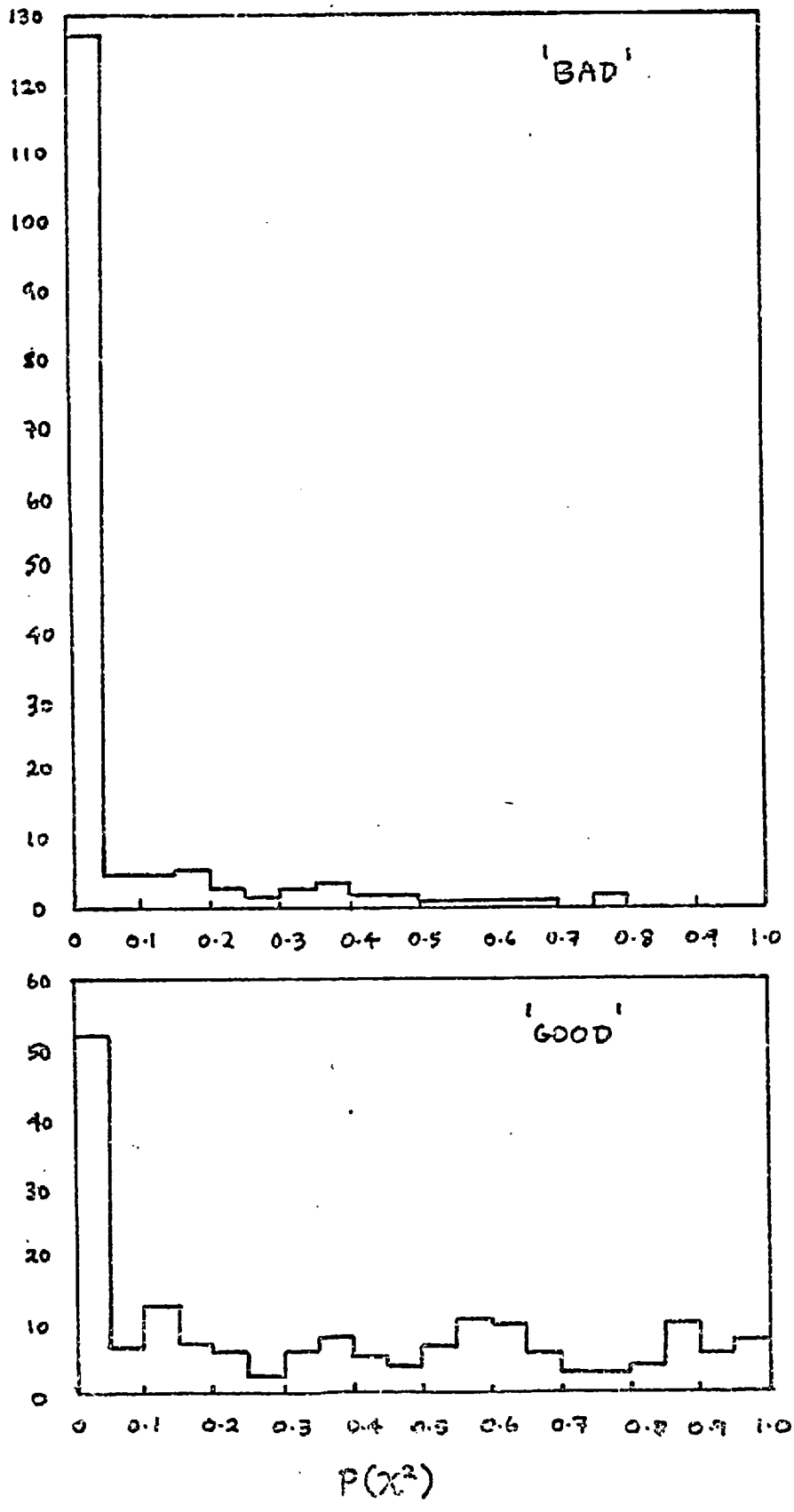


Figure 4.5

Stretch Functions

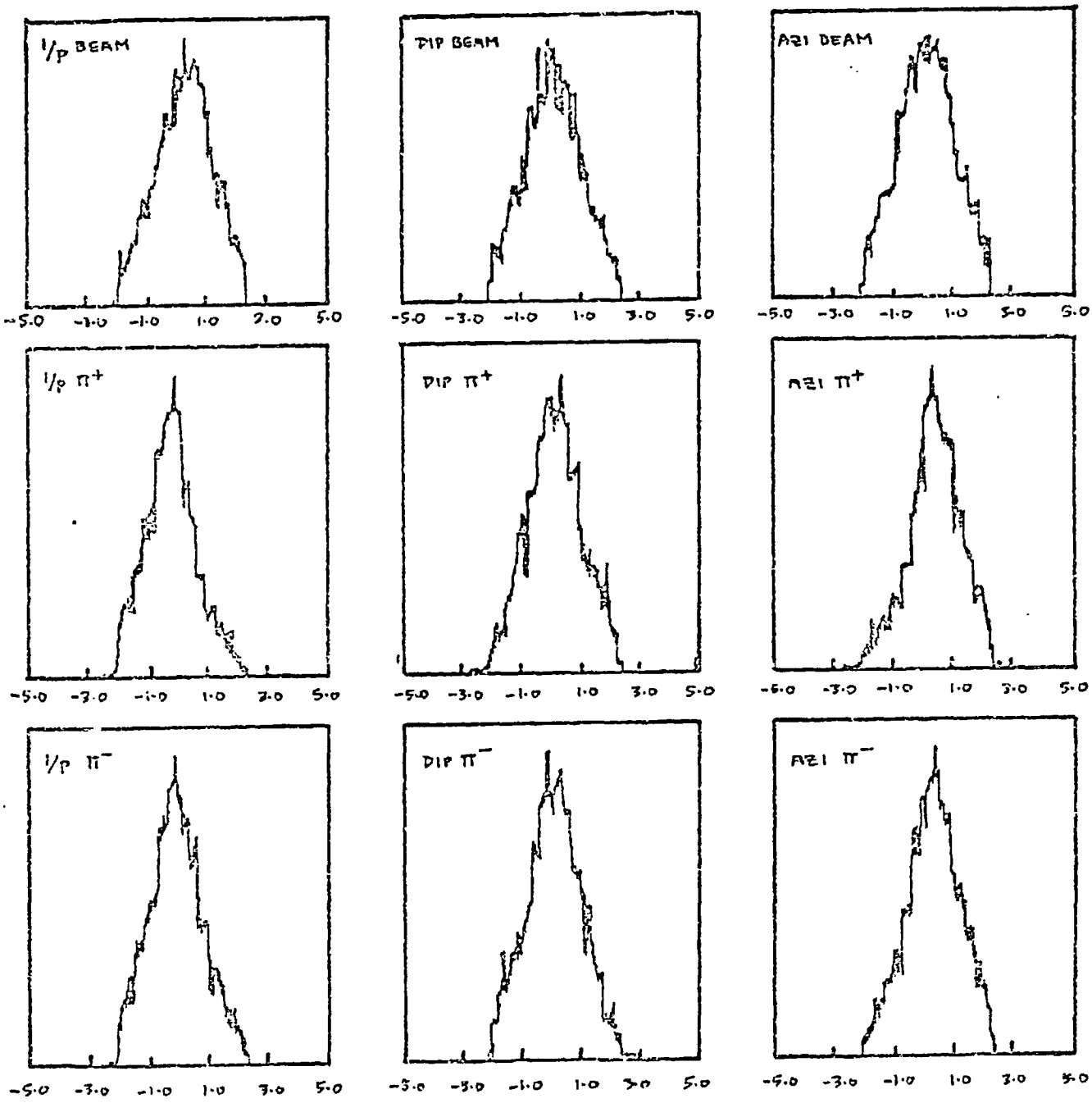


Figure 4.6

Centre of Mass Decay Angle for $-t > 0.15$ (GeV/c)^2

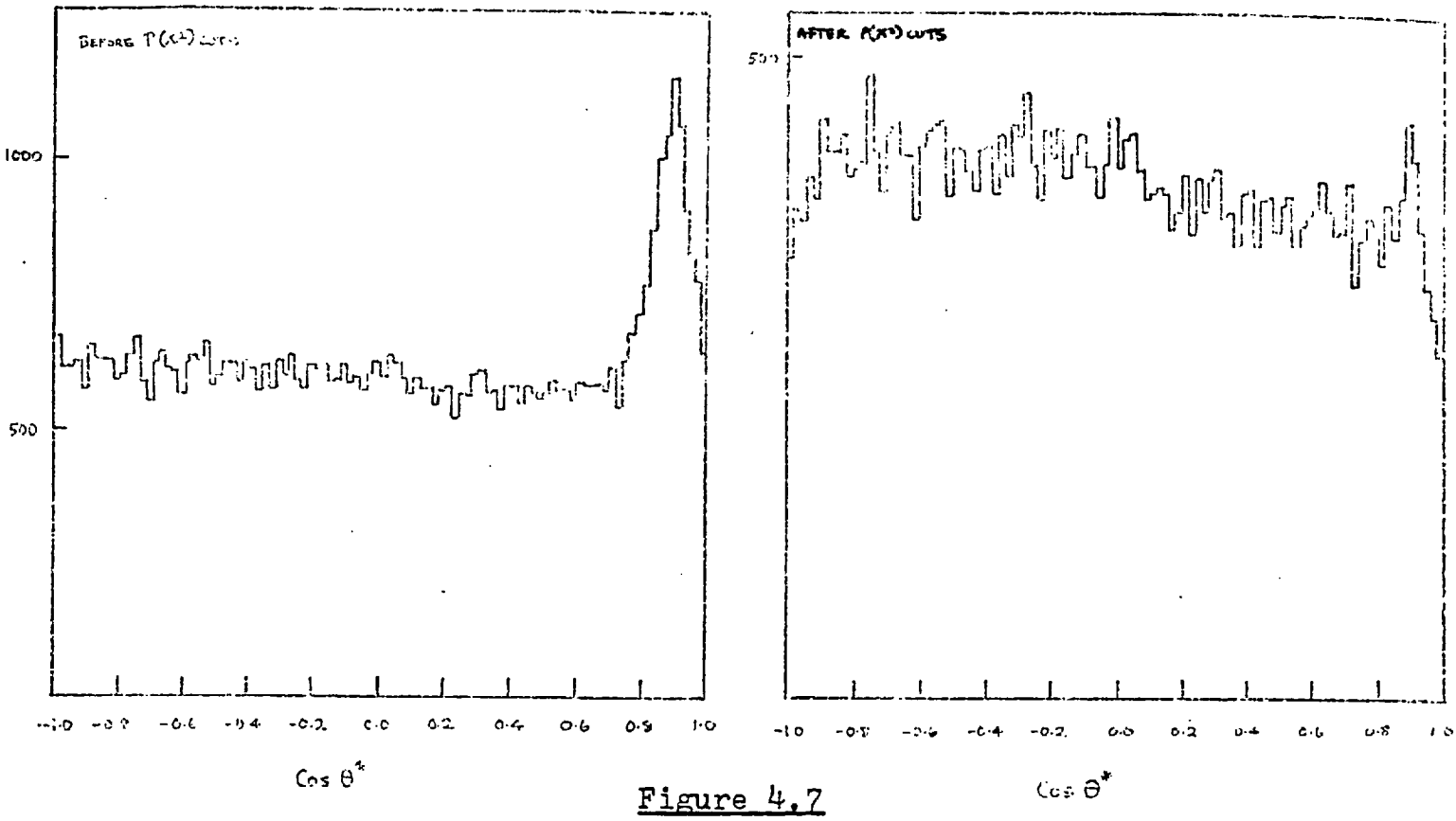


Figure 4.7

Centre of Mass Decay Angle for All t

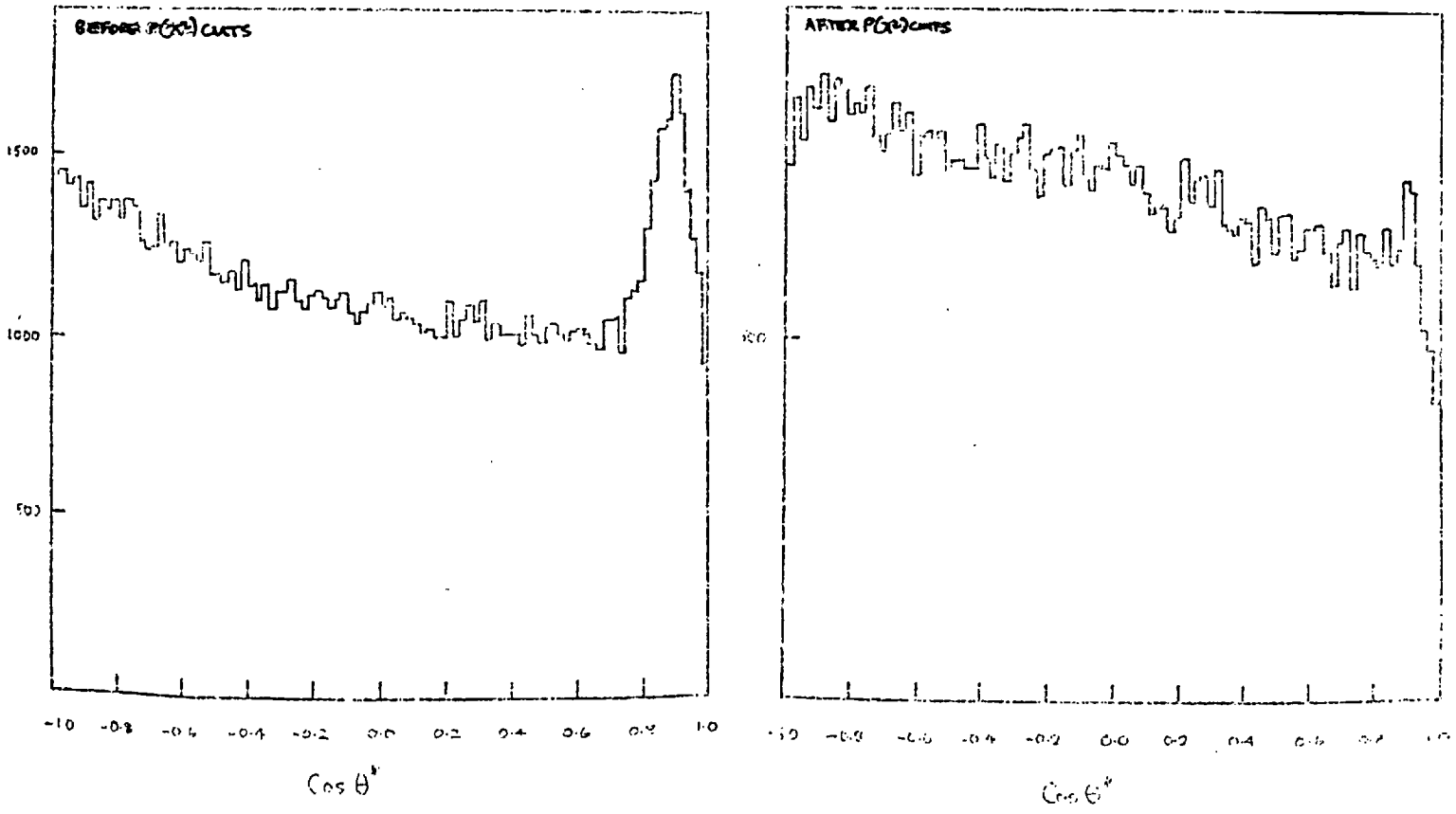


Figure 4.8

Distribution of K^0 Decay Point

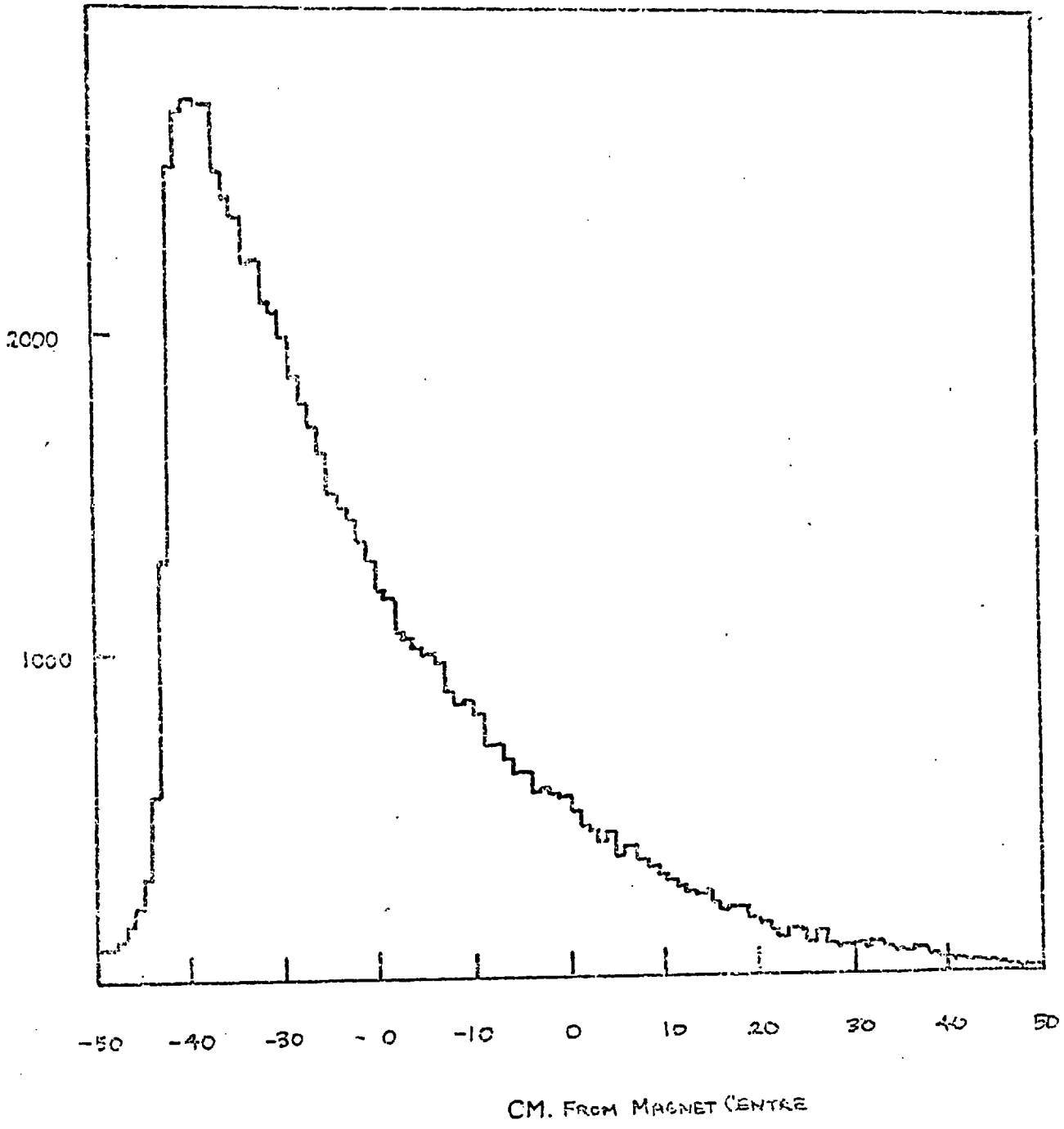


Figure 4.9

Distribution of Interaction Point

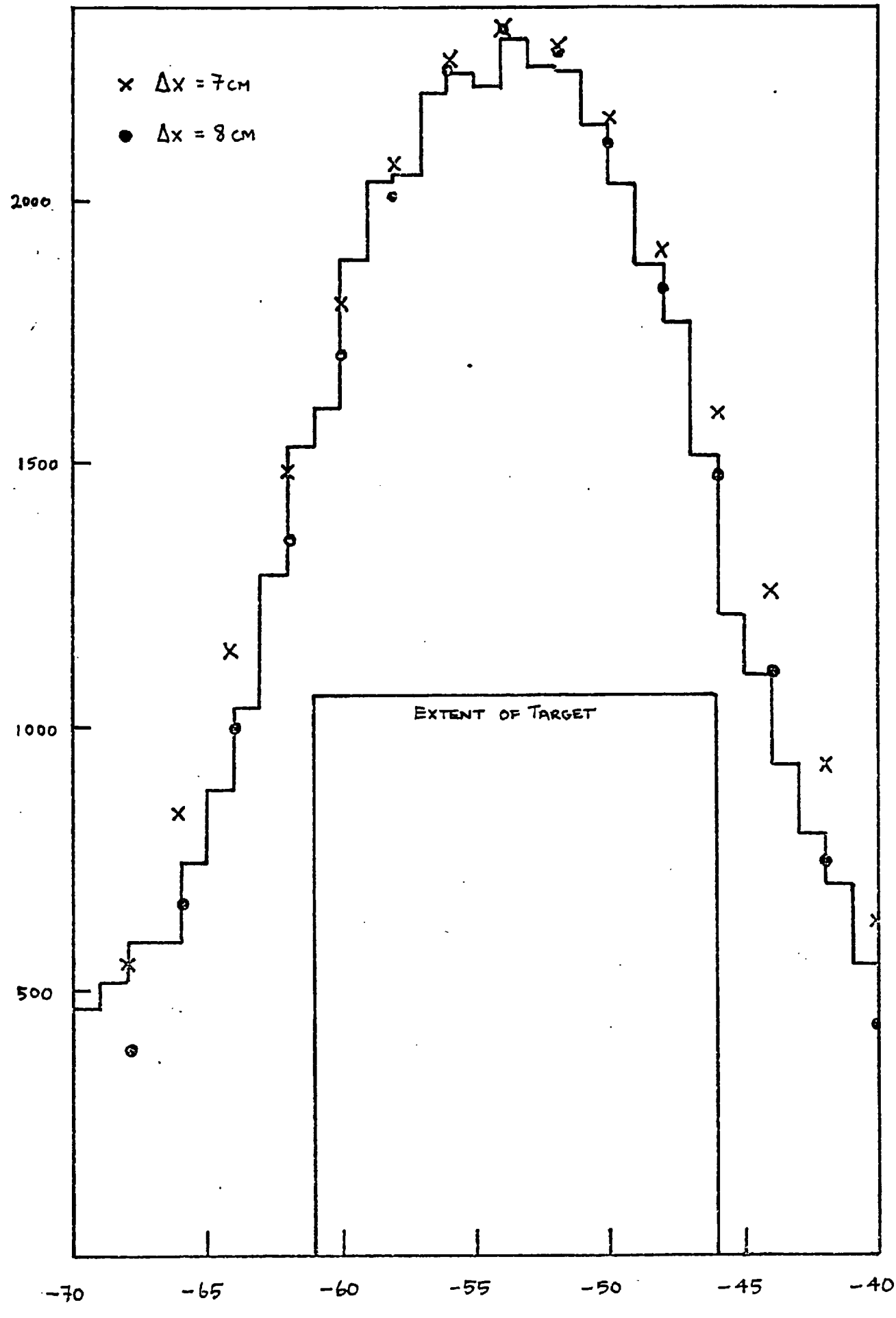
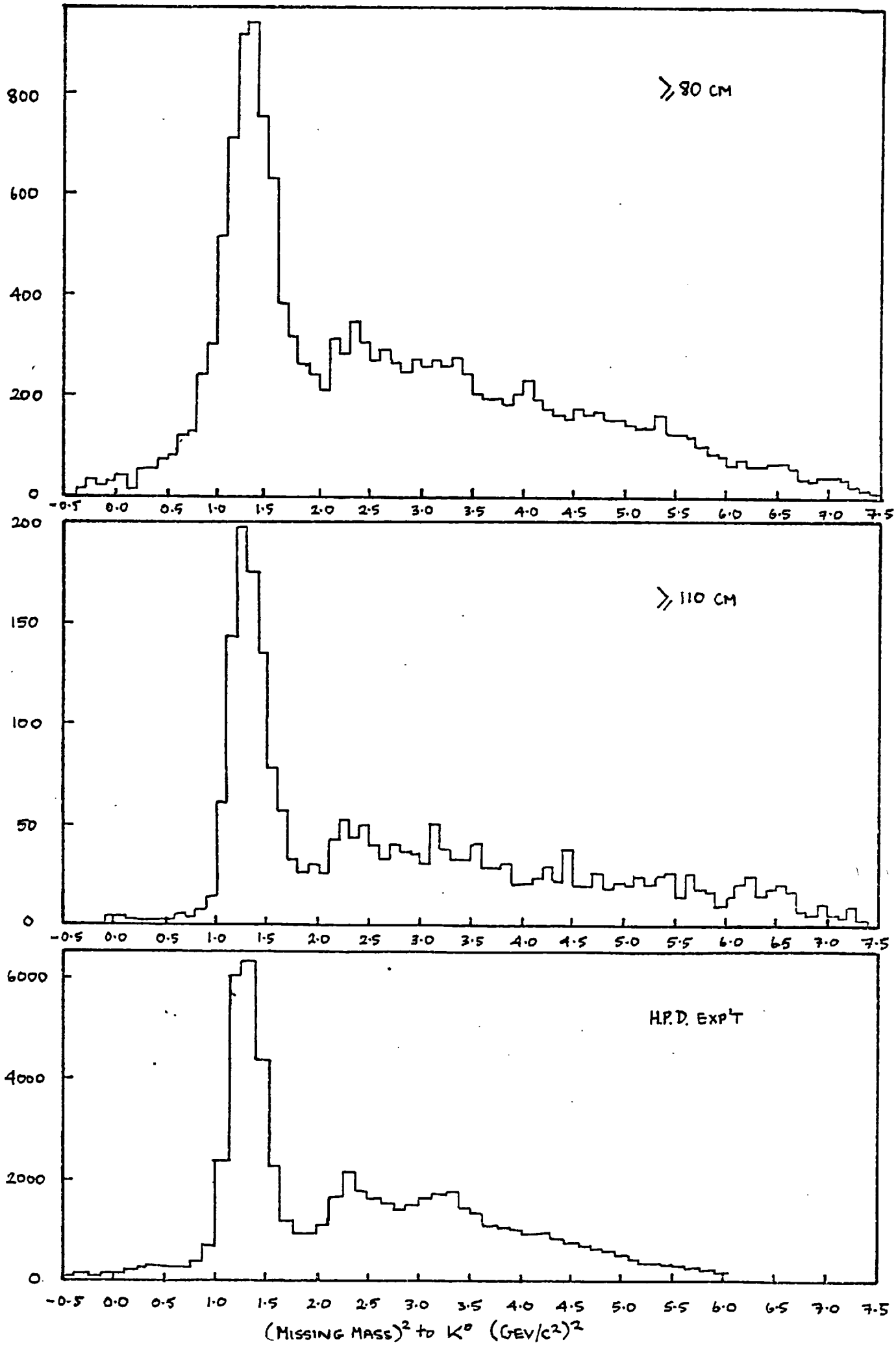


Figure 4.10 (MISSING MASS)^2 to K^0 for Different Track Lengths



CHAPTER 5

Experimental Results

5.1 Introduction

In this chapter the experimental asymmetry in the K^o production distribution and the ratio of all protons to free protons in the target are measured. The polarization parameter is calculated and using data off the Hydrogen target, the differential cross-section is measured.

5.2 The Experimental Asymmetry

5.2.1 Formalism

The measured differential cross-section on a polarized target can be written as

$$\left(\frac{d^2\sigma}{dt\,d\Omega}\right)_{\pm} = \left(\frac{d^2\sigma}{dt\,d\Omega}\right)_o (1 \pm P_o |\tilde{P}_T| \cos\phi)\ A(\phi, t)$$

where $\pm$ refer to target polarized up/down and o to the true differential cross-section on an unpolarized target. $A(\phi, t)$ is the experimental acceptance in the range $\phi \rightarrow \phi + d\phi$ and $t \rightarrow t + dt$. P_o is the polarization parameter and $|\tilde{P}_T|$ is the effective target polarization. $|\tilde{P}_T| = |P_T|/R$ where P_T is the polarization of free protons in the target and R is the ratio of all protons to free protons in the target

material which is discussed later in this chapter. ϕ is the angle between the direction of positive target polarization and the normal to the scattering plane n.

$$\hat{n} = \frac{\vec{K}_{\pi^-} \wedge \vec{K}_{K^o}}{|\vec{K}_{\pi^-} \wedge \vec{K}_{K^o}|}$$

where $\vec{K}_{\pi^-}$ and $\vec{K}_{K^o}$ are the directions of the incident π^- and the outgoing K^o.

For a small t range dt we have;

$$\left(\frac{d\sigma}{d\phi}\right)_{\pm} = \left(\frac{d\sigma}{d\phi}\right)_o (1 \pm P_o |\tilde{P}_T| \cos\phi)\ A(\phi) \quad - \quad 5.1$$

If n'_+ and n'_- are the number of events observed on target spin up and target spin down normalized to equal numbers of incident pions then

$$n'_{\pm} = \int_{\phi_1}^{\phi_2} \left(\frac{d\sigma}{d\phi}\right)_o (1 \pm P_o |\tilde{P}_T| \cos\phi)\ A(\phi) d\phi$$

We can define an experimental asymmetry α such that

$$\alpha = \frac{n'_+ - n'_-}{n'_+ + n'_-}$$

i.e. $$\alpha = P_o |\tilde{P}_T| \cdot \frac{\int_{\phi_1}^{\phi_2} A(\phi)\cos\phi d\phi}{\int_{\phi_1}^{\phi_2} A(\phi)\ d\phi} \quad - \quad 5.2$$

If $A(\phi)$ is constant then we have that

$$P_o |\tilde{P}_T| = \frac{\alpha}{\cos\phi} \quad - \quad 5.3$$

where $\overline{\cos\phi}$ is the mean value of $\cos\phi$ in the interval $\phi_1 \rightarrow \phi_2$. The error on α is discussed in Appendix 3.

5.2.2 Normalization

We need to normalize the number of events observed on each parity target to the number of pions incident on that target.

The number of incident pions is monitored throughout the run by counting the numbers of particles passing through the beam telescope. This number has to be corrected for accidental losses caused by pions passing through the veto counters.

Another method of normalization is to take events around $\cos\phi = 0$, where the number of events observed should be independent of the target polarization and hence proportional to the number of incident pions.

Because the scalers counting the numbers of pions were sometimes subject to pick up, every run would have to be carefully checked to ensure correct normalization. For this reason the second method was preferred since the data could still be used even if the scaler data was useless.

A carefully checked sample of 56,000 events where the scalers were known to be accurate was used to check the compatability of the two methods. Using uncorrected numbers of pions, the two methods agreed to within 1½% and with

the number of pions corrected for accidentals they agreed to within 0.2%. Thus we are justified in using the internal normalization method.

5.2.3 Maximum Likelihood Method

From equation 5.1 we have that the probability of an incident π^- producing an event at angle ϕ is

$$p_{\pm}(\phi)d\phi = RN\sigma A(\phi)d\phi\,(1 \pm P_o|\tilde{P}_T|\cos\phi)$$

where N is the number of free protons in the target and σ is the cross-section.

The probability of no event is

$$\bar{p}_{\pm} = 1 - RN\sigma(A_1 \pm A_2 P_o|\tilde{P}_T|\cos\phi)$$

where $A_1 = \int_0^{2\pi} A(\phi)d\phi$ and $A_2 = \int_0^{2\pi} A(\phi)\cos\phi d\phi$

The likelihood function for the experiment can now be written as

$$L = \prod_i^{n^+} p_+(\phi_i).\prod_1^{N^+-n^+} \bar{p}_+.\prod_j^{n^-} p_-(\phi_j).\prod_k^{N^--n^-} \bar{p}_-$$

where $n_{\pm}$ are the number of observed events on spin up and spin down and $N_{\pm}$ are the number of incident pions.

When L is a maximum so is ln L i.e.

$$\ln L = \sum_{i=1}^{n_+} \ln p_+(\phi_i) + (N^+ - n^+)\ln \bar{p}_+ + \sum_{j=1}^{n_-} \ln p_-(\phi_j) + (N^- - n^-)\ln \bar{p}_-$$

If we use $n_{\pm} = N_{\pm} R\sigma N(A_1 \pm A_2 P_o |\tilde{P}_T|)$ and differentiate with respect to P_o we get

$$\frac{\partial \ln L}{\partial P_o} = \sum_{i=1}^{n_+} \frac{|\tilde{P}_T| \cos\phi_i}{(1+P_o|\tilde{P}_T|\cos\phi_i)} - \sum_{j=1}^{n_-} \frac{|\tilde{P}_T|\cos\phi_j}{(1-P_o|\tilde{P}_T|\cos\phi_j)}$$

$$- (1 - \ln \bar{p}_+) RN\sigma A_2 |\tilde{P}_T| (N_+ - N_-)$$

Since $1 - \ln \bar{p}_+ \simeq 1$ we have at maximum likelihood

$$\sum_{i=1}^{n_+} \frac{\cos\phi_i}{(1+P_o|\tilde{P}_T|\cos\phi_i)} - \sum_{j=1}^{n_-} \frac{\cos\phi_j}{(1-P_o|\tilde{P}_T|\cos\phi_j)}$$

$$- A_2 RN\sigma(N_+ - N_-) = 0$$

Hence if $N_+ \simeq N_-$ we do not have to worry about any non-uniform acceptance.

If $P_o|\tilde{P}_T|$ is small c.f. 1 we can expand the denominator in a power series

$$\sum_{i=1}^{n_+} \cos\phi_i(1-P_o|\tilde{P}_T|\cos\phi_i) = \sum_{j=1}^{n_-} \cos\phi_j(1+P_o|\tilde{P}_T|\cos\phi_j)$$

$$\therefore \quad P_o|\tilde{P}_T| = \frac{\sum_{i=1}^{n_+} \cos\phi_i - \sum_{j=1}^{n_-} \cos\phi_j}{\sum_{i=1}^{n_+} (\cos\phi_i)^2 + \sum_{j=1}^{n_-} (\cos\phi_j)^2} \qquad - 5.4$$

5.2.4 Measurement of $P_o P_T$

Three methods were used to calculate $P_o|\tilde{P}_T|$. Firstly the acceptance $A(\phi)$ was assumed to be uniform and $P_o|\tilde{P}_T|$ was calculated from equation 5.3 in each of the 4 quadrants :

$$-\pi < \phi \leqslant -\pi/2$$
$$-\pi/2 < \phi \leqslant 0$$
$$0 < \phi \leqslant \pi/2$$
$$\pi/2 < \phi \leqslant \pi$$

This method provides a sensitive test of beam normalization. If $n_L^{\pm}$ and $n_R^{\pm}$ are the number of scatters into the left and right hand sides of the apparatus on targets up and down and $N_{\pm}$ are the number of incident pions, then since

$$P_o|\tilde{P}_T| \propto \left(\frac{n_+}{N_+} - \frac{n_-}{N_-}\right)\frac{1}{\overline{\cos\phi}}$$

and $\overline{\cos\phi_L} = 1$ and $\overline{\cos\phi_R} = -1$

then $$(P_o|\tilde{P}_T|)_L = \frac{n_L^+}{N_+} - \frac{n_L^-}{N_-}$$

and $$(P_o|\tilde{P}_T|)_R = -\frac{n_R^+}{N_+} + \frac{n_R^-}{N_-}$$

Thus if N_+ or N_- are incorrect they will produce apparently different polarizations on each side of the apparatus.

Values of $P_o P_T$ are shown for each quadrant in Table 5.1. There is good agreement and hence we conclude that the method of normalization used in 5.1.2 is correct.

Secondly, the acceptance functions A_1 and A_2 were calculated for all 4 quadrants using 43,000 events off the carbon target. The values of $(A_1/A_2).(2/\pi)$ are shown in Table 5.2.

$P_o|\tilde{P_T}|$ was then calculated from equation 5.2 and is shown in Table 5.3.

Finally $\cos\phi$ was calculated for each event and equation 5.4 used to calculate $P_o|\tilde{P_T}|$. This is the most accurate method and the one used to calculate the final polarization value. From Table 5.3 we see that it is compatible with the other 2 methods.

5.2.5 Checks on the Asymmetry

In order to be certain that the non-zero value of $P_o|\tilde{P_T}|$ was not caused by acceptance effects, $P_o|\tilde{P_T}|$ was measured for several values of $\cos\phi$ using the uniform acceptance method. As can be seen from fig. 5.1 the result is independent of $\cos\phi$.

As shown in 4.3.2 there is a non-uniformity in the K^o centre of mass decay angle. In order to prove that this was not biasing the results in any way, $P_o|\tilde{P_T}|$ was measured as a function of $\cos\theta^*$ where θ^* is the decay angle, for low -t where the effect is dominant. The results are shown in fig. 5.2 and we conclude that the non-uniformity does not bias the result.

Since the target was polarized in the vertical direction, any polarization effects in the final state should cause an asymmetry in the horizontal plane but not in the vertical. If the method of analysis is correct we should not see any preference for the K^o to go up or down (the basis for our normalization in 5.2.2). To check this $P_o|\tilde{P_T}|$ was measured assuming a target polarized in the horizontal plane and normalized to the number of incident pions. The result for a small sample of data is shown in fig. 5.3 and is consistent with zero as expected.

5.2.6 $P_o|\tilde{P_T}|$ as a Function of Missing Mass

In order to investigate the asymmetric distribution in missing mass squared to the K^o seen in 4.4.5, $P_o|\tilde{P_T}|$ was measured as a function of missing mass squared. Obviously if all the events are true K^o events then $P_o|\tilde{P_T}|$ should be constant.

From Table 5.4 we see that $P_o|\tilde{P_T}|$ decreases with increasing missing mass squared. This could be evidence for some contamination or be due to the fermi momentum in the target and be compensated for by an increase in R. The effect of the fermi momentum will be to broaden the distribution hence causing a decreasing asymmetry as one moves away from the lambda peak. In 5.3 it is shown that R does increase but not enough to explain the decrease in $P_o|\tilde{P_T}|$. This is discussed in more detail later.

5.3 The Effective Target Polarization $|\tilde{P}_T|$

As shown in Chapter 1 we can measure the polarization without having to separate bound protons from free protons kinematically, if we know the ratio R of all protons to free protons in the target. This was done using the Carbon and Hydrogen data.

Naively since propanediol $C_3H_8O_2$ has 42 protons of which 8 are free one would expect this ratio to be $42/8 = 5.25$. However this is reduced due to nuclear shadowing effects, i.e. interactions are more likely off protons towards the exterior of the nucleus. Another factor which reduces this ratio is that interactions with complex nuclei will produce nuclear fragmentation leading to several charged particles which may cause hits in the veto counters.

5.3.1 Run Selection

To calculate R one needs to know the event rate off different targets. Event rate is defined as the number of $\pi^- p \rightarrow K^o\Lambda$ events per incident pion. Careful checks were carried out to ensure that the event rates were correctly calculated and that the data were of good quality.

The event rate for each run off the various targets (propanediol, Carbon, Carbon + Helium, Hydrogen and target empty) was plotted as shown in fig. 5.4. Any run which was more than 2 standard deviations from the mean was

rejected as unreliable. Out of 493 runs considered, 22 were rejected on this basis.

The quality of the data was checked by looking at the percentage of potential $K^{o}\Lambda$ events found by ROMEO and applying the same criterion as above. Only 2 runs were rejected on this basis.

There was no evidence that the event rate was affected by any change in the upstream momentum slit setting.

The event rates for the selected runs are shown in Table 5.5. The rate for propanediol is not constant but seems to increase with time. This is probably due to improvements made to the camera system. For this reason only the data from run 1763 onwards was used for this calculation. The empty target data, taken at the start of the experiment, was scaled up to allow for this improvement - the effect on the calculation of R is very small.

5.3.2 Formalism

$$R = \frac{\text{number of events off polarized propanediol target}}{\text{number of events off free protons in propanediol}}$$

Let E(X) be the event rate on the target material X and ev(x) be the measured event rate i.e. E(Carbon) = ev(Carbon target) - ev(empty target)

Let R=R1.R2

where $$R2 = \frac{E(\text{propanediol})+E(\text{Target container})+E(\text{Helium})}{E(\text{propanediol})}$$

where E(Target container) and E(Helium) are due to events off the target container and the helium in the cryostat.

$$\text{Also let } R1 = \frac{E(\text{Propanediol})}{E(\text{free protons})}$$

R2 is easily calculated from the event rates of Table 5.5

$$R2 = \frac{ev(\text{propanediol})}{ev(\text{propanediol}) - ev(\text{empty}) - (ev(\text{carbon} + \text{He}) - ev(\text{carbon}))}$$

R2 is shown in fig. 5.5 and is independent of t.

$$R1 = \frac{\text{effective number of protons(bound and unbound)}}{\text{number of free protons in propanediol}}$$

If F_c and F_o are the effective numbers of bound protons in carbon and oxygen that can participate in the reaction then

$$R1 = \frac{3F_c + 2F_o + 8}{8}$$

The contribution from oxygen is discussed in the next section. If $F_o = KF_c$ where K is some constant then

$$R1 = \frac{(3 + 2K)}{8} F_c + 1 \qquad - \ 5.5$$

F_c is the ratio of the cross-sections on carbon and hydrogen targets. $F_c = \frac{\sigma_c}{\sigma_H}$ where the cross-section is given by

$$\sigma = \frac{A}{\rho} \cdot \frac{E}{N_{AV}}$$

where A is the atomic number, E the event rate, ρ the areal density and N_{AV} is Avogadro's number.

5.3.3 Oxygen Contribution

Since no data were taken to deduce the oxygen rate directly - such as using a H_2O target, the contribution

has to be estimated.

O. Guissan et al (Ref. 14) have studied the reactions

(a) $\pi^- A \rightarrow \pi^o A'$ and

(b) $\pi^- A \rightarrow \eta A'$

at 7.82 GeV/c where A is a nucleus and A' is the nucleus with 1 proton transformed into a neutron. Only γ's from forward π^o or η were detected and anticoincidence counters were employed to veto charged particles. Hence the effects of nuclear breakup can be expected to be similar to those in this experiment. The nuclei studied were ^{4}He, ^{6}Li, ^{7}Li, ^{12}C, ^{27}Al, ^{64}Cu and ^{27}Pb with $0.0 < -t < 0.5$ for (a) and $0.0 < -t < 0.75$ for (b).

If we parameterize the cross-section σ as

$$\sigma \propto \frac{Z}{A} A^N$$

and plot $\log \sigma A/Z$ against $\log A$, the data lies reasonably well on a straight line with N = 0.47. If only nuclei on the nuclear rim contribute then N = 0.33 whereas if the cross-section is proportional to the nuclear area then N = 0.66. One expects the true value to lie between these limits which is what is observed.

With N = 0.47 we get K = 1.14 hence

$$R1 = 1 + 0.66\ F_c \qquad - \quad 5.6$$

5.3.4 Values of F_c and R1

F_c the effective number of bound protons in carbon,

was calculated from the event rates and R1 was calculated from (5.6). The value of R is then obtained from R = R1.R2. Values of F_c, R1 and R are tabulated in Table 5.6.

As shown in Table 5.7 R1 is independent of the $P(\chi^2)$ cut for the interaction vertex. The t dependence is discussed later on.

5.3.5 Dependence of R on Missing Mass

In 5.2.6 it was shown that $P_o|\tilde{P}_T|$ decreased as the (missing mass)^2 to the K^o increased. In order to check whether or not this is compensated for by an increase in R, R was measured in different missing mass regions. The results are shown in Table 5.8. The polarization P_o is calculated from

$$\alpha = P_o|\tilde{P}_T|$$

$$= \frac{P_o|P_T|}{R}$$

The weighted average target polarization $|P_T|$ for each run whether positive or negative gave :-

$$|P_T| = 0.85 \pm 0.04$$

In fig. 5.6 P_o is plotted for the two regions (i) $MM^2 < 1.25$ and (ii) $1.25 < MM^2 < 1.55$. It can be seen that P_o is reduced in region (ii) especially at high -t. Thus there appears to be some contamination at high values of MM^2.

5.3.6 Sigma Contamination

From fig. 5.6 we see that for $-t > 0.4$ then the polarization for $1.25 < MM^2 < 1.55$ is approximately half the polarization for $MM^2 < 1.25$. Since $P_o(\pi^- p \to K^o \Sigma^o) \sim -P_o(\pi^- p \to K^o \Lambda)$ (Ref. 15), we can write that

$$\frac{P_o \text{measured}}{P_o \text{ real}} = \frac{N_\Lambda - N_\Sigma}{N_\Lambda + N_\Sigma}$$

where N_Λ and N_Σ are the number of Λ/Σ s in the region $1.25 < MM^2 < 1.55$.

Thus $\frac{N_\Lambda - N_\Sigma}{N_\Lambda + N_\Sigma} = \frac{1}{2}$ hence $\frac{N_\Sigma}{N_\Lambda + N_\Sigma} = 0.25$

This is equivalent to an overall Σ contamination of about 10% consistent with what one might expect from the inefficiency of the target veto counters.

In order to ensure that no sigmas are included in our final sample, a cut was made requiring that $MM^2 \leqslant 1.25$.

5.3.7 Consistency Checks on R1

As outlined in 5.3.2, R1 was calculated using the carbon and hydrogen data only. One can calculate R1 in two other ways using the ratio of the propanediol to the hydrogen data, and by using the propanediol and carbon data and doing a subtraction to find the hydrogen contribution.

Obviously all these three methods are not independent but do serve as a consistency check in case, for example,

the hydrogen cross-section is wildly wrong.

The values for R1 using the three methods

(a) $R1 = 1 + 0.66\,\sigma_{carbon}/\sigma_{hydrogen}$

(b) $R1 = \sigma_{propanediol}/8\sigma_{hydrogen}$

(c) $R1 = \sigma_{propanediol}/(\sigma_{propanediol} - 5.28\,\sigma_{carbon})$

are plotted in fig. 5.7 and it can be seen that they are in good agreement. Method (a) is the most accurate and is the one used for the final polarization measurement.

5.3.8 The Structure of F_c

F_c, the ratio of the cross-sections on carbon and hydrogen is plotted in fig. 5.8. F_c is essentially constant for $-t > 0.15(GeV/c)^2$ but peaks at low $-t$.

Kölbig and Margolis (Ref. 16) compute an effective nucleon number $N(A,\sigma_1,\sigma_2)$ which is the ratio of the cross-sections on that nucleus to that on free protons, and takes into account nuclear screening inside the nucleus.

$$N(A,\sigma_1,\sigma_2) = \left(\frac{d\sigma}{dt}\right)_A \Big/ \left(\frac{d\sigma}{dt}\right)_{\text{free protons}}$$

where A is the Atomic weight and σ_1 and σ_2 are the total cross-sections of particles 1 and 2 in $1 + A \rightarrow 2 + A'$ on Hydrogen. Interpolation of their results using $\sigma(\pi^- p) \sim 30mb$ and $\sigma(K^o p) \sim 20mb$ predicts that

$$\left(\frac{d\sigma}{dt}\right)_c \Big/ \left(\frac{d\sigma}{dt}\right)_H \sim 2.5$$

Kölbig and Margolis however do not take into account the effects of nuclear breakup causing hits in the anticoincidence counters, which would tend to lower this value.

The average value of F_c for $-t > 0.15(GeV/c)^2$ of ~ 2 is in good agreement with this prediction.

In $K^-p \rightarrow \bar{K}^0n$ (Ref. 10) F_c has been seen to decrease at low -t and this has been attributed to the Pauli exclusion principle preventing the production of a neutron in an already full nuclear level. In our experiment however the opposite effect has been observed. In order to explain this effect, Monte Carlo methods have been employed and are explained in the next section.

5.3.9 Monte Carlo

The Monte Carlo program SPRUCE (Ref. 17) was used to generate $\pi^-p \rightarrow K^0\Lambda$ events from stationary protons and from protons with fermi momentum to simulate both the carbon and hydrogen data.

Cuts were made on the generated events to take into account the effects of the veto counters. In the case of moving protons the events were weighted by a factor

$$\left(\frac{P'_{lab}}{5}\right)^{-1.93}$$

to take into account the variation of σ with $\sqrt{s}$. P'_{lab} is the equivalent lab energy of the beam to produce the same

centre of mass energy on a stationary proton. The factor of -1.93 (Ref. 18) is to account for the fact that the cross-section is higher if the incident π^- and the target proton are moving in the same direction, than if they are moving towards each other.

In fig. 5.8 we can see that there is indeed an enhancement at low -t values. At low -t the lambda goes forward as well as the K^o and the effect of the fermi momentum is to 'push' the lambda further forward so as to clear the F counters. Hence events which would have been vetoed if they had occurred on stationary protons now survive hence increasing the ratio of carbon to hydrogen cross-sections at low -t.

In fig. 5.9 the experimental acceptance of the apparatus is shown both for the charged decay $\Lambda \rightarrow p\pi^-$ and for the neutral decays $\Lambda \rightarrow n\pi^o$ where the π^o decays to $\gamma\gamma$.

5.4 Results

5.4.1 Polarization Parameter

$P_o|\tilde{P_T}|$ was measured using the maximum likelihood method for (missing mass)$^2 \lesssim 1.25$ in order to avoid any sigma contamination. R was measured in the same region. Since there is no reason to believe that there is any t dependence of R for $-t > 0.15$, in order to smooth out statistical fluctuations R was fitted to the expression

$$R = A_o + A_1 e^{A_2 t}$$

The fit was performed by minimization of χ^2 using the program MINUIT (Ref. 19). The values were found to be :

$$A_o = 2.25 \pm 0.17$$
$$A_1 = 4.43 \pm 1.41$$
$$A_2 = 11.82 \pm 4.11$$

R and $P_o|\tilde{P}_T|$ were combined with the target polarization $|P_T|$ to give the values of the polarization parameter P_o listed in Table 5.9 and plotted in fig. 5.10. The error on the target polarization is not included and hence there is an overall normalization error of $\sim 5\%$. Also plotted in fig. 5.10 are two previous measurements of P_o by Ward et al (Ref. 21) and Beusch et al (Ref. 13). It can be seen that there is good agreement with both previous results. Three high -t points of Ward et al are not included because they involve unphysical values of P_o.

P_o was also calculated for $2.0 < -t < 7.9$ $(GeV/c)^2$ where 7.9 $(GeV/c)^2$ corresponds to the maximum value of t or U_{min}. For this data a cut was made for $\cos\theta^* > 0.75$ for the K^o decay to eliminate lambda events faking K^o's. The values of P_o are plotted in fig. 5.11 over the whole t range along with the values measured in the backward peak by Astbury et al (Ref. 20). It can be seen that although the statistics are limited at high values of -t, the polarization is consistent with that measured in the backward peak.

Comparison of the values of P_o with the predictions of various phenomenological models is made in Chapter 6.

5.4.2 Differential Cross-section

Using the event rates calculated using the hydrogen target and the experimental acceptance calculated in 5.3.9 one can work out the differential cross-section $d\sigma/dt$. For the full P_o, A and R analysis one needs to measure $d\sigma/dt$ in order to determine the helicity amplitudes. We do not intend to measure $d\sigma/dt$ in this experiment but it is useful as a check.

There are several correction factors to be taken into account and these are listed below and tabulated in Table 5.10.

F1 takes into account the fact that only half of the events in the lambda peak have been used due to the cut imposed on the missing mass squared to the K^o. F2 and F3 take into account the branching ratios $K^o \rightarrow K^o_S$ and $K^o_S \rightarrow \pi^+\pi^-$.

F4 corrects the cross-section for losses caused by the 3% χ^2 cuts imposed on the data. F5, F6 and F7 are corrections for estimated losses due to the K^o's interacting inelastically in the F counters, absorption of the π^- or K^o in the target and inelastic lambda interactions in the R counters.

F8 is an estimated correction for δ rays produced by the beam causing hits in the veto counters. F9 is a

correction for losses due to inefficiencies in the pattern recognition estimated to be ~ 20%. The total correction factor is 9.04 ± 0.62. The main contribution to the uncertainty in this factor is due to the uncertainty in determining the pattern recognition efficiency.

The differential cross-section $d\sigma/dt$ is tabulated in Table 5.11 and fig. 5.12. It is in good agreement with previous measurements (Refs. 42 and 22). This gives us confidence that R has been correctly estimated and that the method of analysis is reasonably efficient.

Table 5.1

$P_o|\tilde{P}_T|$ for all quadrants assuming uniform acceptance

$-t$ (GeV/c)^2	1	2	3	4
0.0-0.05	0.017±0.012	0.004±0.012	0.019±0.012	0.009±0.011
0.05-0.10	0.006±0.012	0.023±0.012	-0.014±0.012	0.022±0.012
0.10-0.15	0.005±0.014	-0.003±0.014	0.033±0.014	0.023±0.014
0.15-0.20	0.034±0.017	0.041±0.017	0.040±0.017	0.050±0.016
0.20-0.25	0.023±0.020	0.046±0.019	-0.008±0.019	0.018±0.018
0.25-0.30	0.044±0.023	0.007±0.022	0.016±0.022	0.016±0.021
0.30-0.40	0.012±0.019	-0.003±0.019	-0.003±0.019	0.012±0.018
0.40-0.50	-0.033±0.025	-0.023±0.023	-0.062±0.023	0.029±0.023
0.50-0.60	-0.057±0.028	-0.085±0.028	-0.089±0.028	-0.068±0.026
0.60-0.80	-0.091±0.023	-0.105±0.023	-0.149±0.021	-0.120±0.022
0.80-1.00	-0.127±0.025	-0.115±0.025	-0.120±0.024	-0.165±0.026
1.00-1.30	-0.102±0.024	-0.097±0.025	-0.133±0.024	-0.135±0.025
1.30-1.65	-0.098±0.032	-0.099±0.031	-0.095±0.031	-0.101±0.032
1.65-2.00	-0.103±0.049	0.022±0.047	-0.046±0.046	-0.062±0.050

Table 5.2

Acceptance functions (A1/A2).2/π

$-t$ (GeV/c)^2	$-\pi < \phi \leq -\pi/2$	$-\pi/2 < \phi \leq 0$	$0 < \phi < \pi/2$	$\pi/2 < \phi \leq \pi$
0.0-0.2	-0.970	0.993	0.983	-0.980
0.2-0.4	-0.957	0.969	0.958	-0.953
0.4-0.8	-0.965	0.979	0.929	-0.951
0.8-1.2	-0.934	0.998	0.919	-0.897
1.2-1.8	-0.922	0.936	0.905	-0.851

Table 5.3

Values of $P_o|\tilde{P}_T|$

$-t$ (GeV/c)^2	With acceptance correction	Maximum likelihood
0.0-0.05	0.010 ± 0.006	0.010 ± 0.005
0.05-0.10	0.015 ± 0.006	0.005 ± 0.006
0.10-0.15	0.023 ± 0.007	0.010 ± 0.006
0.15-0.20	0.043 ± 0.008	0.034 ± 0.007
0.20-0.25	0.027 ± 0.010	0.016 ± 0.008
0.25-0.30	0.031 ± 0.011	0.023 ± 0.010
0.30-0.40	0.011 ± 0.010	0.004 ± 0.008
0.40-0.50	-0.032 ± 0.012	-0.038 ± 0.011
0.50-0.60	-0.070 ± 0.014	-0.081 ± 0.012
0.60-0.80	-0.115 ± 0.011	-0.120 ± 0.010
0.80-1.00	-0.142 ± 0.012	-0.141 ± 0.011
1.00-1.30	-0.116 ± 0.012	-0.119 ± 0.011
1.30-1.65	-0.085 ± 0.016	-0.083 ± 0.014
1.65-2.00	-0.051 ± 0.024	-0.050 ± 0.021

Table 5.4

$P_o|\tilde{P}_T|$ as a function of missing mass squared

$-t$ (GeV/c)^2	$MM^2 < 1.25$	$1.25 < MM^2 < 1.55$	$MM^2 > 1.55$
0.0-0.05	0.016 ± 0.011	-0.003 ± 0.013	-0.005 ± 0.015
0.05-0.10	0.015 ± 0.012	0.029 ± 0.013	-0.019 ± 0.015
0.10-0.15	0.030 ± 0.014	0.009 ± 0.016	0.009 ± 0.017
0.15-0.20	0.060 ± 0.016	0.035 ± 0.018	0.046 ± 0.020
0.20-0.30	0.015 ± 0.014	0.052 ± 0.017	0.021 ± 0.017
0.30-0.40	-0.021 ± 0.019	0.076 ± 0.022	0.032 ± 0.021
0.40-0.60	-0.066 ± 0.017	-0.058 ± 0.021	-0.033 ± 0.020
0.60-0.80	-0.196 ± 0.021	-0.094 ± 0.027	-0.048 ± 0.024
0.80-1.10	-0.223 ± 0.021	-0.150 ± 0.025	-0.041 ± 0.023
1.10-1.30	-0.249 ± 0.032	-0.100 ± 0.038	-0.048 ± 0.032
1.30-1.60	-0.225 ± 0.035	-0.094 ± 0.042	-0.002 ± 0.033
1.60-2.00	-0.136 ± 0.049	-0.124 ± 0.059	0.017 ± 0.041

Table 5.5

Event rates off different targets

Runs	Target	Events	Event rate x 10^6
500-527	empty	210	0.46 ± 0.03
530-568	unpolarized	3,143	3.58 ± 0.06
576-653	Propanediol	21,032	3.78 ± 0.03
1312-1375	Propanediol	26,253	4.81 ± 0.04
1376-1444	Carbon	18,570	3.73 ± 0.05
1465-1520	Propanediol	13,789	4.70 ± 0.05
1701-1755	Propanediol	14,860	4.81 ± 0.05
1763-1794	Carbon	8,306	4.00 ± 0.05
1795-1821	Carbon + Helium	6,982	4.23 ± 0.07
2510-2575	Propanediol	22,681	5.16 ± 0.07
3000-3092	Hydrogen	13,377	1.62 ± 0.02

Table 5.6

Values of F_c, R1 and R

$-t$ (GeV/c)^2	F_c	R1	R
0.0-0.05	9.98 ± 2.31	7.79 ± 1.57	10.90 ± 2.21
0.05-0.10	6.24 ± 0.92	5.24 ± 0.62	6.55 ± 0.79
0.10-0.15	4.24 ± 0.47	3.89 ± 0.32	4.89 ± 0.41
0.15-0.20	4.10 ± 0.60	3.79 ± 0.41	4.97 ± 0.55
0.20-0.25	3.71 ± 0.49	3.52 ± 0.33	4.55 ± 0.44
0.25-0.30	3.07 ± 0.31	3.09 ± 0.21	3.61 ± 0.27
0.30-0.40	3.68 ± 0.54	3.51 ± 0.36	3.95 ± 0.42
0.40-0.50	3.45 ± 0.66	3.34 ± 0.45	4.73 ± 0.65
0.50-0.70	3.53 ± 0.56	3.40 ± 0.38	4.23 ± 0.48
0.70-0.90	2.89 ± 0.35	2.96 ± 0.24	3.46 ± 0.29
0.90-1.30	2.33 ± 0.13	2.58 ± 0.09	2.75 ± 0.12
1.30-1.70	2.57 ± 0.44	2.75 ± 0.30	3.17 ± 0.36
1.70-2.00	2.60 ± 0.53	2.77 ± 0.36	3.31 ± 0.45

Table 5.7

Values of R1 for different P(χ^2) interaction cuts

-t (GeV/c)^2	3%	10%	50%
0.00-0.05	7.79 ± 1.57	8.88 ± 2.32	7.32 ± 1.89
0.05-0.10	5.24 ± 0.62	5.28 ± 0.68	4.74 ± 0.58
0.10-0.15	3.88 ± 0.32	3.73 ± 0.28	3.85 ± 0.44
0.15-0.20	3.79 ± 0.41	3.83 ± 0.43	4.62 ± 1.17
0.20-0.25	3.52 ± 0.33	3.55 ± 0.36	3.83 ± 0.44
0.25-0.30	3.09 ± 0.21	3.14 ± 0.26	3.11 ± 0.16
0.30-0.40	3.51 ± 0.36	3.47 ± 0.37	3.84 ± 0.69
0.40-0.50	3.34 ± 0.45	3.15 ± 0.39	2.71 ± 0.15
0.50-0.70	3.40 ± 0.38	3.47 ± 0.41	3.40 ± 0.52
0.70-0.90	2.96 ± 0.24	2.87 ± 0.22	2.78 ± 0.16
0.90-1.30	2.58 ± 0.09	2.53 ± 0.10	2.48 ± 0.20
1.30-1.70	2.75 ± 0.30	2.75 ± 0.38	2.58 ± 0.65
1.70-2.00	2.77 ± 0.36	2.54 ± 0.23	2.20 ± 0.15

Table 5.8

Values of R as a function of missing mass squared

$-t$ (GeV/c)^2	$0.75 < MM^2 < 1.25$	$1.25 \leq MM^2 \leq 1.55$	$1.55 < MM^2 < 1.95$
0.00-0.05	6.91 ± 1.04	12.00 ± 3.93	-5.43 ± 5.99
0.05-0.10	4.95 ± 0.70	8.43 ± 1.88	7.39 ± 2.61
0.10-0.15	3.64 ± 0.38	5.84 ± 0.89	7.28 ± 2.12
0.15-0.20	3.23 ± 0.27	7.41 ± 2.17	12.30 ± 12.62
0.20-0.25	3.12 ± 0.22	6.37 ± 1.45	8.34 ± 6.04
0.25-0.30	2.66 ± 0.23	5.16 ± 0.81	4.41 ± 1.08
0.30-0.40	2.79 ± 0.31	4.98 ± 1.25	6.02 ± 1.50
0.40-0.50	3.10 ± 0.30	4.75 ± 1.24	24.94 ± 64.07
0.50-0.70	2.97 ± 0.26	5.45 ± 1.59	10.48 ± 9.43
0.70-0.90	2.38 ± 0.18	3.27 ± 0.33	21.21 ± 40.64
0.90-1.30	2.22 ± 0.14	2.86 ± 0.23	4.29 ± 0.69
1.30-1.70	3.62 ± 0.99	2.68 ± 0.40	4.48 ± 1.64
1.70-2.00	3.14 ± 0.47	3.18 ± 0.66	5.36 ± 5.11

Table 5.9

Values of the polarization parameter P_o

$-t$ (GeV/c)^2	P_o
0.00-0.05	0.099 ± 0.153
0.05-0.10	0.039 ± 0.071
0.10-0.15	0.079 ± 0.082
0.15-0.20	0.168 ± 0.110
0.20-0.25	0.119 ± 0.077
0.25-0.30	0.016 ± 0.064
0.30-0.40	-0.051 ± 0.054
0.40-0.50	-0.133 ± 0.070
0.50-0.60	-0.210 ± 0.085
0.60-0.70	-0.408 ± 0.115
0.70-0.90	-0.660 ± 0.149
0.90-1.15	-0.570 ± 0.134
1.15-1.40	-0.537 ± 0.139
1.40-1.70	-0.557 ± 0.157
1.70-2.00	-0.406 ± 0.181
2.0-2.5	-0.24 ± 0.20
2.5-3.0	-0.39 ± 0.34
3.0-4.0	-0.16 ± 0.31
4.0-5.0	-0.31 ± 0.36
5.0-6.0	0.03 ± 0.35
6.0-7.0	1.09 ± 0.43
7.0-7.9	0.56 ± 0.76

Table 5.10

Corrections to the differential cross-section

$\frac{1}{2}\Lambda$ peak cut	F1 = 2.0 ± 0.05
$K^o s \rightarrow \pi^+\pi^-$ B.R.	F2 = 1.46
$K_o \rightarrow K^o s$	F3 = 2.0
losses due to $P(\chi^2)$ cuts	F4 = 1.06
K^o interactions in F counters	F5 = 1.03
Absorption in target	F6 = 1.04
Λ interactions in R counter	F7 = 1.06
δ ray production	F8 = 1.03
Pattern Recognition losses	F9 = 1.25 ± 0.08
Total correction factor = $\prod F_i$ = 9.04 ± 0.62	

Table 5.11

Values of the differential cross-section

$-t$ (GeV/c)^2	$d\sigma/dt$ (μb/(GeV/c)^2)
0.0-0.05	258 ± 45
0.05-0.10	177 ± 31
0.10-0.15	122 ± 16
0.15-0.20	93.1 ± 9.9
0.20-0.25	63.8 ± 4.8
0.25-0.30	43.4 ± 4.2
0.30-0.40	21.5 ± 3.2
0.40-0.50	14.9 ± 1.8
0.50-0.70	8.38 ± 0.93
0.70-0.90	6.31 ± 0.51
0.90-1.30	4.00 ± 0.32
1.30-1.70	0.86 ± 0.36
1.70-2.00	1.39 ± 0.28

Figure 5.1

$P_o|\tilde{P_T}|$ as a Fuction of $\cos\phi$

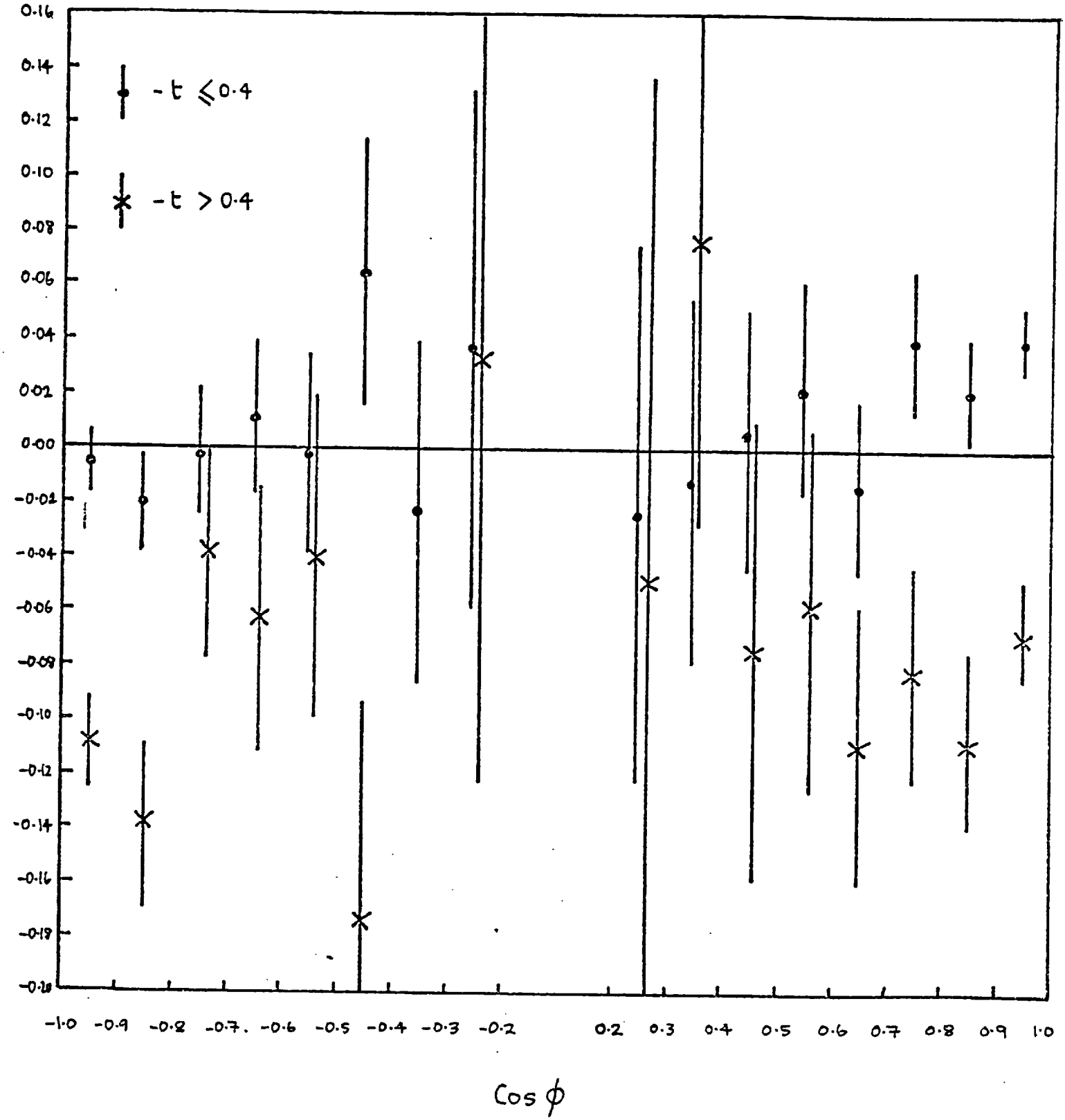


Figure 5.2

$P_o|\tilde{P}_T|$ as a Function of Decay Angle

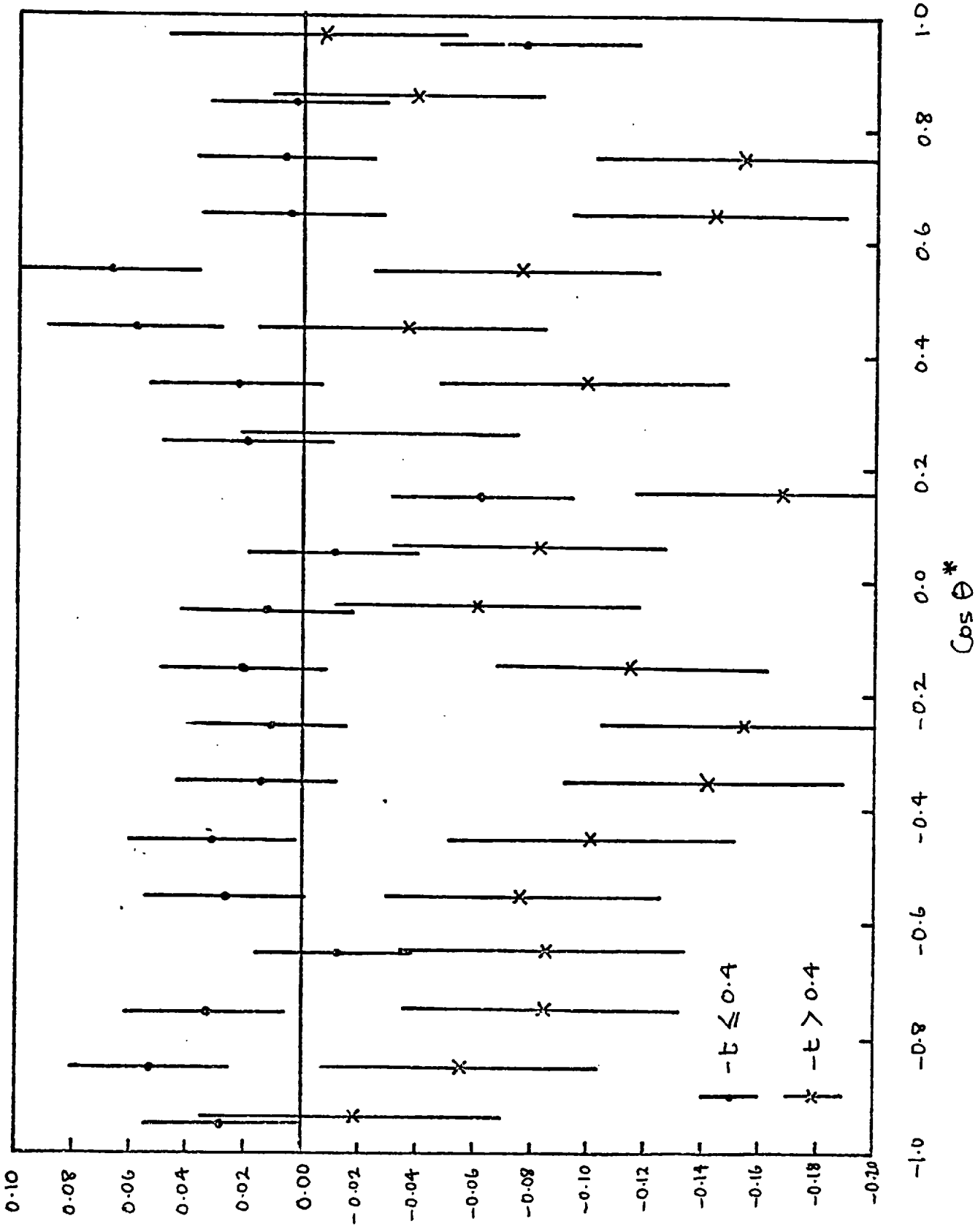


Figure 5.3

'Parity Violating' Asymmetry

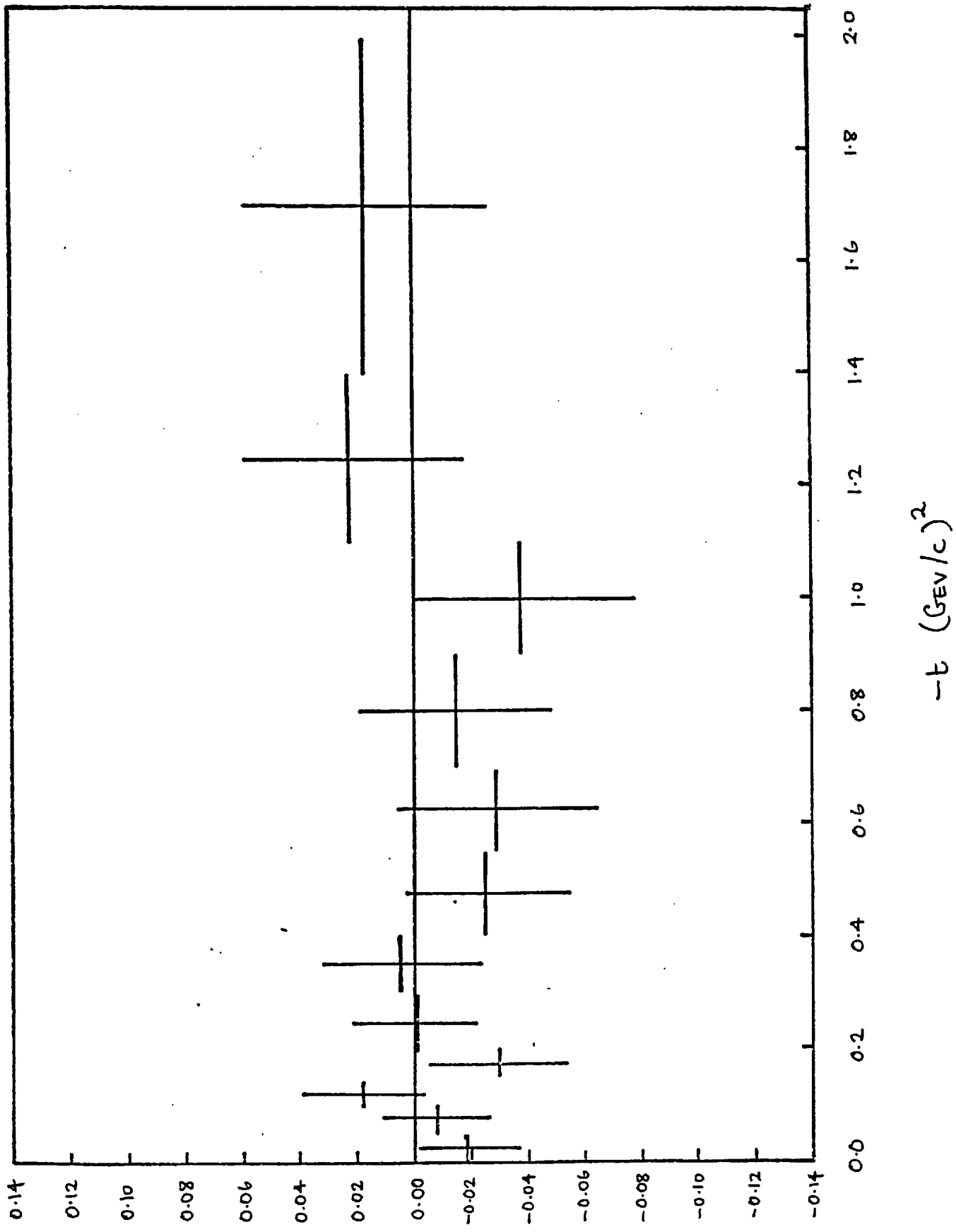


Figure 5.4

Sample Event Rates

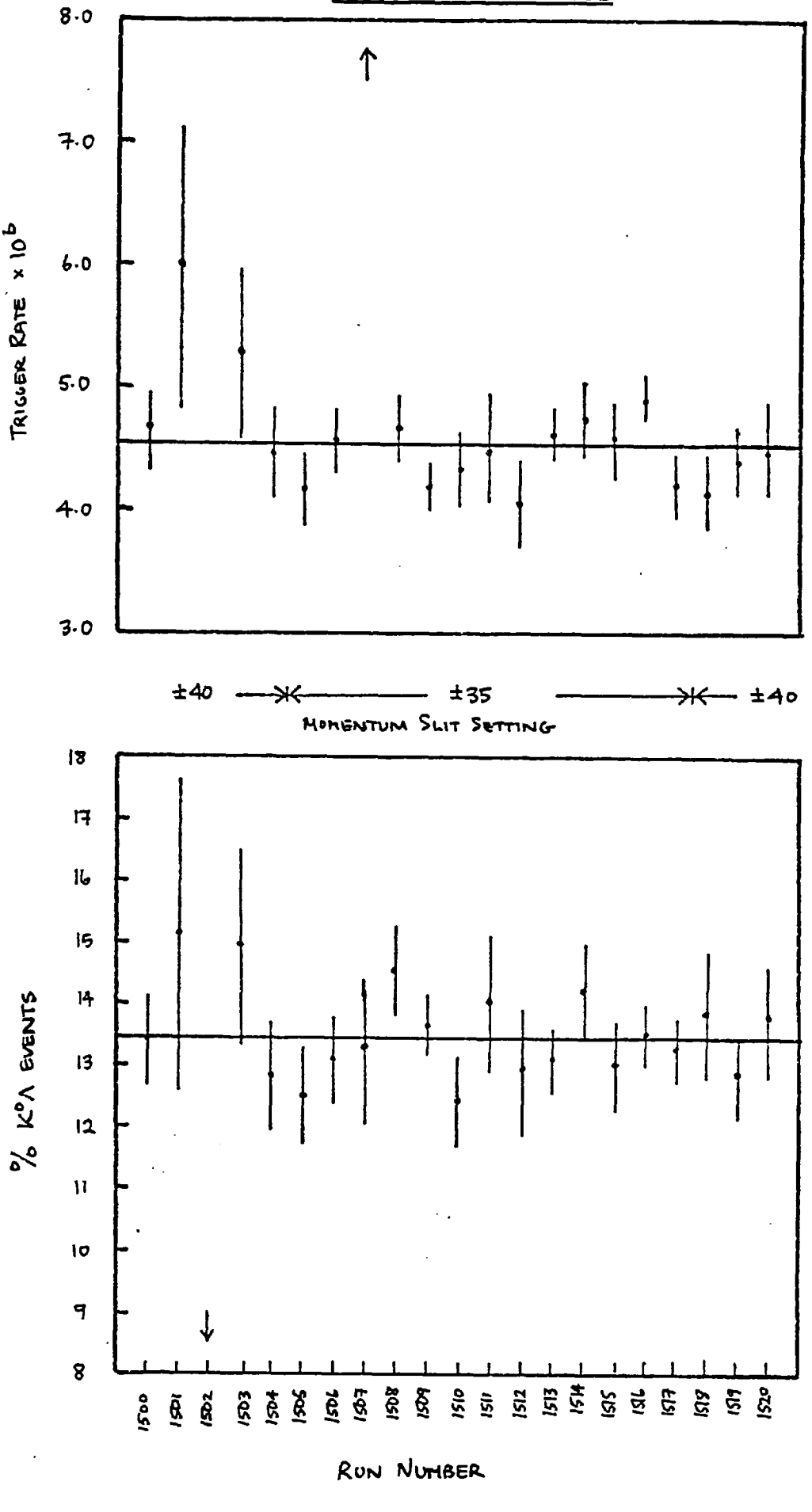


Figure 5.5

Values of R2

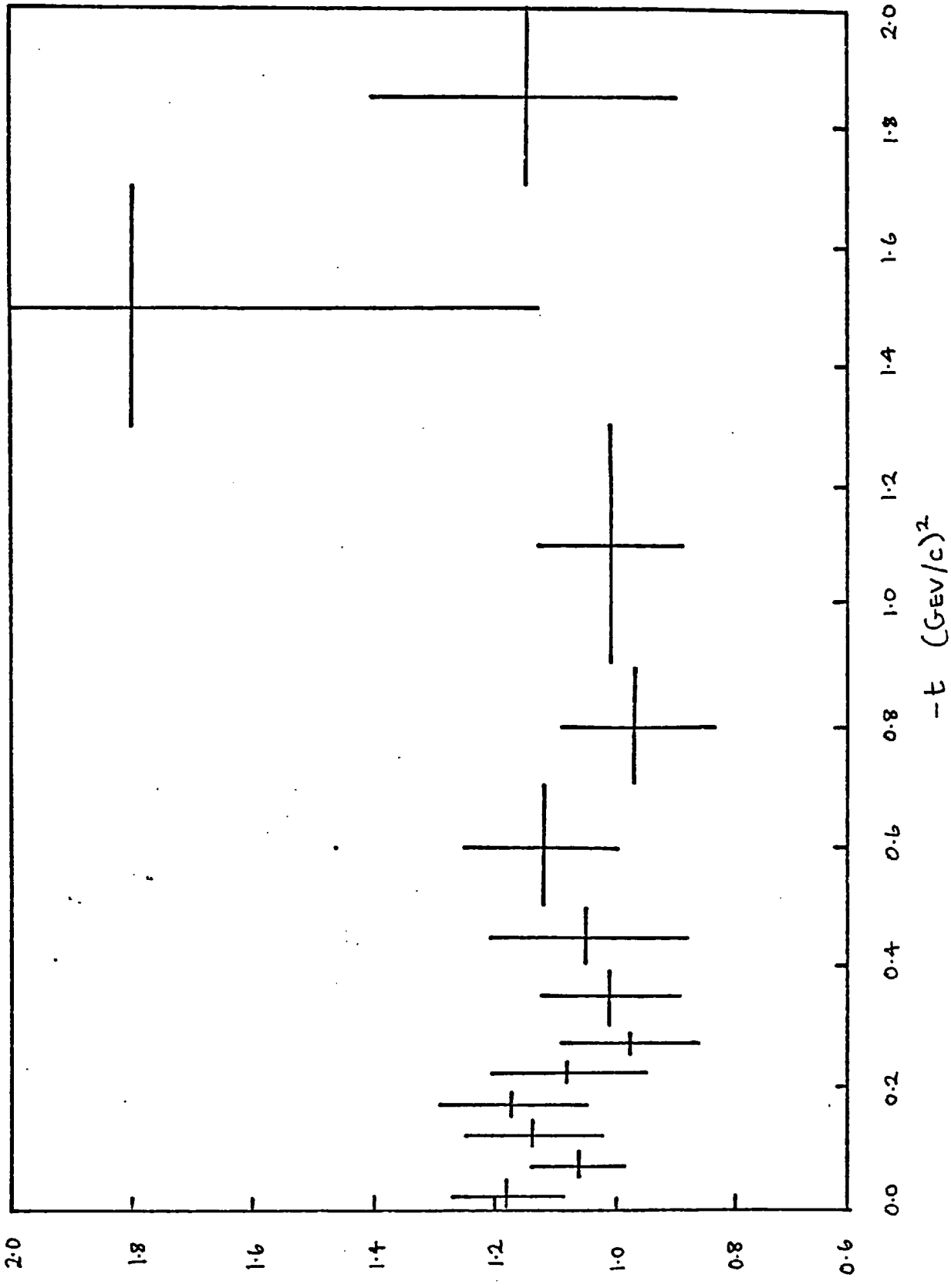


Figure 5.6

Polarization as a Function of Missing Mass Squared

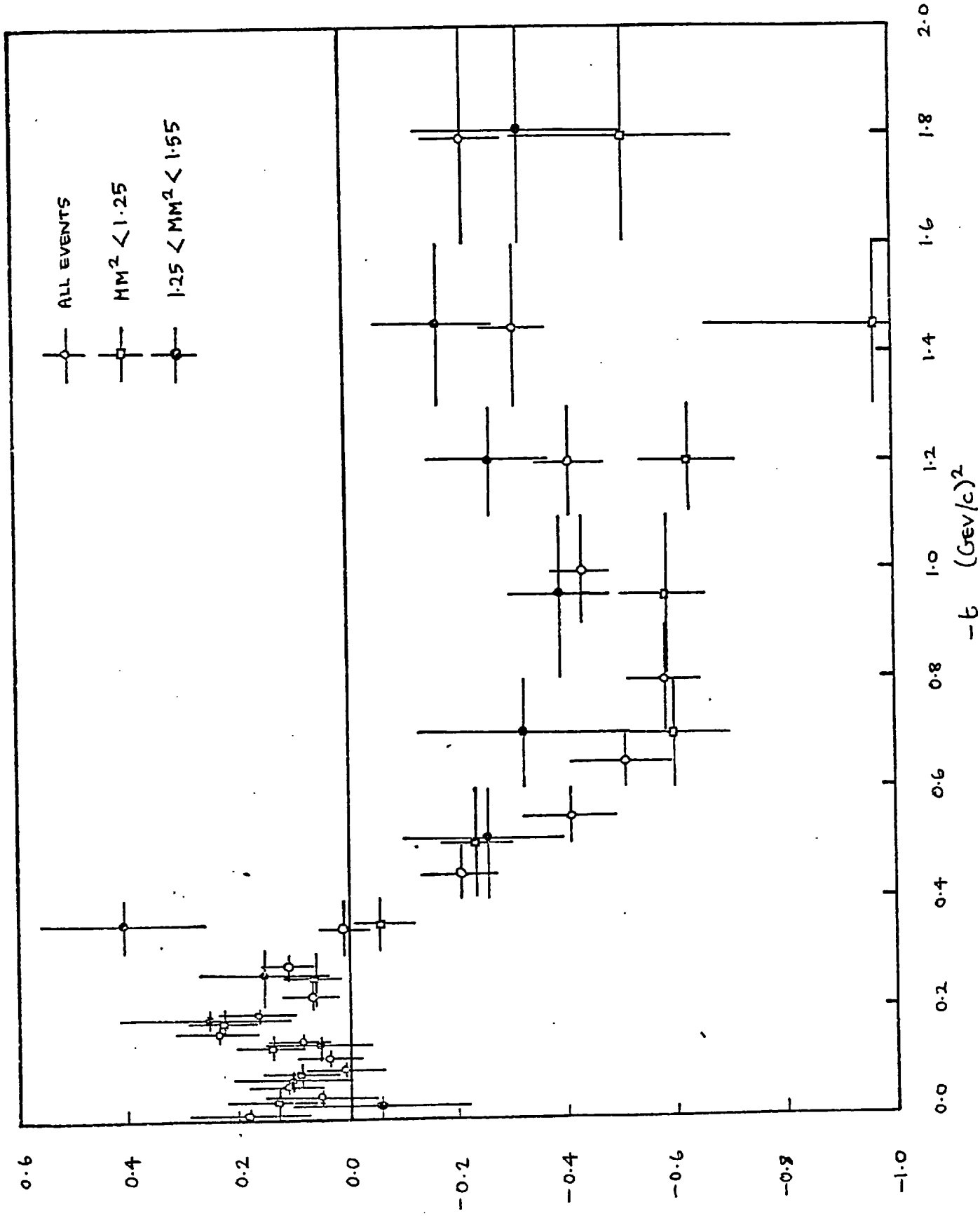


Figure 5.7

Consistency Checks on R1

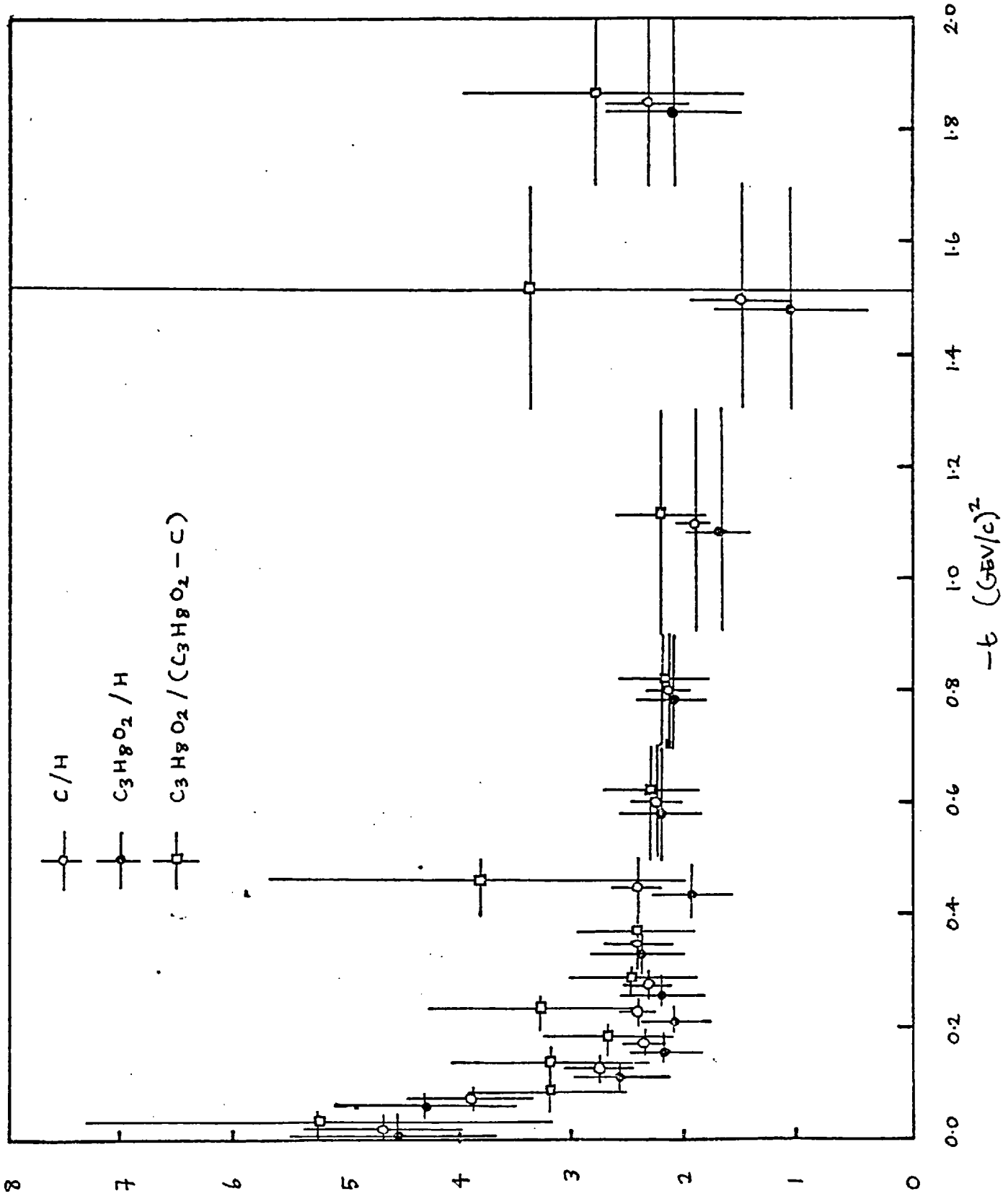


Figure 5.8

The Structure of F_c

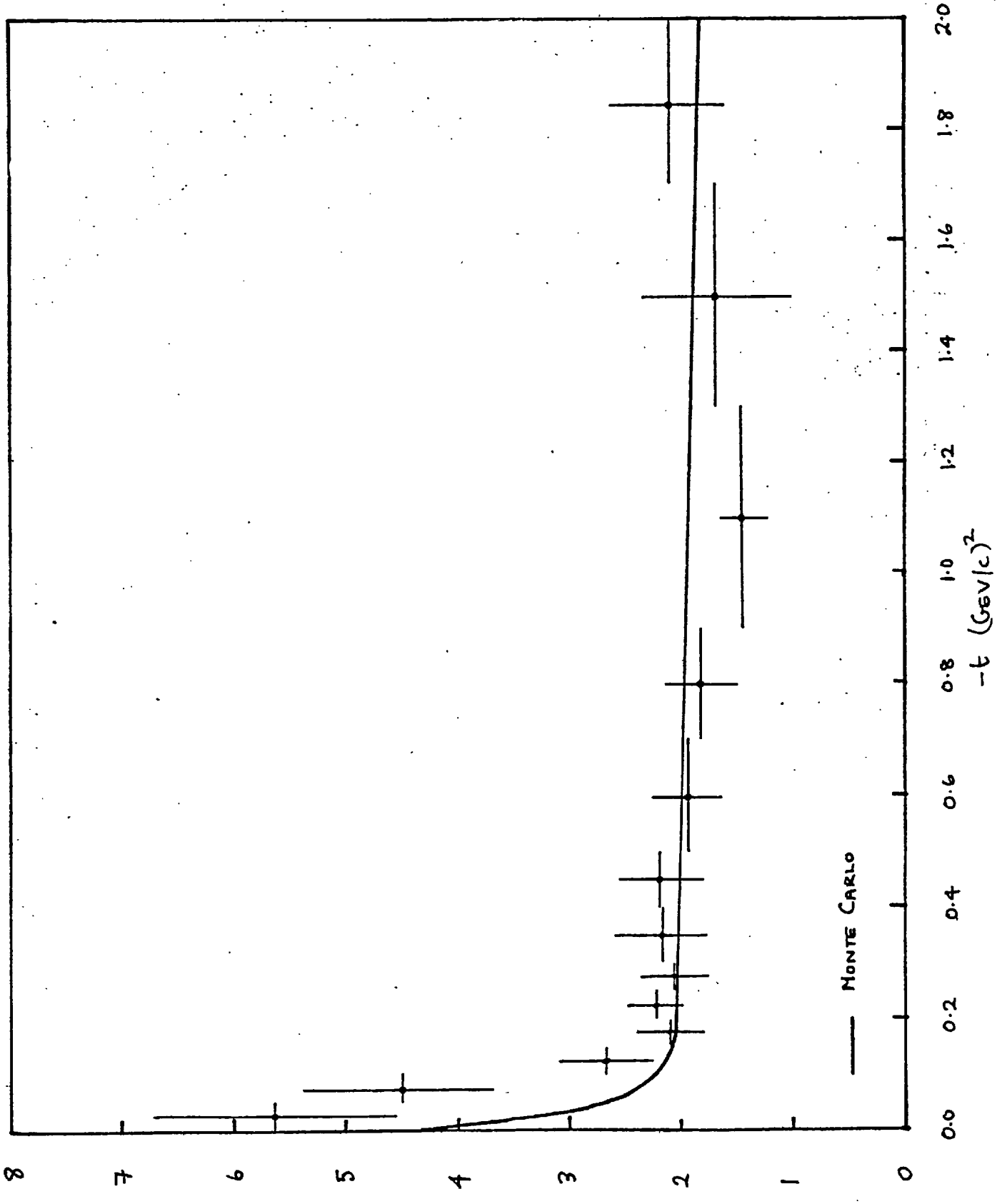


Figure 5.9

The Acceptance of the Apparatus

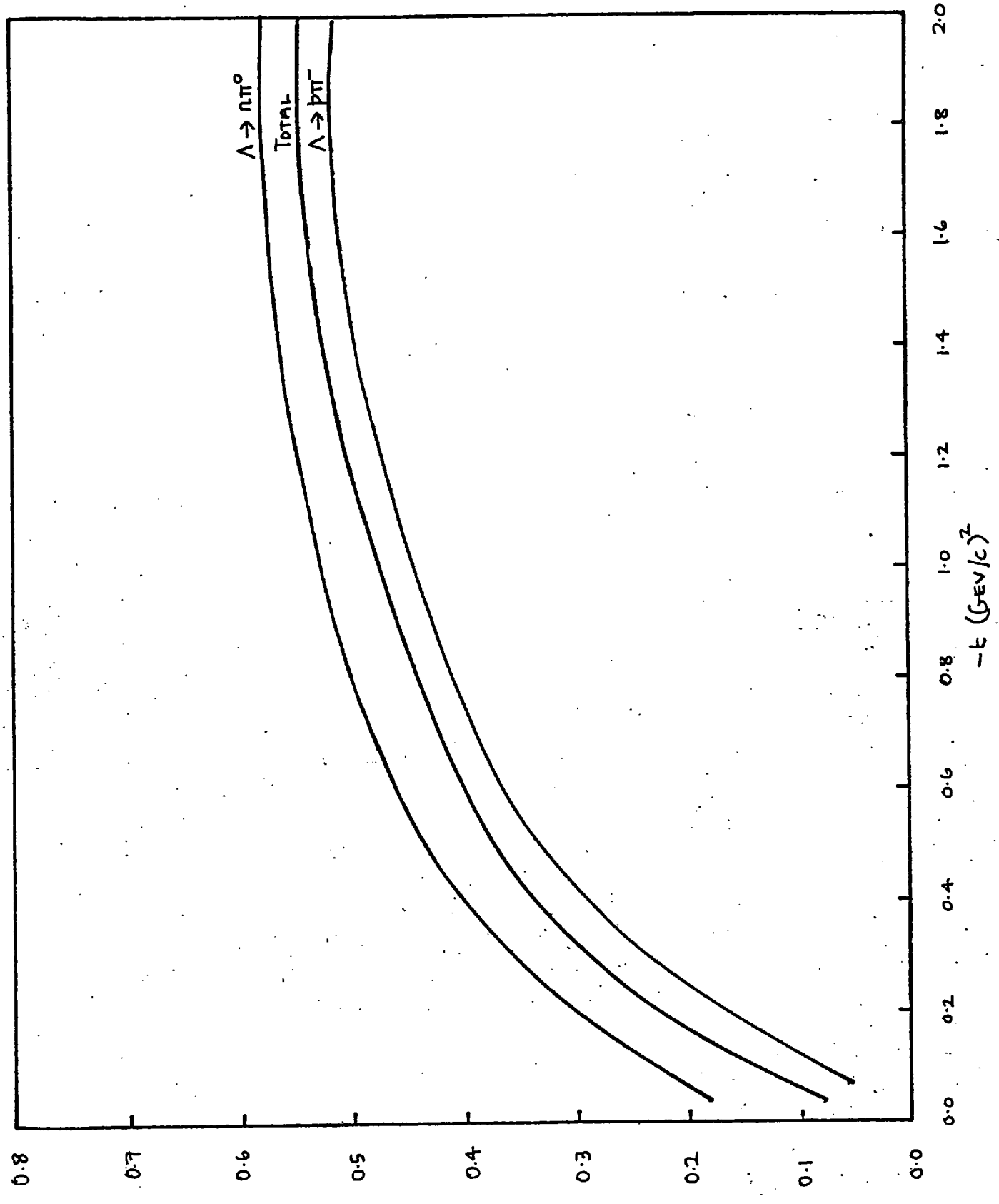


Figure 5.10

The Polarization Parameter

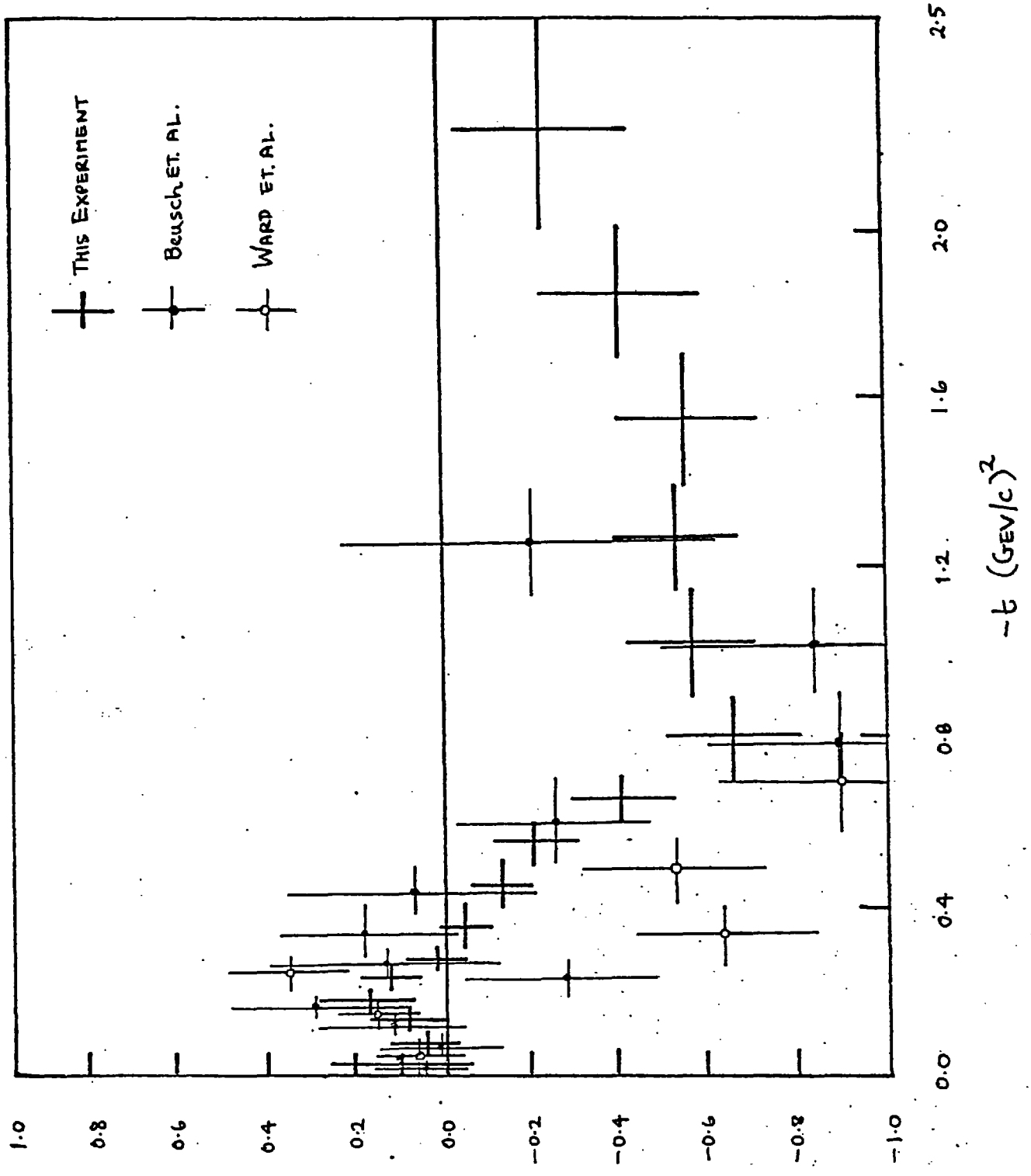


Figure 5.11

Polarization for All t

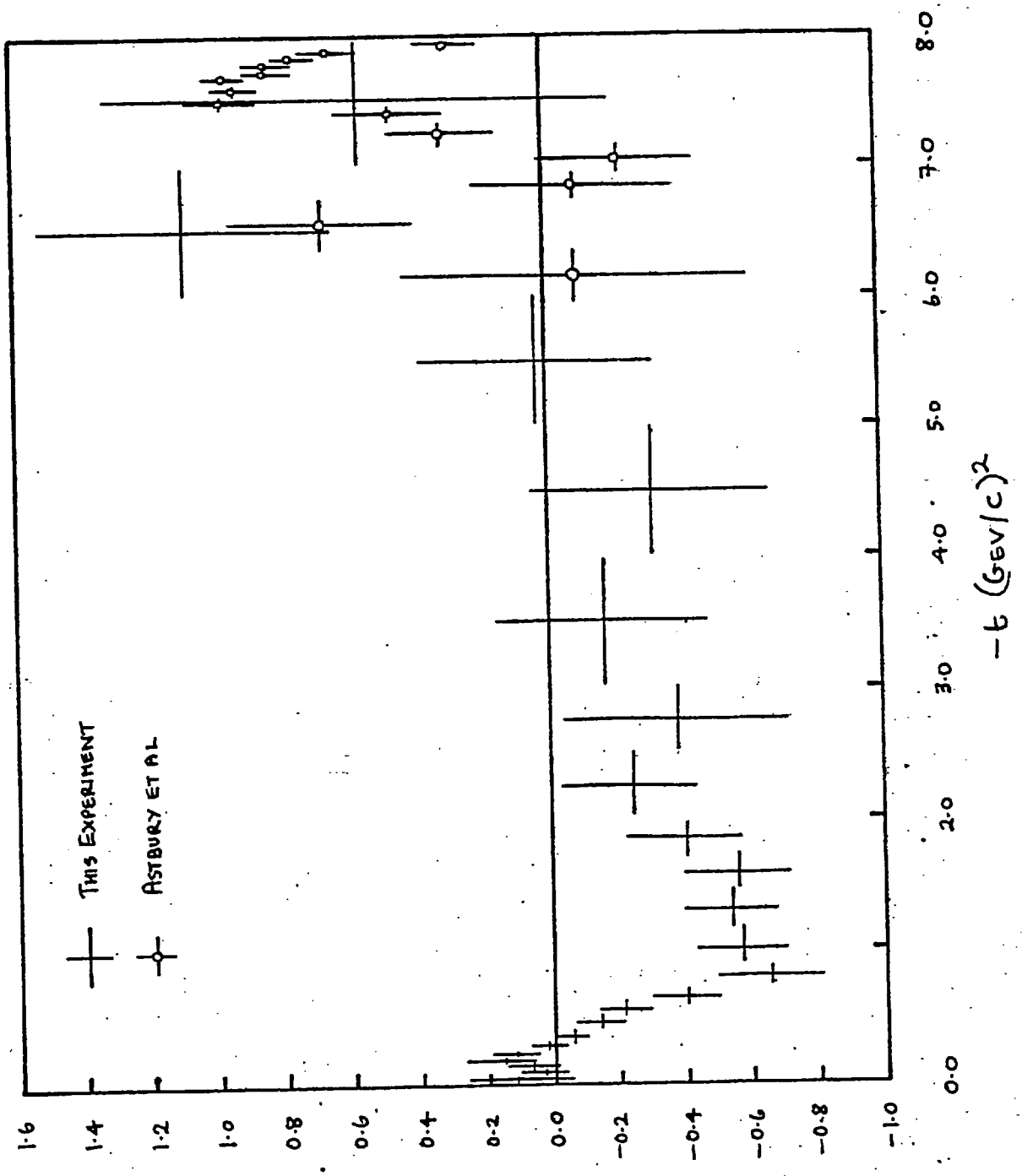
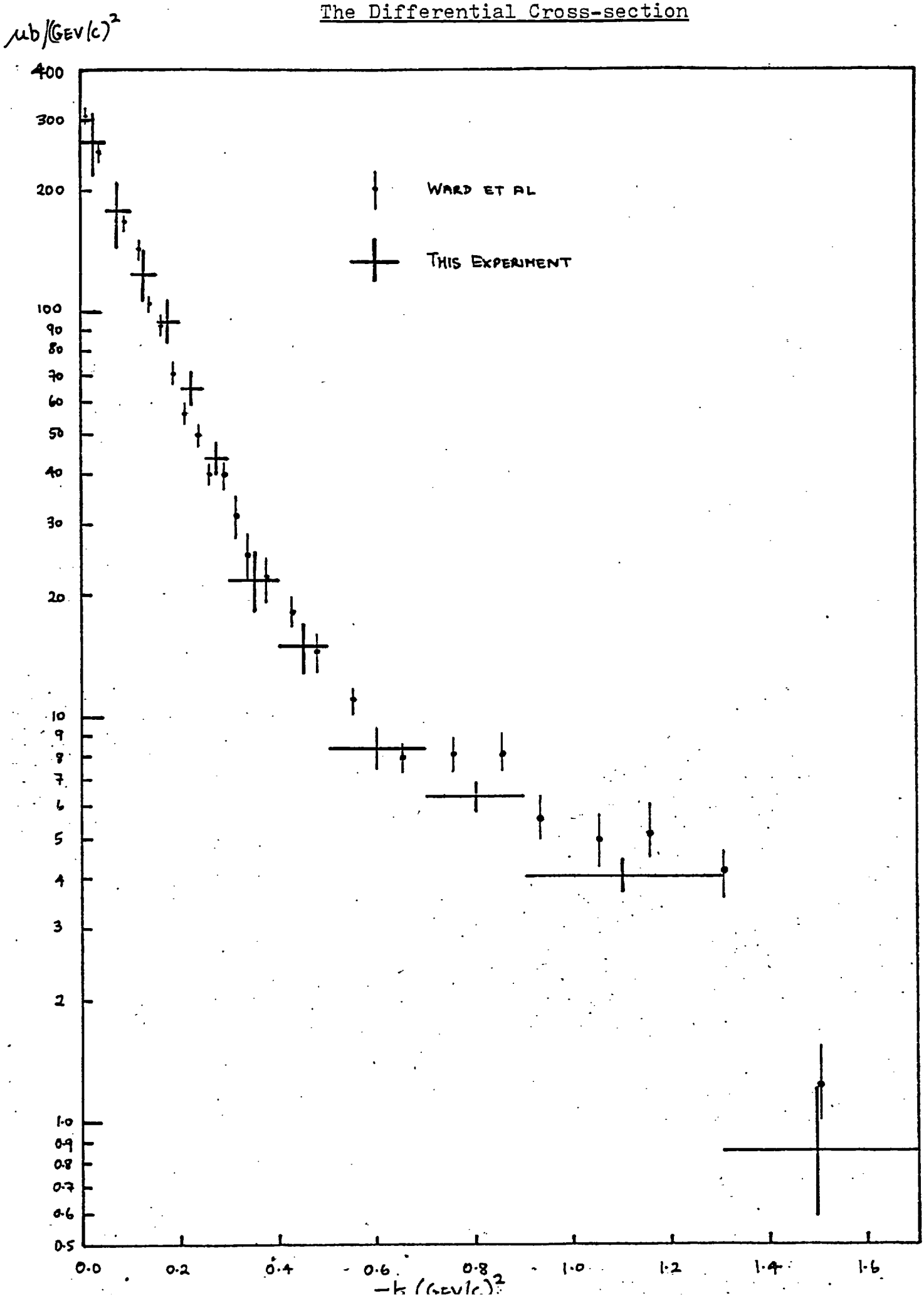


Figure 5.12

The Differential Cross-section



CHAPTER 6

Theoretical Discussion

6.1 Introduction

Hypercharge exchange reactions such as $\pi^- p \rightarrow K^o \Lambda$ above $\sim$ 2 GeV/c are dominated by the exchange of the $K^*(890)$ ($J^P = 1^-$) and the $K^{**}(1420)$ ($J^P = 2^+$), the exchange of the K meson being excluded by spin parity.(Ref. 23). One of the important consequences of duality is exchange degeneracy between Regge pole exchanges. Exchange degeneracy (EXD) relates the trajectories and couplings of Regge poles of opposite signature.

The $K^*(890)$ and $K^{**}(1420)$ mesons lie on a common trajectory as do the ρ and the f mesons which implies that EXD is a good symmetry in the time like region. However strong K^*-K^{**} EXD predicts zero polarization (Ref. 24) for $\pi^- p \rightarrow K^o \Lambda$ in severe disagreement with the data. Thus in the space like region EXD is definitely broken. In order to retain the concept of EXD one therefore needs additional contributions to the dynamics in addition to pure Regge pole exchange. Regge cuts and absorptive corrections can destroy the underlying symmetry and hence help to explain the data.

In this chapter the predictions for the polarization in $\pi^- p \rightarrow K^o \Lambda$ for several models are compared with our data.

Some predictions for the spin rotation parameters A and R are also given.

6.2 Comparison of the Data with Various Models

6.2.1 Basic Regge Pole Theory

The first order amplitude for an s channel scattering process ($A + B \rightarrow A + B$) involving the exchange of a single meson of spin J and mass M_J in the t channel ($\bar{A} + A \rightarrow \bar{B} + B$) is given by

$$F(s,t) = \frac{g_J^2 \,[2J+1]\, (-S/S_o)^J}{M_J^2 - t} \qquad \text{as } S \rightarrow \infty \text{ (Ref. 25)}$$

g_J^2 is the product of the coupling constants and S_o is an energy scale factor. Now if the exchanged particle is a member of a Regge trajectory with an infinite series of particle recurrences J = 1, 3, 5 ... or J = 2, 4, 6 ... then the amplitude due to summing over all these mesons on the trajectory is given by

$$F(s,t) = \sum_{J=1}^{\infty} \frac{g_J^2(2J+1)}{M_J^2 - t} \left[\frac{(-1)^J + \tau}{2}\right]\left(\frac{S}{S_o}\right)^J$$

where τ is the signature of the trajectory given by $\tau = (-1)^J$. If the coupling constants are assumed equal and M_J^2 increases linearly with J as is observed for certain sets of mesons then the resultant s channel amplitude can be written as

$$f(s,t) \sim \sum_r \frac{[2\alpha_r(t) + 1]}{\sin \pi \alpha_r(t)} \gamma_r(t) \left[1 + \tau_r e^{-i\pi\alpha_r(t)}\right] \left(\frac{s}{s_o}\right)^{\alpha_r(t)}$$

where $\alpha(t) = \alpha_o + \alpha_1 t$ is the trajectory. γ_r is the residue function associated with the pole.

The trajectory $\alpha(t)$ determined for $t > 0$ from assignments of resonances as Regge recurrences is a smooth continuation of the trajectory for $t \lesssim 0$ that describes scattering due to Regge pole exchange.

6.2.2 Duality and Exchange Degeneracy

Duality (Ref. 26) is the idea that resonance formation and Regge pole exchange, which appear to dominate low energy and high energy scattering respectively, may be simply and directly related. If f is the scattering amplitude then

Im f(resonance + background) $\simeq$ Im f(Regge poles + Pomeron)

Im f(resonance) $\simeq$ Im f(Regge poles)

Im f(background) $\simeq$ Im f(Pomeron).

The Pomeron has the quantum numbers of the vacuum ($J^{PC} = 0^{++}$, $I_3 = B = S = 0$).

If one considers an inelastic reaction where the t channel allows Regge pole exchange but the s channel is exotic i.e. cannot be described by three simple quarks or a quark-antiquark pair, then in general there will be no s channel resonances. Thus Im f(Regge poles) = 0. Since all the exchanged poles cannot decouple from the interaction this can only be satisfied by cancellation of terms in the amplitude. This implies exchange degeneracy of the

trajectories and residues.

6.2.3 Simple Regge Pole Models

The helicity non-flip and flip amplitudes from a single Regge pole have the same phase and energy dependence. Thus any non-zero polarization must come from the interference of two poles. Since only the ρ trajectory is allowed in the reaction $\pi^- p \to \pi^0 n$, one expects zero polarization. Data at 3.5 and 5 GeV/c (Ref. 27) suggest that the polarization is zero for $0.6 < -t < 1.8$ $(GeV/c)^2$ but positive for $-t < 0.35$ $(GeV/c)^2$. Thus pure Regge pole exchange models are unable to describe the data.

In general simple Regge pole models predict the differential cross-sections quite well, however they are unable to describe polarizations which depend on the interference between helicity flip and non-flip amplitudes, hence providing a much more sensitive test. Helicity flip amplitudes appear to have mainly the simple Regge pole form whereas helicity non-flip amplitudes do not (Ref. 28).

In $\pi^- p \to K^0 \Lambda$ where two Regge poles are exchanged then non-zero polarization is allowed as long as there is not strong exchange degeneracy. Predictions from two simple Regge models (Refs. 29 and 30) are shown in fig. 6.1. These models have different prescriptions for the residues but essentially the same trajectory functions. There is large disagreement with the data. It can be seen that even without exchange degeneracy the exchange of simple Regge

poles alone is not adequate to describe the data. Hence modifications are required which are described below.

6.2.4 Regge Cuts

A t-channel Regge pole can be considered as a pole of the partial wave amplitude $a_j(t)$ in the complex J-plane. It is possible to have other singularities as well as poles such as branch points with associated cuts. Cuts can be thought of as multi-exchange effects consisting of a continuum of trajectories lying below α_c and approximated by some mean trajectory α_{eff} (see fig. 6.2).

The cut trajectory α_c from the exchange of two trajectories $\alpha_1 = \alpha_{10} + \alpha_1' t$ and $\alpha_2 = \alpha_{20} + \alpha_2' t$ is given by

$$\alpha_c(t) = \alpha_{10} + \alpha_{20} - 1 + \left(\frac{\alpha_1' \alpha_2'}{\alpha_1' + \alpha_2'}\right) t \quad \text{(Ref. 31)}$$

The intercept is generally lower than either pole unless one of them is the Pomeron. The most important Regge cuts are those involving Regge pole exchange and Pomeron exchange. These are shown in fig. 6.3 and can be considered as elastic scattering in the initial or final state as well as Regge pole exchange. This is also known as Absorption, which is discussed later.

6.2.5 The Model of Navelet and Stevens (Ref. 32)

A Regge pole plus effective-cut parameterization was fitted to all experimental data available up to 1975 for $0^-\frac{1}{2}^+ \to 0^-\frac{1}{2}^+$ hypercharge exchange reactions.

The pole amplitudes were as follows with K^* and K^{**} amplitudes being treated separately

$$F_{++} = K\gamma_{++}\,(\tau + e^{-i\pi\alpha(t)})\; s^{\alpha(t)}\; e^{a_{++}t}$$

$$F_{+-} = K\sqrt{-t'}\,\gamma_{+-}\,(\tau + e^{-i\pi\alpha(t)})\; s^{\alpha(t)}\; e^{a_{+-}t}$$

K is a kinematic factor and $\sqrt{-t'} = \sqrt{-(t-t_{min})}$. The a's and the residues are considered different for Λ and Σ channels.

The effective cut amplitudes read

$$F_{++} = K\gamma_{++}\gamma_c \begin{Bmatrix} i \\ -1 \end{Bmatrix} (e^{-i\pi/2}s)^{\alpha_c(t)}\; e^{a_c t}$$

where (i) is for vector exchange, (K^*) and (-1) for tensor exchange (K^{**}). γ_c is the strength of the cut trajectory relative to the pole. The relative sign convention is that used by Martin et al (Ref. 33) i.e.

$$F_{++} = -K^* - K^{**}$$

Both vector and tensor pole trajectories are found to be close to the trajectory passing through the particle masses $(0.35 + 0.82t)$ whereas the effective cut trajectory is flatter and lower.

The prediction for the polarization parameter in $\pi^- p \rightarrow K^0 \Lambda$ is shown in fig. 6.4 and is in quite good agreement with our data points. Only a slight adjustment of the parameters is required to produce a good fit to the data. This is perhaps not too surprising since our data agrees with previous data which this model was fitted to.

However new data (Ref. 34) on the line reversed reactions $\pi^+ p \rightarrow K^+ \Sigma^+$ and $K^- p \rightarrow \pi^- \Sigma^+$ find that $P_o(\pi^+ p \rightarrow K^+ \Sigma^+) + P_o(K^- p \rightarrow \pi^- \Sigma^+) = 0$ for $0 < -t < 1.0$ $(GeV/c)^2$ whereas this model predicts a fall to $P_o \sim -0.6$ at $-t \sim 0.3$ $(GeV/c)^2$ rising to zero at $-t \sim 1.0$ $(GeV/c)^2$.

Fitting our polarization data and the cross-section data of Ward et al to Navelet and Stevens model we are able to deduce the structure of the helicity amplitudes which are shown in fig. 6.5. The relative strength of the cut term γ_c is of order 1 so that the helicity non-flip amplitudes have to be extensively modified from the pure Regge form in order to fit the data.

6.2.6 The Model of Girardi (Ref. 35)

A Regge-Cut model applied to elastic and charge exchange reactions has been used to predict the behaviour of hypercharge exchange reactions.

The starting point of the model is the expansion of the amplitude in terms of Regge poles and their iterations.

$$M = R + (P*R) + (R*P) + (R*R) + (P*R*R) + \ldots$$

where P*R means the convolution between Pomeron and Regge exchange amplitudes and is represented by a diagram such as fig. 6.3.

The Regge pole contribution has the standard form and the Pomeron pole amplitude for a process AB → AB is given by

$$i\,\sigma_{\infty}(AB)\,\nu\,\exp\left[t(a(AB) + \alpha'_p \ln(\nu/\nu_0))\right] \cdot \exp(-\tfrac{1}{2}i\pi\alpha'_p t)$$

where $\sigma_{\infty}(AB)$ is the asymptotic total cross-section for the channel AB, $\nu = \frac{1}{2}(s-u)$ and ν_0 is fixed at 1 $(GeV/c)^2$. The Pomeron trajectory is

$$\alpha_p(t) = \alpha_p(o) + \alpha'_p t = 1.0 + 0.2t$$

The model uses fits to data in charge exchange reactions and then uses SU(3) symmetry relations to predict behaviour in hypercharge exchange reactions.

The predictions of this model for $P_o(\pi^- p \to K^o \Lambda)$ are shown in fig. 6.4 and are not in good agreement with the values measured in this experiment.

6.2.7 The Model of Irving, Martin and Michael (Ref. 36)

This model employs an exchange degenerate $K^* - K^{**}$ pole trajectory parameterized in the normal way and a Regge cut. The Regge cut is generated by absorbing the pole with a Pomeron with trajectory $\alpha_p = 1 + 0.5t$.

The prediction for the polarization in $\pi^- p \to K^0 \Lambda$ is shown in fig. 6.4 and there is reasonable agreement with the data.

6.2.8 Absorption

Absorption is an initial or final state interaction looked at from a purely s-channel point of view, as opposed to Regge cuts which are t-channel exchanges.

The main feature of absorptive models is that scattering will be dominated by the most peripheral partial wave. If k is the centre of mass momentum and R($\sim$ 1 fermi) is the radius of interaction, then the scattering can be described by $f \sim J_{\Delta\lambda}(R.\sqrt{-t})$ where $\Delta\lambda$ is the net s-channel change in helicity and $J_{\Delta\lambda}$ is the Bessel function of order $\Delta\lambda$.

Harari (Ref. 37) has proposed a Dual Absorption Model (DAM) in which the imaginary part of any amplitude is made up of two components
(a) contributions from all s-channel resonances, equivalent to all non-Pomeron t-channel exchange, and
(b) non-resonant s-channel background corresponding to t-channel Pomeron exchange.
Contribution (a) has the form of the $J_{\Delta\lambda}$ Bessel function as shown above. The background term (b) is assumed to conserve s-channel helicity. The real parts are deduced from the imaginary parts either by dispersion relations or from theorems relating high energy behaviour to the phase of the amplitudes.

6.2.9 The Model of Loos and Matthews (Ref. 38)

This is a Dual Absorption Model in which the imaginary parts of the s-channel helicity non-flip and helicity flip amplitudes are assumed to have the "J_0" and "J_1" structures respectively, as specified by the dual absorption model of Harari.

The authors apply their model to charge and hypercharge exchange data to determine empirically the real part of the s-channel non-flip amplitude which the model does not predict.

The predictions for $P_0(\pi^- p \to K^0 \Lambda)$ are shown in fig. 6.4 and are seen to be in fair agreement with the data.

6.2.10 Finite Energy Sum Rules

Finite energy sum rules (Ref. 39) (FESR) determine high energy Regge parameters from integrals over low energy scattering data.

The relationships are of the form:

$$\int(\text{s-channel physics}) + \int(\text{u-channel physics}) + \int(\text{Regge poles}) = 0$$

Field and Jackson (Ref. 40) using FESR for the reactions $K^- n \to \pi^- \Lambda$ and $\pi^+ n \to K^+ \Lambda$ determine the effective pole parameters of the K^* and K^{**} Regge trajectories from

a knowledge of the low energy resonances and their couplings. Good fits are achieved for $K^-n \to \pi^-\Lambda$ over a wide range of energies whereas they are unable to fit $\pi^+n \to K^+\Lambda$ at intermediate energies. This is possibly explained by the fact that the contributions to $K^-n \to \pi^-\Lambda$ mainly come from peripheral resonances whose angular momenta increase with their masses, whereas the contributions to $\pi^+n \to K^+\Lambda$ are mainly from small spin non-peripheral resonances.

The predicted polarization in $\pi^+n \to K^+\Lambda$ at 3.9 GeV/c is also shown in fig. 6.4.

6.3 Predictions for A and R Parameters

In section 6.2 several models have been shown to predict $P_o(\pi^-p \to K^o\Lambda)$ with varying degrees of accuracy. Most of these models have some degrees of freedom which allow them to be fitted to the data. Thus a measurement of the polarization alone is not enough to decide which model or models are best at describing the data and a more sensitive test still is required. Since most of these models are parameterized in terms of the helicity amplitudes they are able to provide direct predictions for the parameters A and R as described in Chapter 1.

In fig. 6.6 the predictions for A and R from the models discussed so far are shown for $\pi^-p \to K^o\Lambda$ in the region of 5 GeV/c. Also plotted are the predictions from

a direct amplitude analysis carried out by Ward et al (Ref. 41) which is described below.

6.3.1 Amplitude Analysis of Ward et al

Using data on $d\sigma/dt$ and polarizations in $\pi^- p \to K^0 \Lambda$ and $\pi^- p \to K^0 \Sigma^0$ at 5 GeV/c and assuming SU(3) octet dominance of baryon couplings in s-channel helicity amplitudes, the amplitudes are determined up to an overall phase.

As shown in Chapter 1 the differential cross-sections and polarized cross-sections can be expressed as;

$$\frac{d\sigma_\Lambda}{dt} = (2\alpha_+ + 1)^2 |f_+|^2 + (2\alpha_- + 1)^2 |f_-|^2$$

$$P_\Lambda \frac{d\sigma_\Lambda}{dt} = 2(2\alpha_+ + 1)(2\alpha_- + 1) |f_+|^2 |f_-|^2 \sin\phi_{+-}$$

where $$\frac{F_{++}^{\Lambda}}{2\alpha_+ + 1} = \frac{F_{++}^{\Sigma}}{\sqrt{3}(2\alpha_+ - 1)} \equiv f_+$$

with similar expressions for $\pi^- p \to K^0 \Sigma^0$. ϕ_{+-} is the phase of f_- relative to f_+.

Since the helicity flip amplitude vanishes at 0° one can calculate α_+ from

$$R_z \equiv \frac{d\sigma/dt^{\Sigma}(0^\circ)}{d\sigma/dt^{\Lambda}(0^\circ)} = \frac{3(2\alpha_+ - 1)^2}{(2\alpha_+ + 1)^2}$$

which is constant with energy between 3 and 6 GeV/c (Ref. 42) with an average value of 0.708 ± 0.014. In addition α_- can be calculated from

$$R_p \equiv \frac{P_\Sigma d\sigma^\Sigma/dt}{P_\Lambda d\sigma^\Lambda/dt} = \frac{3(2\alpha_+ - 1)(2\alpha_- - 1)}{(2\alpha_+ + 1)(2\alpha_- + 1)}$$

which at 5 GeV/c is found to be independent of t with a value of -0.304 ± 0.067. From these results they obtain $\alpha_+ = 1.445 \pm 0.007$ and $\alpha_- = 0.327 \pm 0.031$. Using the values for α_+ and α_- they solve for $|f_+|$, $|f_-|$ and $\sin\phi_{+-}$ enabling the parameters A and R to be calculated. The predictions are shown in fig. 6.6.

6.4 Conclusions

Since the polarization in $\pi^- p \to K\Lambda$ is non-zero, then simple Regge pole exchange and strong exchange degeneracy of the K^*-K^{**} trajectories is ruled out. They may however be weakly degenerate with equality of the trajectories but not the residues. In fact since the s-channel for $\pi N \to K\Lambda$ is non-exotic strong exchange degeneracy is not required by duality.

The overall picture seems to be that pure Regge exchange can only explain helicity flip amplitudes and that the imaginary parts of the helicity non-flip amplitudes need to be extensively modified by absorption or Regge cuts in order to describe the data.

Although several models correctly predict the polarization for $\pi^- p \rightarrow K^0 \Lambda$ their predictions for the spin rotation parameters A and R differ wildly. Hence measurement of these parameters which will eventually be extracted from our data, will be of the utmost importance in choosing between these models.

Figure 6.1

Predictions for the Polarization from Simple Regge Pole Models

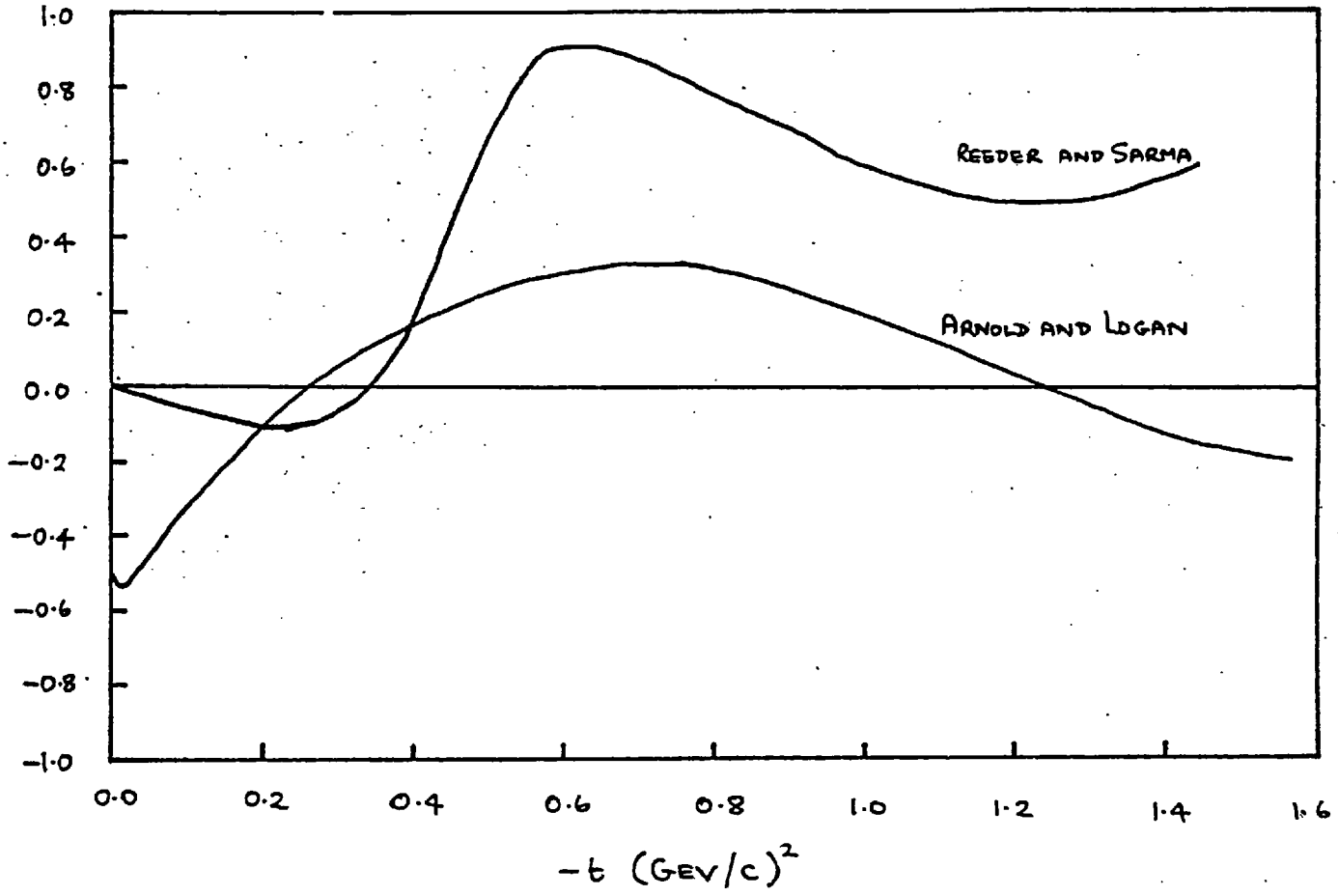


Figure 6.2

Regge Cut Trajectories

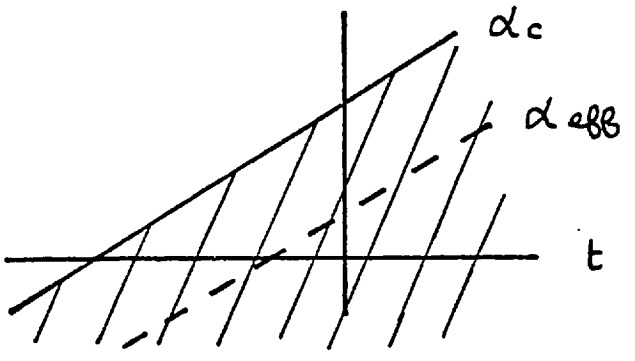


Figure 6.3

Regge-Pomeron Cuts

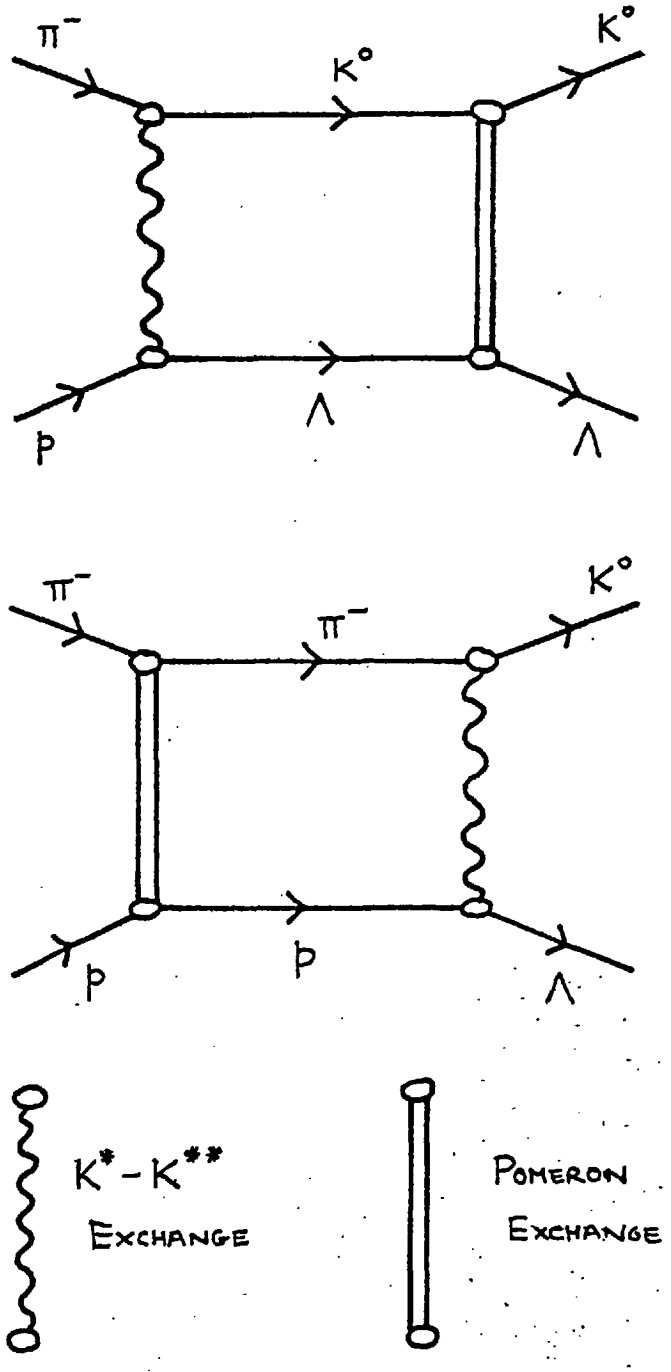


Figure 6.4

Comparison of the Polarization with the Predictions of Various Models

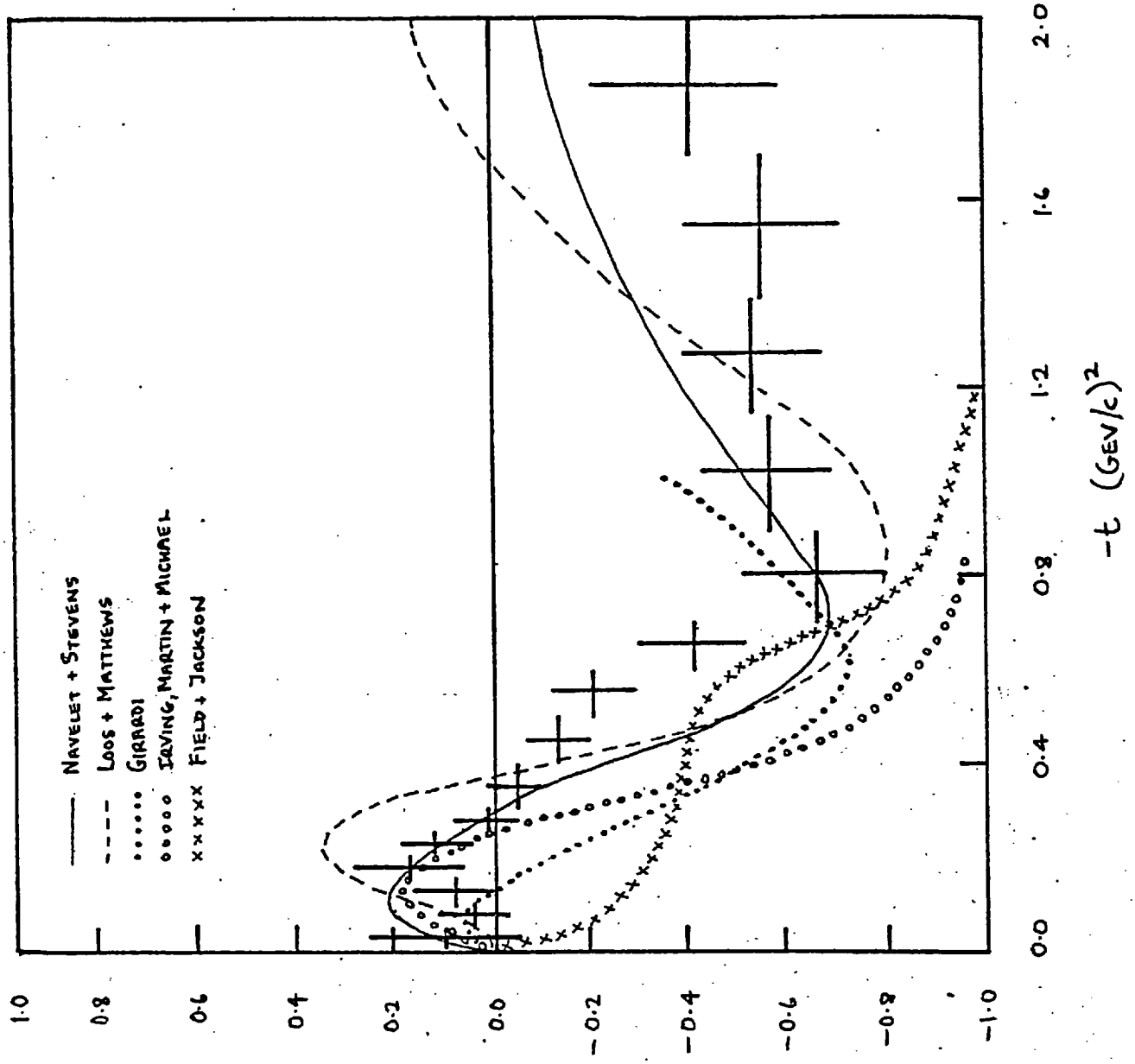


Figure 6.5

Helicity Amplitudes from the Model of Navelet and Stevens

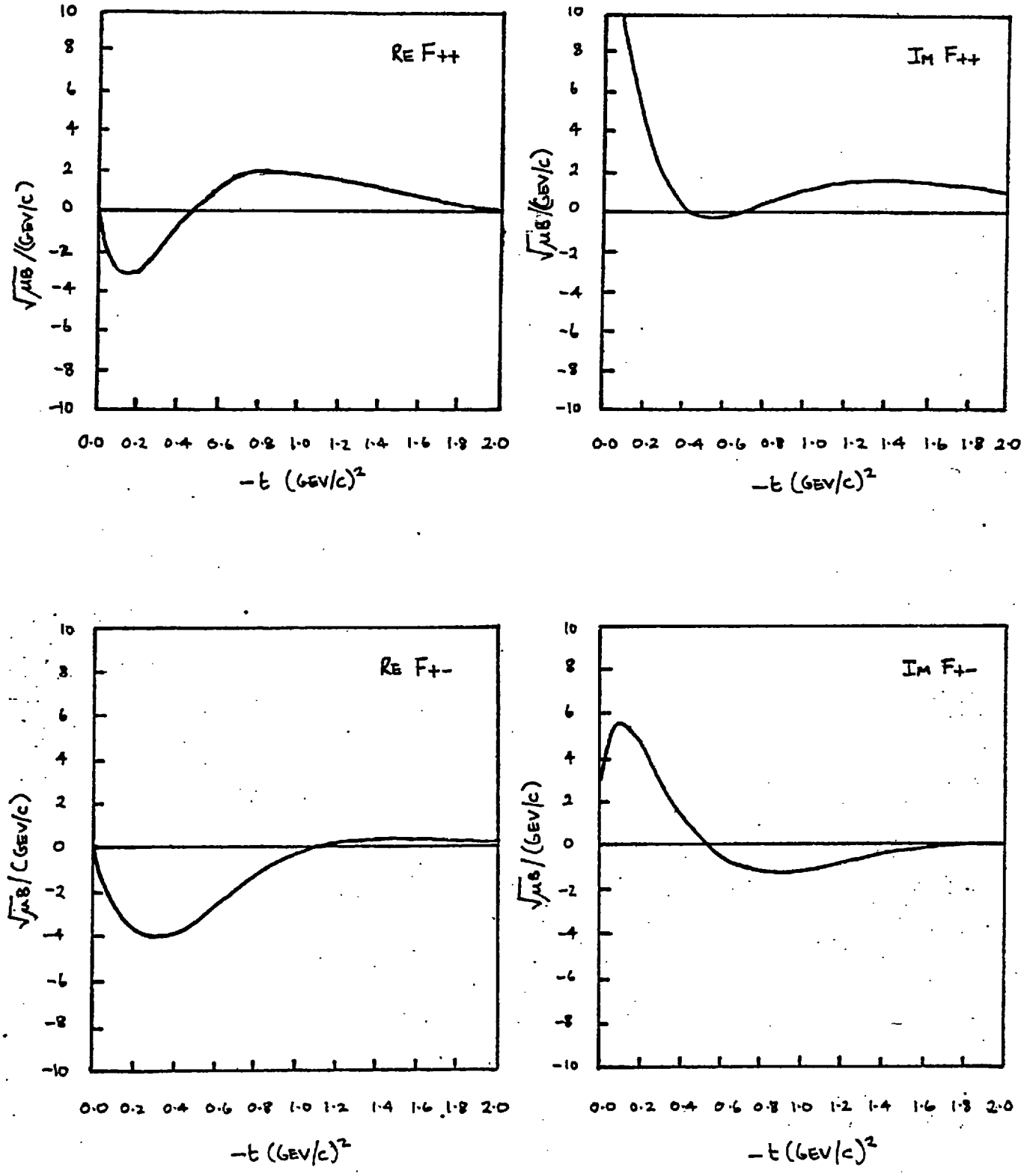
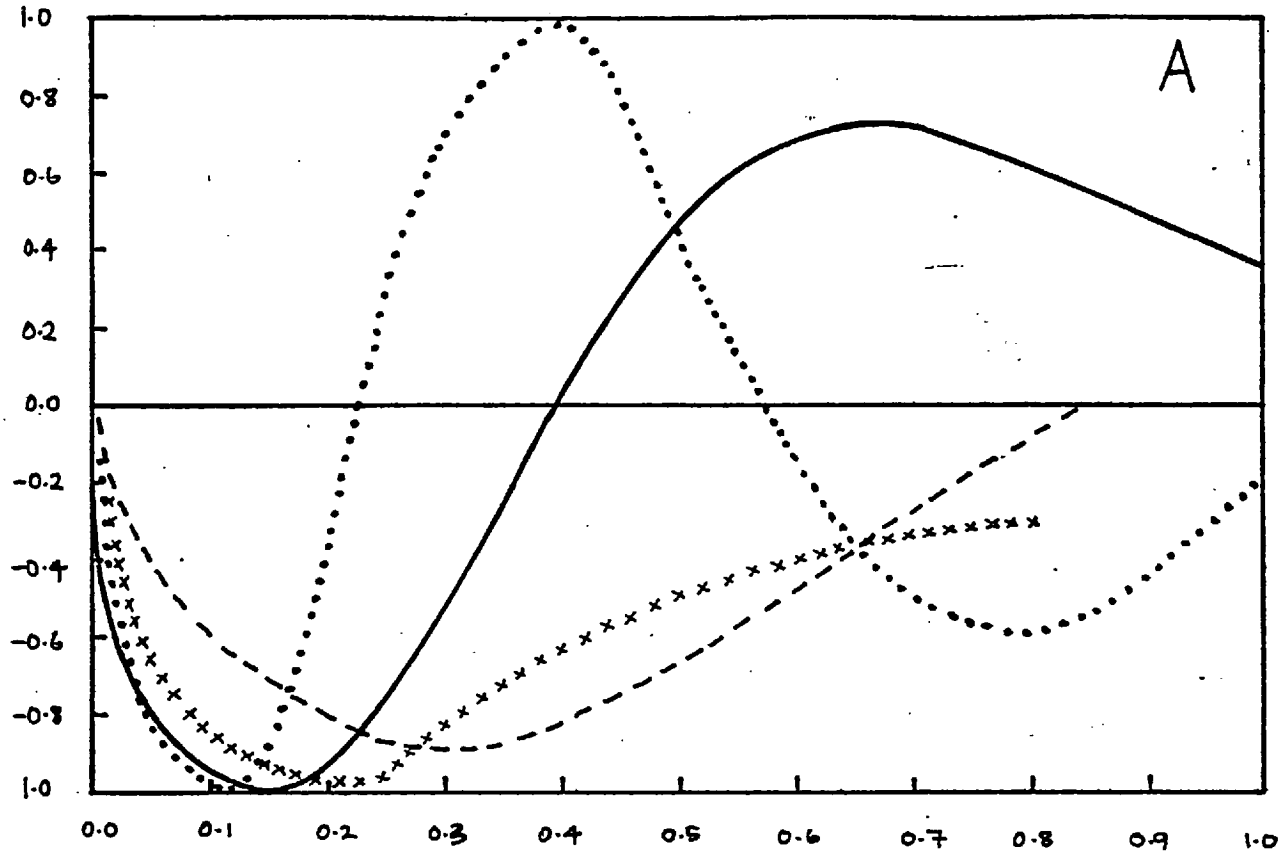
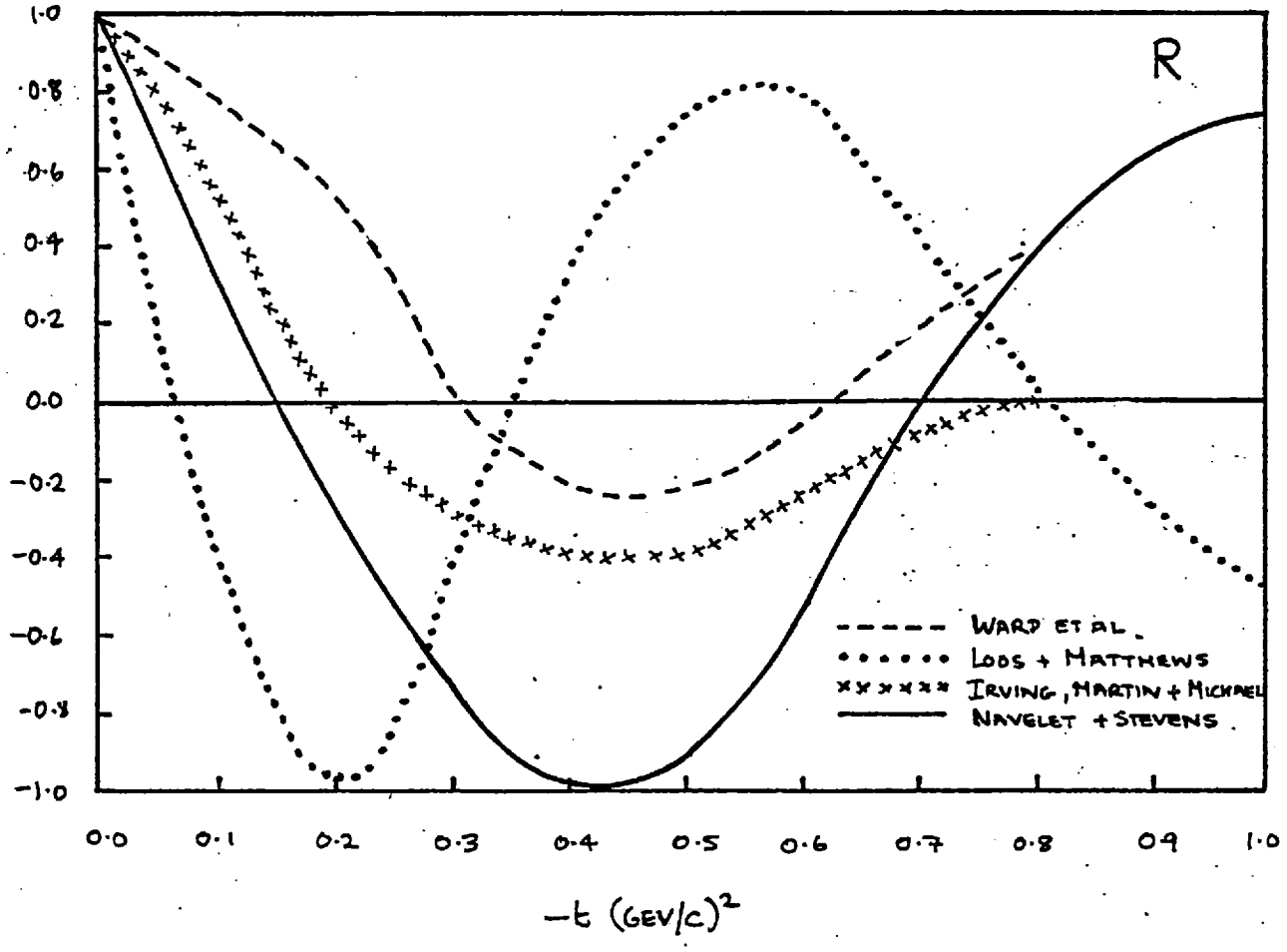


Figure 6.6

Predictions for A and R Parameters





CHAPTER 7

Test of a π^0 Detector

7.1 Introduction

In Chapter 1 it was shown that more stringent tests of exchange models could be made if data on SU(3) related and line reversed reactions were compared. It was proposed (Ref. 43) that the study of the reaction $\pi^- p \rightarrow K^0 \Lambda$ at 5 GeV/c be followed by a study of the line reversed reaction $K^- p \rightarrow \pi^0 \Lambda$ at the same energy, although this has been indefinitely postponed due to group participation in CERN SPS experiment WA11.

The experimental setup would be every similar to that described in Chapter 2 i.e. a 5 GeV/c K^- beam, frozen spin polarized proton target, magnet spark chamber spectrometer to analyse Λ decay and an additional π^0 detector.

This chapter deals with a small test π^0 detector which was installed in our beam line and tested during December 1975.

7.2 The π^0 Detector

In order to fully reconstruct each event it would be necessary to know the direction and energy of both the gammas from π^0 decay to good accuracy. It was proposed to

measure both these in a counter a few metres downstream from the target after the spark chamber spectrometer.

The counter consisted of a heavy metal plate spark chamber followed by lead/scintillator sandwich counters. The positions of the gamma's could be measured by observing tracks of showers in the heavy metal plate chamber viewed by television cameras and the shower energy measured by the lead/scintillation hodoscope.

7.2.1 Description of the Counter

The spark chamber consisted of 12 copper plates each 3mm. thick separated by 17mm. of argon, a total of 2.5 radiation lengths corresponding to a 92% probability of conversion. Thus 85% of π^0's with both gamma's hitting the counter will have both γ's showering in the chamber. The area covered by the chamber was approximately 50cm. x 50cm. A cross-section through the counter is shown in fig. 7.1.

Behind the spark chamber were 18 lead/scintillator shower counters arranged in three planes of 6 counters each, 2 'y' planes and 1 'z' plane. A schematic of the detector showing the spark chamber and 4 of the shower counters is shown in fig. 7.2. Each shower counter consisted of 6 3mm. lead sheets separated by 6 2mm. scintillator sheets. Each shower counter was a total of 3.4 radiation lengths making the complete detector 12.7 radiation lengths long, enough to contain $\sim$90% of a 2.5 GeV gamma.

The two faces of each shower counter were not the same width since they were originally constructed as a cylindrical neutron counter with wider faces adjacent. For our application however the counters were placed together with the wider faces alternately at the front and then the back to produce a flat counter.

7.2.2 Monte Carlo Studies

A Monte Carlo shower program GERBE, written by the Strasbourg group at CERN, was the basis for the Monte Carlo simulation of the counter.

The program is able to track the passage of all secondaries, above a certain minimum energy, from an incident photon or electron through various layers of different materials. The program stores the values of the energy deposited, positions and momenta of all particles etc. in each layer, as the simulation progresses through the material, and is able to repeat itself several times in order to get a statistical distribution for all required quantities.

By modifying the existing GERBE program to suit our needs it was possible to know how much energy would be deposited in each shower counter for a given energy primary gamma at a given point on the detector face. A sample result is shown in fig. 7.3.

The program was run with gammas of incident energy 0.5, 1.0, 1.5, 2.0, 2.5, 3.0, 3.5, 4.0 and 4.5 GeV at approximately 2cm. intervals over the whole face of the detector. By interpolation it was then possible to use the results of these runs to obtain the energy distribution in the shower counters for any energy ($\lesssim$ 5.0 GeV) gamma incident anywhere on the detector face i.e. the problem of energy sharing was dealt with by pattern matching.

7.2.3 Event Reconstruction

For a given $\pi^0 \rightarrow \gamma\gamma$ event with both gamma's hitting the detector, the positions (z_1,y_1) and (z_2,y_2) relative to the beam direction (x-axis) of the γ's in the detector would be given by the spark chamber readout. To determine the π^0 energy the following method was used.

An energy ε_i', being the sum of the energy in the i^{th} counter given by the Monte Carlo when a gamma of energy E_1' was incident at (z_1,y_1) and a gamma of energy E_2' was incident at (z_2,y_2), was calculated. A χ^2 was then calculated by

$$\chi^2_{E_1'E_2'} = \sum_{i=1,18} \frac{(\varepsilon_i - \varepsilon_i')^2}{\sigma\varepsilon_i'^2}$$

where ε_i is the observed energy in counter i and $\sigma\varepsilon_i'$ is the error on ε_i'. The sum is over all the counters.

Various combinations of E_1' and E_2' were taken and by minimizing the χ^2 the best estimates of the 'real' gamma

energies E_1 and E_2 could be found where E_1 and E_2 are the gamma energies corresponding to χ^2 minima. The values of χ^2 for 2 gamma's of energy 3.75 GeV and 1.25 GeV incident on the detector are shown in Table 7.1.

7.2.4 Precision in π^0 Mass Determination

The program was used to simulate the decay of 5 GeV/c π^0's, 6 metres from the detector, track the two γ's through the detector and use the method outlined above to reconstruct the gamma energies and hence the π^0 mass. The mass distribution is shown in fig. 7.4. The mass precision is approximately 3% compared with $\sim$ 2% for the K^0's in the present experiment. These are however π^0's constrained to be 5 GeV and the energy precision is much worse than this being $\sim \frac{35\%}{\sqrt{E}}$ (FWHM) (see fig. 7.4).

7.3 The Test Run

It was hoped that charge exchange $\pi^- p \rightarrow \pi^0 n$ would provide π^0's of a suitable energy to test the detector.

The same apparatus as described in Chapter 2 was used except for the removal of the tungsten in the F counters and the fact that the E counters were placed in front of the π^0 detector and put in anticoincidence ensured that we did not trigger when charged particles entered the π^0 detector.

The heavy plate spark chamber was viewed from the top

and side, both views being recorded by the same TV camera via a mirror and prism system.

It was attempted to calibrate each shower counter separately in the beam with the Čerenkov counter adjusted for electrons but it was found that there were large variations in pulse height over long periods and eventually it was decided to rely on a running calibration using light diodes (which were built into the counters) and minimum ionizing particles during the data taking.

Approximately 200,000 triggers were taken during this run. By looking at the heavy plate chamber by eye, it was estimated that showers were seen in about 5% of the triggers. Some care had to be taken as the spark chambers sometimes broke down along the side facing the camera, which gave the appearance of a 'track' in one view. In fig. 7.6 online computer reconstructions of possible 2γ events are shown.

7.4 Conclusion

Since the $K^-p \rightarrow \pi^0\Lambda$ experiment has been indefinitely postponed, the data from this test run has not yet been analysed. The Monte Carlo studies show that we are able to recognise 5 GeV π^0's although the energy measurement would not be very good. We feel confident that a larger and better constructed purpose built detector of this design would enable us to identify and measure π^0's sufficiently well to enable the experiment to be performed satisfactorily.

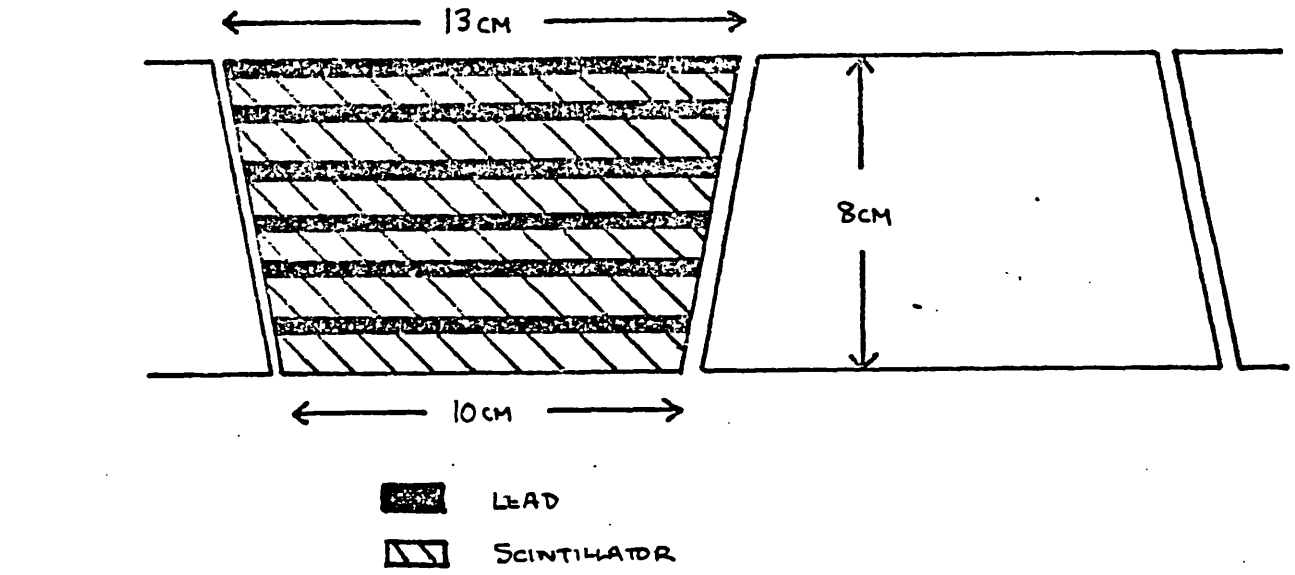
Table 7.1

Values of χ^2 as a function of gamma energies

E_1' (GeV)	E_2' (GeV)	$\chi^2_{E_1'E_2'}$
0.5	4.5	517.3
1.0	4.0	144.2
1.5	3.5	83.6
2.0	3.0	31.3
2.5	2.5	32.7
3.0	2.0	15.3
3.5	1.5	4.3
4.0	1.0	4.1
4.5	0.5	37.8

Figure 7.1

Cross-section of π^0 Detector



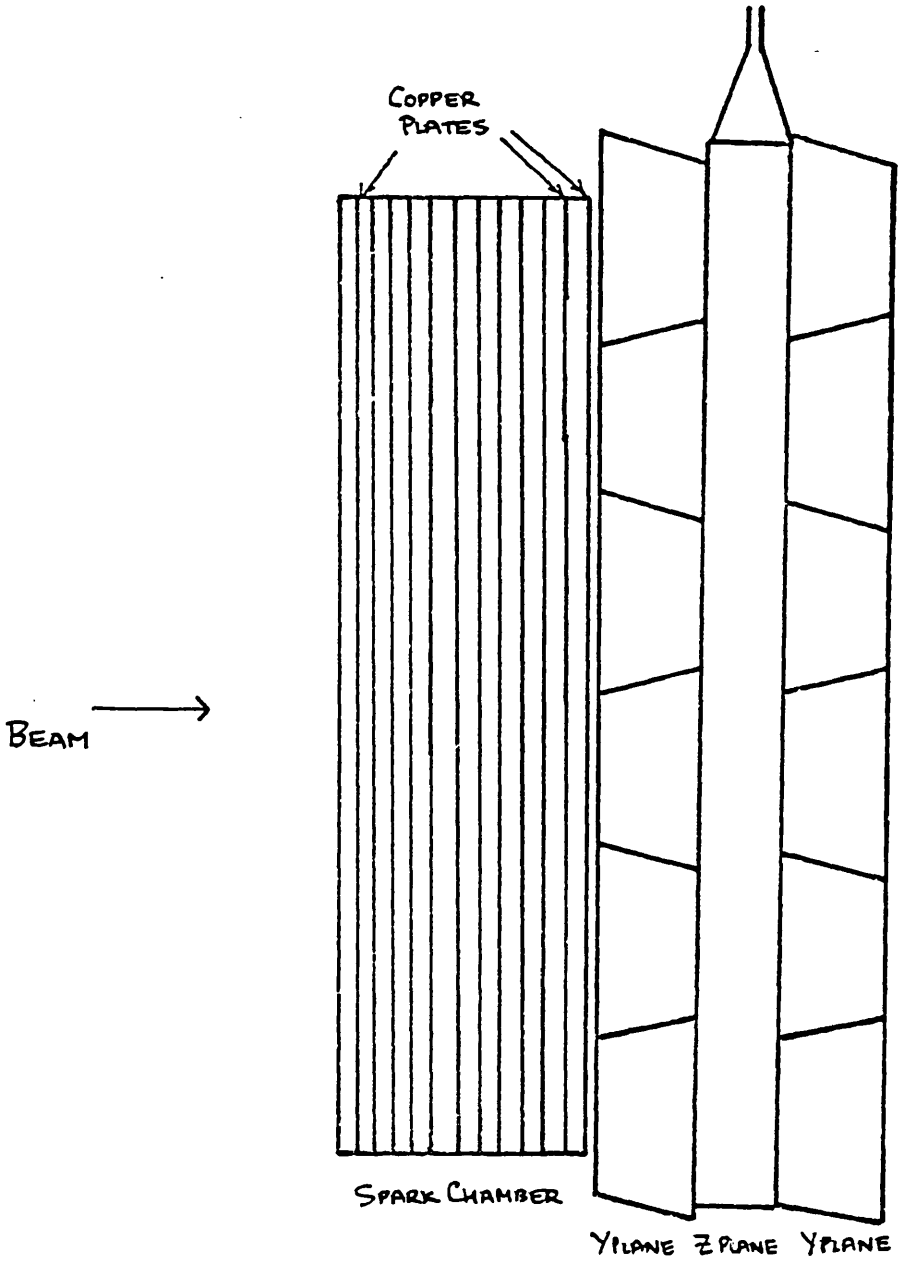


Figure 7.2

Schematic View of Part of π^0 Detector

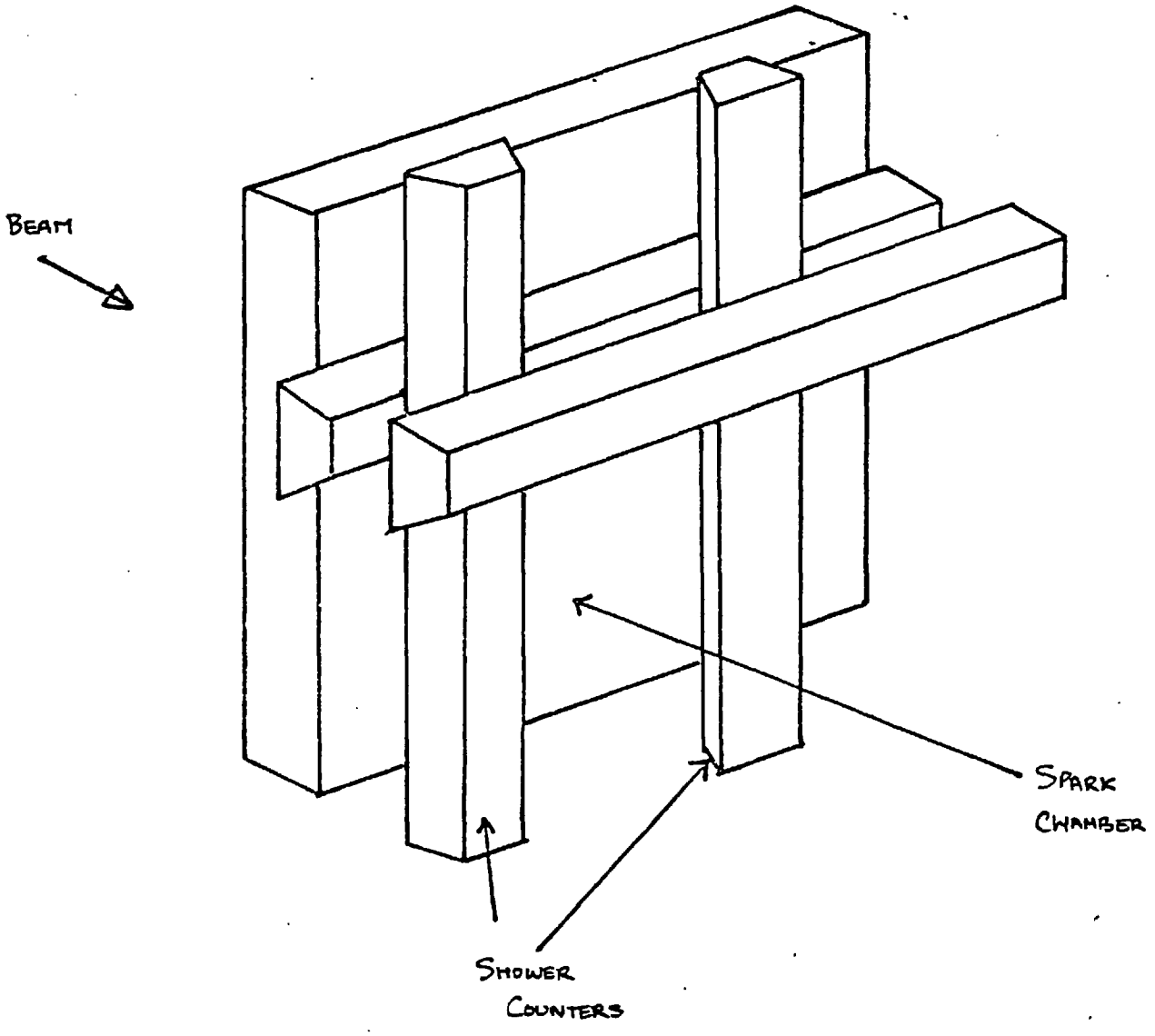


Figure 7.3

Sample Shower Distribution

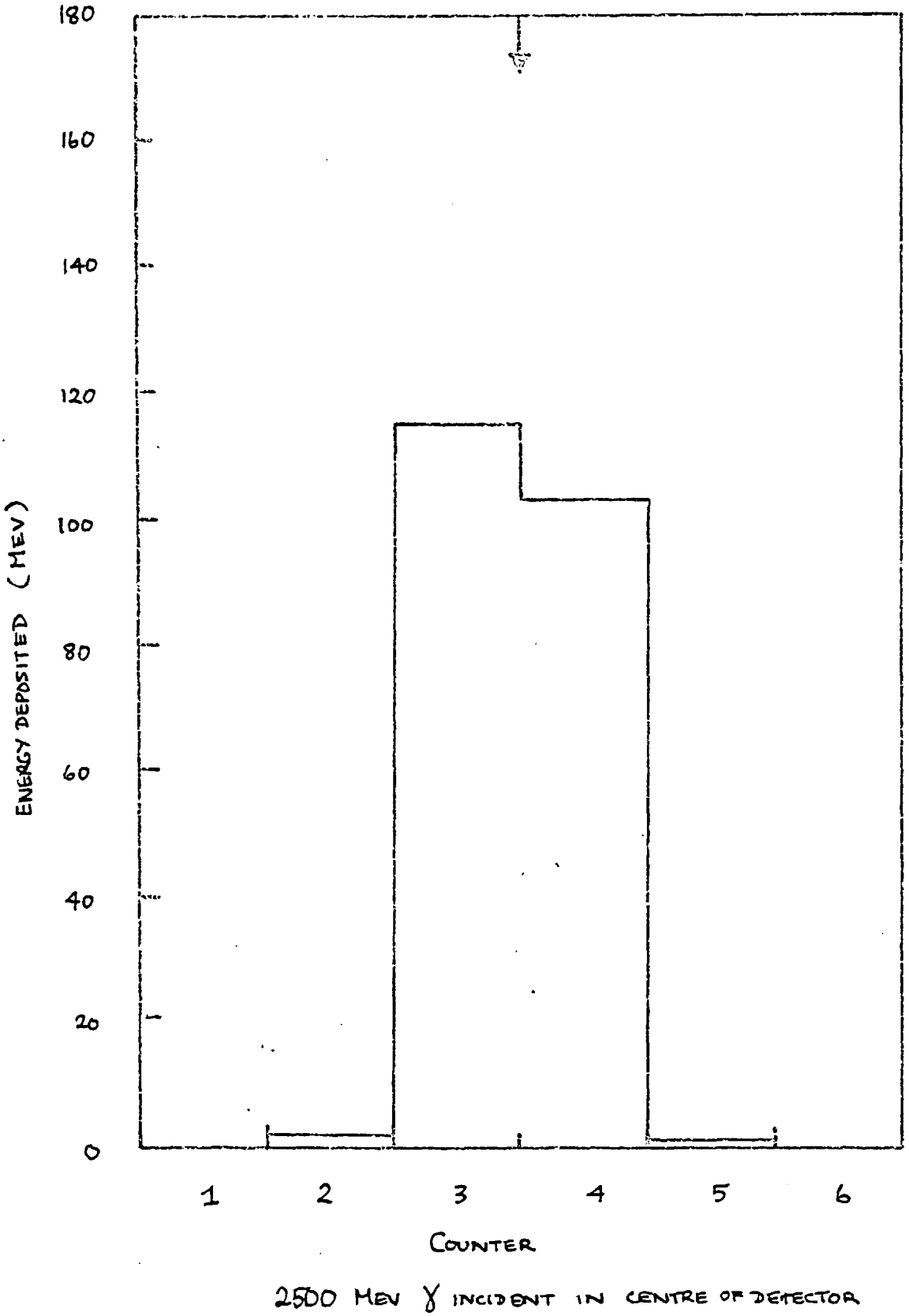


Figure 7.4

π^0 Mass Distribution

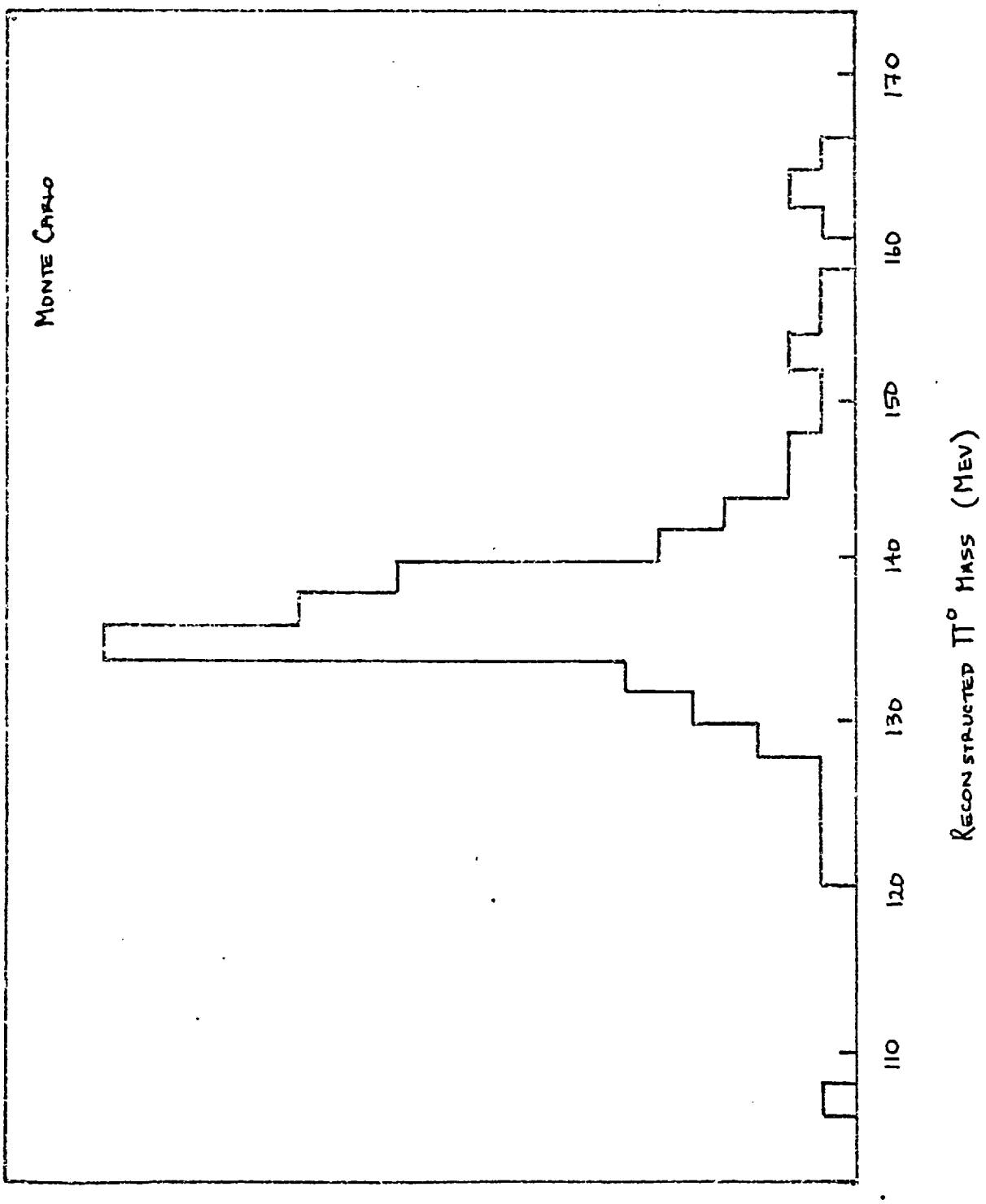


Figure 7.5

Energy Resolution

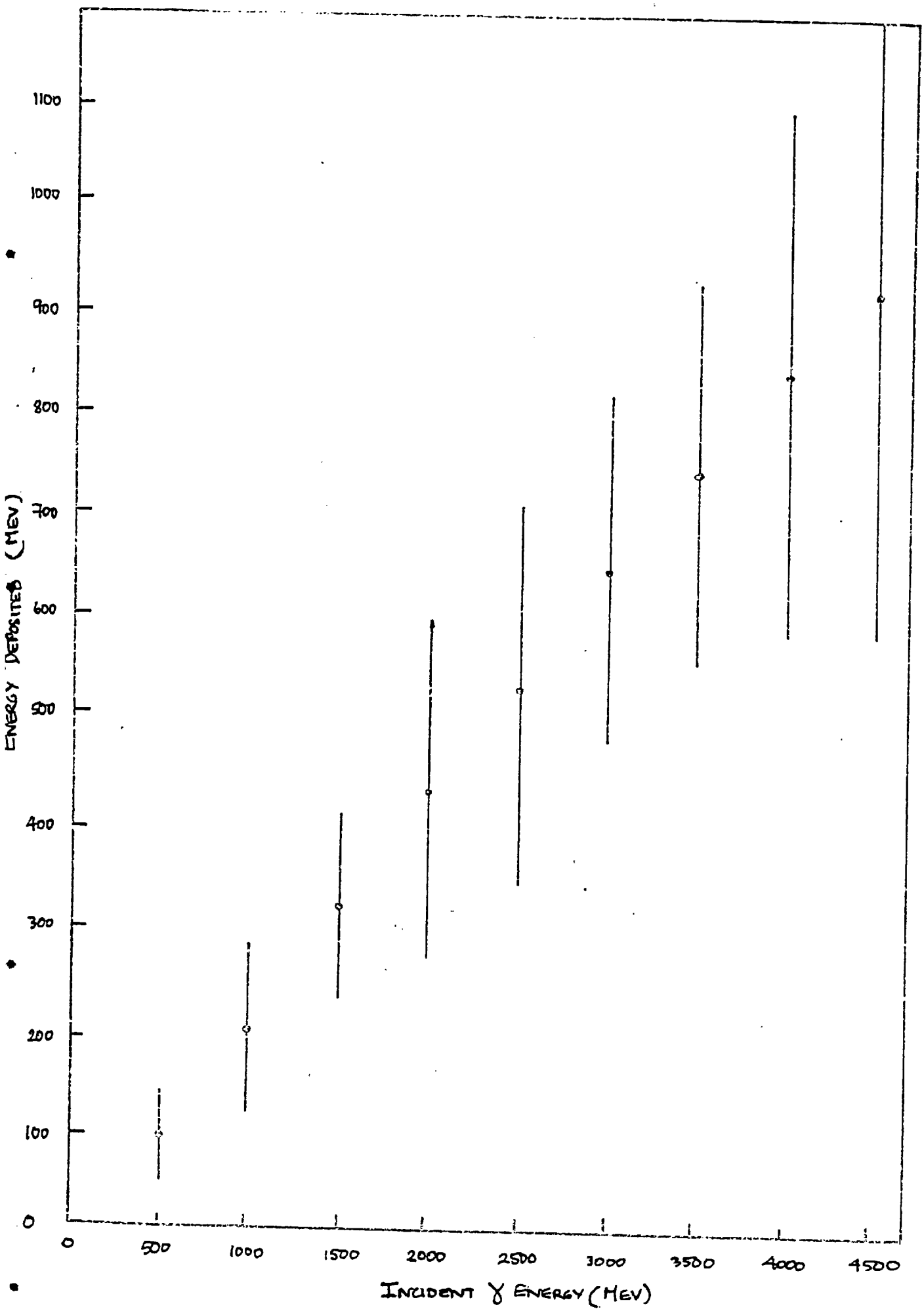
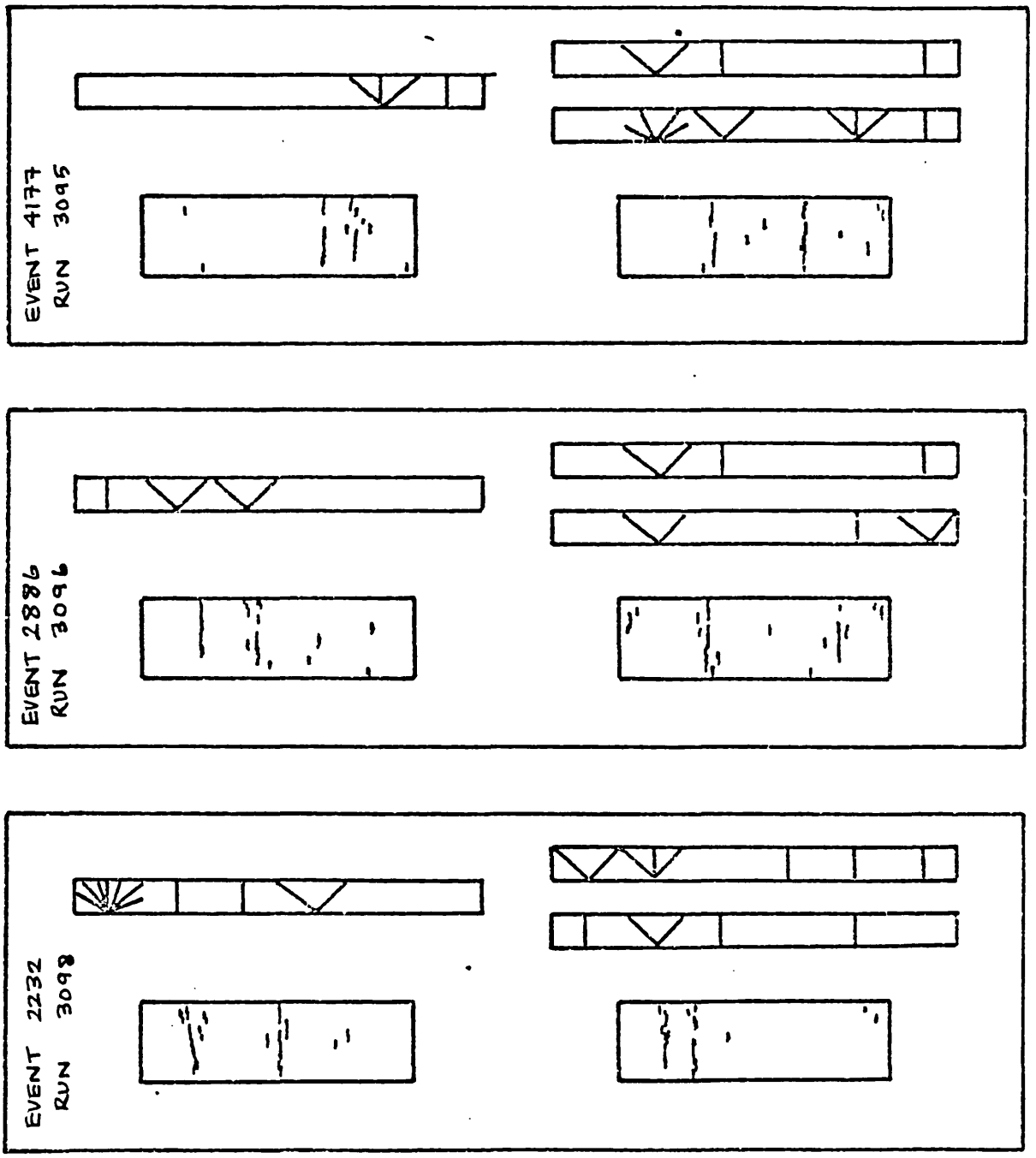


Figure 7.6

Online Display of Shower Candidates



APPENDIX 1

Density Matrix Formalism

A pure state $|\phi\rangle_p$ can be represented by a basis

$$|\phi\rangle_p = \sum_K \langle K|\phi\rangle_p |K\rangle$$

The expectation value of a hermitian operator Q is

$$\langle Q\rangle_p = \langle\phi|Q|\phi\rangle = \sum_{jk}\sum \langle\phi|K\rangle\langle K|\phi|j\rangle\langle j|\phi\rangle_p$$

A mixed state is an incoherent sum of pure states. The expectation value for a mixed state is the sum of the expectation values of the pure states weighted by the probability w_n that that state appears in the mixture.

$$\langle\phi\rangle_M = \sum_n \langle\phi\rangle_n w_n$$

$$\langle\phi\rangle_m = \sum_n w_n \left\{ \sum_j \sum_k \langle\phi|k\rangle\langle k|Q|j\rangle\langle j|\phi\rangle_n \right\}$$

$$= \sum_j \sum_k \langle k|Q|j\rangle \sum_n w_n \langle\phi|k\rangle\langle j|\phi\rangle_n$$

The Density Matrix is defined to be the quantity

$$\rho_{jk} = \sum_n w_n \langle\phi|k\rangle\langle j|\phi\rangle_n$$

If we use matrix notation for Q we have

$$Q_{kj} = \langle k|Q|j\rangle$$

$$\langle Q \rangle = \sum_k \sum_j Q_{kj} \rho_{jk} = \sum_K (Q\rho)_{KK} = \mathrm{Tr}(Q\rho)$$

where Tr is the trace of the matrix. ρ is Hermitian and has unit trace (unitarity constraint). For baryons of spin $\frac{1}{2}$ ρ will be a 2 x 2 matrix which can always be written as a linear combination of the Unit Matrix 1 and the Pauli Matrices σ.

$$\rho = a.1 + \underline{b}.\underline{\sigma} \qquad \text{since } \mathrm{Tr}(\rho) = 2a = 1$$

$$\rho = \tfrac{1}{2}(1 + \underline{p}.\underline{\sigma}) \qquad \text{where } \underline{p} \text{ is the polarization}$$

The initial and final pure states are related via a Matrix M.

$$|\phi_n^f\rangle = M|\phi_n^i\rangle \qquad \text{for the } n^{th} \text{ pure state}$$

$$\therefore \langle\phi_n^f| = \langle\phi_n^i|M^+$$

$$\rho^f_{jk} = \sum_n w_n \langle\phi_n^i|k\rangle\langle j|\phi_n^i\rangle$$

$$\therefore \rho^f_{jk} = \sum_n w_n \langle\phi_n^f|k\rangle\langle j|\phi_n^f\rangle$$

$$= \sum_n w_n \langle j|\phi_n^f\rangle\langle\phi_n^f|k\rangle$$

$$= \sum_n w_n \langle j|M|\phi_n^i\rangle\langle\phi_n^i|M^+|k\rangle$$

$$= \sum_n w_n \sum_{lm} \langle j|M|l\rangle\langle l|\phi_n^i\rangle\langle\phi_n^i|m\rangle\langle m|M^+|k\rangle$$

$$\therefore \rho^f_{jk} = \sum_{lm} \langle j|M|l\rangle \rho^i_{lm} \langle m|M^+|k\rangle$$

$$= \sum_{lm} M_{jl} \rho^i_{lm} M^+_{mk}$$

So the matrix relation between ρ^f and ρ^i is $\rho^f = M\rho^i M^+$

APPENDIX 2

Parity Violating Baryon Decays

We use as an example $\Lambda \to p\pi^-$ where parity is not conserved. Thus a $\frac{1}{2}^+$ decays like a $\frac{1}{2}^+$ and a $\frac{1}{2}^-$. The first decay is $l = 1$ and second $l = 0$. Let them have amplitudes a_p and a_s.

$$|JM\rangle \text{ for } \Lambda \text{ is } |\tfrac{1}{2}, \pm\tfrac{1}{2}\rangle$$

If decay is pure $l = 0$ $\quad |\tfrac{1}{2}, \pm\tfrac{1}{2}\rangle = Y_{00}\,|\tfrac{1}{2}, \pm\tfrac{1}{2}\rangle$

If decay is pure $l = 1$

$$|\tfrac{1}{2}, \pm\tfrac{1}{2}\rangle = \mp\sqrt{1/3}\; Y_{10}|\tfrac{1}{2}, \pm\tfrac{1}{2}\rangle \pm \sqrt{2/3}\; Y_{1\pm1}|\tfrac{1}{2}, \mp\tfrac{1}{2}\rangle$$

Thus if M is the matrix for the decay

$$M|\tfrac{1}{2}, \pm\tfrac{1}{2}\rangle = a_s Y_{00}|\tfrac{1}{2}, \pm\tfrac{1}{2}\rangle + a_p(\mp\sqrt{1/3}Y_{10}|\tfrac{1}{2}, \pm\tfrac{1}{2}\rangle \pm 2/3 Y_{1\pm1}|\tfrac{1}{2}, \mp\tfrac{1}{2}\rangle$$

Thus
$$M = \frac{1}{\sqrt{4\pi}} \begin{pmatrix} a_s - a_p\cos\theta & -a_p\sin\theta e^{-i\phi} \\ -a_p\sin\theta e^{i\phi} & a_s + a_p\cos\theta \end{pmatrix}$$

If we specify the direction of the proton in the Λ centre of mass as $\underline{k} = (\sin\theta\cos\phi, \sin\theta\sin\phi, \cos\theta)$ then

$$\underline{k}.\underline{\sigma} = \begin{pmatrix} \cos\theta & \sin\theta e^{-i\phi} \\ \sin\theta e^{i\phi} & -\cos\theta \end{pmatrix}$$

where $\underline{\sigma}$ are the Pauli matrices.

$$M = \frac{1}{\sqrt{4\pi}} (a_s - a_p \underline{k}.\underline{\sigma})$$

Since $\rho f = M\rho^{i}M^{+}$ and $\rho^{i} = \frac{1}{2}(1 + \underline{P}^{i}.\underline{\sigma})$ with $\underline{P}^{i} = \underline{P}^{\wedge}$ then

$$\rho f = \frac{1}{8\pi}(a_s - a_p\underline{k}.\underline{\sigma})(1 + \underline{P}^{\wedge}.\underline{\sigma})(a_s^{*} - a_p^{*}\underline{k}.\underline{\sigma})$$

$$= \frac{1}{8\pi}\left[|a_s|^2 + |a_p|^2 + (|a_s|^2 + |a_p|^2)\underline{P}^{\wedge}.\underline{\sigma}\right.$$

$$\left. - (2\mathrm{Re}\ a_s a_p^{*})(\underline{P}^{\wedge}.\underline{k} + \underline{k}.\underline{\sigma})\right]$$

Let $$\alpha = \frac{-2\mathrm{Re}\ a_s a_p^{*}}{|a_s|^2 + |a_p|^2}$$

where α is the Λ decay asymmetry parameter = 0.647.

Now $$\left(\frac{d\sigma}{d\Omega}\right)_{\text{decay}} = \mathrm{Tr}\,\rho f$$

$$= \frac{1}{8\pi}(|a_s|^2 + |a_p|^2)\{1 + \alpha\underline{P}^{\wedge}.\underline{k}\}$$

$$\therefore \left(\frac{d\sigma}{d\Omega}\right)_{\text{decay}} = \left(\frac{d\sigma}{d\Omega}\right)'\{1 + \alpha\underline{P}^{\wedge}.\underline{k}\}$$

APPENDIX 3

The Error in the Asymmetry

If n^+ and n^- are the observed number of events on target spin up (+) and down (-) and N^+ and N^- are the number of incident pions on these targets respectively, then the asymmetry α is given by

$$\alpha = \frac{\frac{n^+}{N^+} - \frac{n^-}{N^-}}{\frac{n^+}{N^+} + \frac{n^-}{N^-}}$$

The error in the asymmetry is then given by

$$(\Delta\alpha)^2 = \left(\frac{\partial\alpha}{\partial n^+}\right)^2 \Delta n^{+2} + \left(\frac{\partial\alpha}{\partial n^-}\right)^2 \Delta \bar{n}^2$$

If the events are distributed according to poisson statistics then $\Delta n^{\pm} = \sqrt{n^{\pm}}$

$$\text{now } \left(\frac{\partial\alpha}{\partial n^+}\right)^2 = \frac{4n^{-2}}{(N^+N^-)^2} \div \left(\frac{n^+}{N^+} + \frac{n^-}{N^-}\right)^4$$

$$\text{and } \left(\frac{\partial\alpha}{\partial n^-}\right)^2 = \frac{4n^{+2}}{(N^+N^-)^2} \div \left(\frac{n^+}{N^+} + \frac{n^-}{N^-}\right)^4$$

$$\therefore \quad (\Delta\alpha)^2 = \left(\frac{4n^{-2}n^+}{(N^+N^-)^2} + \frac{4n^{+2}n^-}{(N^+N^-)^2}\right) \Big/ \left(\frac{n^+}{N^+} + \frac{n^-}{N^-}\right)^4$$

$$\text{then } \Delta\alpha = \frac{2N^+}{N^-} \frac{\sqrt{n^+n^-(n^+ + n^-)}}{\left(n^+ + \frac{N^+}{N^-} n^-\right)^2}$$

If $R = \frac{N^+}{N^-}$

then $\Delta\alpha = \frac{2R}{(n^+ + R\bar{n})^2} \sqrt{n^+ n^- (n^+ + n^-)}$

and $\alpha = \frac{n^+ - Rn^-}{n^+ + Rn^-}$

Acknowledgements

I thank all the members of the CERN-ETH-Imperial College-Southampton-Helsinki collaboration for the success of this experiment especially Dr. M.C.S. Williams for patiently explaining the intricacies of ROMEO to me.

I am indebted to my supervisor Dr. D.M. Websdale for his guidance, encouragement and friendly advice. It has been a pleasure to work with him.

I also wish to thank Professor I. Butterworth for the opportunity of working in the High Energy Physics Group at Imperial College and Professor E. Picasso for allowing me to work at CERN as a visiting scientist.

The Science Research Council provided financial support for a period of three years.

Finally I thank Ms. Linda Gold for her excellent typing of this thesis.

References

1. H. Muirhead - The Physics of Elementary Particles, Pergamon Press (1965)
2. L. Wolfenstein - Phys. Rev. 96, 1654 (1954)
3. A.C. Irving, A.D. Martin and V. Barger - Nuov. Cim. 16A, 573 (1973)
4. J.J. de Swart - Rev. Mod. Phys. 35, 916 (1963)
5. O. Guisan - 2nd. Int. Conf. on Polarized Targets, LBL (1971)
6. T.O. Niinikoski and F. Udo - Nucl. Inst. and Meth. 134, 219 (1976)
7. P. Astbury et al - Nucl. Inst. and Meth. 46, 61 (1967)
8. M.C.S. Williams - Ph.D. Thesis, University of London (1976)
9. ROMEO Information Notes - CERN OM/SPS
10. J.A. Wilson - Ph.D. Thesis, University of London (1975)
11. P. Mühlemann and J.D. Wilson - CERN Yellow Report CERN 70-17 (1970)
12. CERN E.E.C. Proposal PH I/COM - 73/16 (1973)
13. W. Beusch et al - Nucl. Phys. B99, 53 (1975)
14. O. Guisan et al - Nucl. Phys. B32, 681 (1971)
15. S.M. Pruss et al - Phys. Rev. Lett. 23, 189 (1969)
16. K.S. Kölbig and B. Margolis - Nucl. Phys. B6, 85 (1968)
17. M.F. Letheren - Ph.D. Thesis, University of London (1972)
18. Compilation of $\pi^{\pm}$ Cross-sections - CERN/HERA 72-1 (1972)

19. CERN Computer Centre Program Library - long write-up D506, D516

20. P. Astbury et al - Nucl. Phys. B99, 30 (1975)

21. C.E.W. Ward et al - Phys. Lett. 48B 471 (1974)

22. C.E.W. Ward et al -Private communication

23. M. Abramovich - Nucl. Phys. B27, 477 (1971)

24. D.J. Crennell et al - Phys. Rev. D6, 1220 (1972)

25. V. Barger and D. Cline - Phenomenological Theories of High Energy Scattering, W.A. Benjamin (1968)

26. R.J.N. Phillips and D.P. Roy - Rep. Prog. Phys. 37, 1035 (1974)

27. D. Hill et al - Phys. Rev. Lett. 30, 239 (1973)

28. V. Barger and A.D. Martin - Phys. Lett. 39B, 379 (1972)

29. D.D. Reeder and K.V.L. Sarma - Phys. Rev. 172, 1566 (1968)

30. R.C. Arnold and R.K. Logan - Phys. Rev. 177 2318 (1969)

31. R.J.N. Phillips - Proc. 1972 CERN Summer School, CERN 72-17 (1972)

32. H. Navelet and P.R. Stevens - Nucl. Phys. B104, 171 (1976)

33. A.D. Martin, C. Michael and R.J.N. Phillips - Nucl. Phys. B43, 13 (1972)

34. P.A. Baker et al - Phys. Rev. Lett. 40, 678 (1978)

35. G. Giradi - J. Phys. G3, 1031 (1977)

36. A.C. Irving, A.D. Martin and C. Michael - Nucl. Phys. B32, 1 (1971)

37. H. Harari - Ann. Phys. (N.Y.) 63, 432 (1971)

38. J.S. Loos and J.A.J. Matthews - Phys. Rev. D6, 2463 (1972)

39. R. Dolen, D. Horn and C. Schmid - Phys. Rev. 166, 1768 (1968)

40. R.D. Field and J.D. Jackson - Phys. Rev. D4, 693 (1971)

41. C.E.W. Ward, W.T. Meyer and D.R. Rust - Phys. Rev. D11, 1802 (1975)

42. C.E.W. Ward et al - Phys. Lett. 31 1149 (1973)

43. CERN Letter of Intent - CERN/E.E.C.-74/18